

The development of a distributed electric propulsion (DEP) noise model

Chris Bononi Bello



The development of a distributed electric propulsion (DEP) noise model

by

Chris Bononi Bello

to obtain the degree of Master of Science
at the Delft University of Technology,
to be defended publicly on 18-12-2023

Student number: 4667530
Project duration: 01-02-2023 – 18-12-2023
Thesis committee: Feijia Yin (TU Delft)
Ewoud Smeur (TU Delft)
Mirjam Snellen (TU Delft)
Sander Heblj (NLR)
Wouter de Haan (NLR)

An electronic version of this thesis is available at <http://repository.tudelft.nl/>.

Acknowledgements

This document contains my graduation thesis, which is the final hurdle to complete the master Sustainable Air Transport at the faculty of Aerospace Engineering of Delft University of Technology. The past year I have been investigating the noise produced by a distributed electric propulsion configuration. Throughout the duration of the project I have been guided and assisted by a number of people, whom I would like to thank from the bottom of my heart for their time and advice.

First of all, I would like to thank my supervisors Mirjam Snellen, Sander Heblj, and Wouter de Haan. I would like to extend my heartfelt gratitude to them for their guidance throughout my graduation journey. Throughout the project, I thoroughly enjoyed our meetings and discussions, which definitely contributed to the final result. Mirjam, Sander and Wouter, your guidance during my graduation project has been invaluable.

Secondly, I want to express my sincere appreciation to Bieke von den Hoff for her invaluable support during the course of my thesis work. Bieke was always available to answer questions or discuss theories, which played a pivotal role in the progress of my research. Bieke, I found our meetings to be exceptionally helpful, and therefore I would like to extend my heartfelt thanks to you.

Thirdly, I would like to thank the people who played an important part in generating the validation data. I extend my sincere appreciation to Fernanda do Nascimento Monteiro, Alessandro Mancinelli, and Anique Altena. Your invaluable support was instrumental in enabling me to validate the model using authentic experimental data, a critical contribution that greatly enhanced the quality of my research. Without your assistance, this milestone would not have been attainable.

Lastly, I would like to express my heartfelt appreciation to my family and my girlfriend, who are my biggest source of support and inspiration.

C. Bononi Bello
The Hague, November 2023

Contents

List of Figures	vii
List of Tables	ix
Introduction	xi
I Scientific Paper	1
II Literature Study previously graded under AE4020	25
III Supporting work	65
1 Read me file for Helix tool and DEP model	67
Bibliography	69

List of Figures

Figure 1: Examples of distributed electric propulsion aircraft	5
Figure 2: Flow chart of a general isolated propeller noise model	6
Figure 3: The thrust and power coefficient for an axial Mach number of 0.2 and $\beta_{0.75} = 45.8$	8
Figure 4: Directionality plots of test cases 1 and 2	9
Figure 5: Directionality plot of all noise components computed by the Helix and NLR tools	9
Figure 6: Flowchart of the DEP model	10
Figure 7: The required steps to incorporate the propagation effects in a multi-propeller configuration	12
Figure 8: Scenario 1 with both propellers located 4 m from the middle on opposite wings	12
Figure 9: Scenario 2 with one propeller placed 4 m from the middle and the second propeller located 21 m from the middle on the opposite wing	13
Figure 10: In-plane directivity of a two propeller simulation with different spacing between the propellers	13
Figure 11: Research conducted by Guerin	14
Figure 12: OSPL directivity comparison of case 1 and 2 between Guerin’s results and the developed DEP model	15
Figure 13: GL-10 in hover mode (left) and top view of the forward flight configuration (right)	15
Figure 14: Noise contours comparison between the results produced by Rizzi and the DEP model	16
Figure 15: Experimental setup used for the flyover validation	17
Figure 16: Comparison of the DEP model with the performed flyover measurements	18
Figure 17: Spectrogram of the self performed flyover experiment	18
Figure 18: Front and side view from Maeve-01	19
Figure 19: OSPL results of a Maeve-01 flyover	19
Figure 20: Spectrogram of a Maeve-01 flyover	20
Figure 21: Example heat map when the loading noise is dominant produced by the DEP model	23
Figure 22: The array test setup during the experiments	24
Figure 23: Beamform plot for a frequency range of 2 - 5 kHz	24
Figure 24: Frequency spectra of the DEP model and outdoor measurements at 3.8 sec for a 0.1 s interval	24
Figure 1.1: Examples of distributed electric propulsion aircraft	32
Figure 3.1: The top level and planform parameters of a propeller	34
Figure 3.2: Actuator disk model with control volume for the application of the momentum equation	35
Figure 3.3: Propeller performance diagram: thrust and power coefficient and efficiency as a function of advance ratio	36
Figure 4.1: Visualisation of the motion of air molecules within an acoustic wave	38
Figure 4.2: Overview of the aerodynamic noise sources	39
Figure 4.3: Characteristics of propeller harmonic noise	40
Figure 4.4: Characteristics of propeller broadband noise	41
Figure 4.5: Audio of a flyover event	42
Figure 4.6: OSPL and OASPL plotted over time	42
Figure 5.1: Reflection of a sound ray via the ground	44
Figure 5.2: Effect distance has on the noise intensity: the spreading effect	44
Figure 5.3: The necessary signal processing steps to incorporate the propagation effects	45
Figure 6.1: Flowchart showing the general overview of the main processes involved in a DEP noise model	46
Figure 6.2: Velocity and force vectors of a blade element	47
Figure 6.3: Example of a thickness distribution	49

Figure 6.4: Flow chart of a general isolated propeller noise model	50
Figure 6.5: The thrust and power coefficient for an axial Mach number of 0.2 and $\beta_{0.75} = 45.8$. . .	51
Figure 6.6: The thrust and power coefficient for an axial Mach number of 0.27 and $\beta_{0.75} = 45.8$. .	51
Figure 6.7: Case 1: Directionality plot comparing the OSPL of the Helix-and NLR tool	52
Figure 6.8: Directionality plots of test cases 3 and 4	53
Figure 6.9: Directionality plot of all noise components computed by the Helix-and NLR tool	53
Figure 6.10: Representation of the methodology used by Pascioni and Rizzi	55
Figure 6.11: Processed pressure time signal as received by the observe	58
Figure 6.12: Spectrogram of the DEP configuration with a total duration of 35 second	58
Helix tool work flow diagram [1]	68

List of Tables

Table 1: Input parameters for the different test cases	9
Table 2: Operating conditions used in Guerin	14
table 3: Operating conditions and other inputs of the drone during the flyover	17
Table 4: Operating conditions used for Maeve-01	19
Table 6.1: Input parameters for the different test cases	52
Table 6.2: Operating and propeller characteristics used as input for the preliminary results	57
Table 6.3: Performance coefficients for the preliminary results	57

Introduction

In response to the deeply troubling global warming caused by significant human-made emissions, the aviation sector has initiated a series of projects to explore alternate propulsion systems. These projects aim to diminish aviation's environmental footprint. Within this context, distributed electric propulsion (DEP) has gathered growing attention over the past ten years. The core idea of DEP involves dividing the overall thrust among multiple propulsors, which are then strategically positioned across the wingspan. This approach presents new opportunities for aircraft designs with a focus on reducing emissions. While DEP configurations have the potential to revolutionise aircraft designs and performance, there are still several technological and operational challenges that must be addressed before these aircraft start roaming the skies, e.g., the annoyance experienced by people when a DEP aircraft flies over their head. For that reason, the development of a tonal noise prediction model of a DEP configuration is introduced in this research, which makes it possible to assess the annoyance experienced by the community in a follow up project.

For this project, Delft University of Technology (TUD) and the Netherlands Aerospace Centre (NLR) are teaming up to work on bringing the sounds of a distributed electric propulsion aircraft to life. This collaboration is a joint effort to enhance our understanding of the noise of a DEP aircraft, benefiting from the strengths of both TUD and NLR in academic research and aerospace innovation. The research project was conducted as part of a graduation project within the Sustainable Air Transport group of the aerospace engineering faculty at Delft University of Technology. This group is dedicated to exploring the complexities of noise dynamics and climate implications associated with the aviation industry.

The report is structured into three main segments. The first section comprises a scientific paper, which discusses a method to construct a tonal noise model of a distributed electric propulsion aircraft. In this paper, first, the methodology is discussed elaborately, and thereafter, the results of a reference aircraft are presented. Moving on, the second section contains a literature study conducted at the beginning of the project, aimed at acquiring insights into the field of propeller acoustics. The concluding part incorporates supportive material, offering a more in-depth explanation on the developed Matlab code.

I

Scientific Paper

The development of a distributed electric propulsion (DEP) noise model

Christopher Bononi Bello,*

Delft University of Technology, Delft, The Netherlands &
Netherlands Aerospace Centre, Amsterdam, The Netherlands

Abstract

With the ever-increasing demand of air travel from before the pandemic expected to return, the world's concern of environment-related issues linked to aviation has also increased. With these issues becoming progressively important, it is not surprising that the propeller, with generally a superior efficiency over the jet engine, has regained the interest of the aviation sector. Among the various concepts being explored, one particular propeller configuration stood out as promising: the distributed electric propulsion (DEP) configuration. While DEP configurations have the potential to revolutionise aircraft designs and their performance, there are still several technological and operational challenges that must be addressed before these configurations start roaming the skies. One of the research areas that still needs to be explored, for example, is the noise pollution caused by a DEP aircraft, and consequently the impact it has on society. For that reason, the development of a noise prediction model of a DEP aircraft is introduced in this paper. Acoustic results are presented for Maeve-01, a DEP concept aircraft designed by Dutch startup Maeve Aerospace¹. The DEP model solely focuses on tonal propeller noise generated by steady blade loading and propeller rotation; i.e., broadband sources and unsteady loading noise are disregarded in this study. The tonal noise signatures of an isolated propeller are computed with a model that uses the Helicoidal Surface Theory to predict the source noise. Subsequently, the individual source noises are superimposed at observers in the far field by applying digital processing steps to incorporate spherical spreading, the Doppler effect, atmospheric absorption and phase lags to include the interference effects between propellers. The DEP model is verified both using a more computational intensive model (developed by NLR) for the isolated propeller signatures, and by predicting the directivity patterns of two monopole sources along the axis over the wing span to model the source field of two interfering propellers. For the validation of the DEP model, real-life flyover experiments have been performed with a small drone with four propellers, combined with a comparison with literature data.

Nomenclature

α	Propeller angle of attack,	[°]
Ω	Rotational speed,	[rad/s]
ϕ	Azimuthal angle,	[°]
ϕ_o, ϕ_s	Phase lag due to offset and sweep,	[°]
Ψ_V, Ψ_D, Ψ_L	Thickness, drag and lift distributions	[-]
θ	Radiation angle from propeller axis to observer point,	[°]
B	Number of blades,	[-]
BPF	Blade passage frequency,	[Hz]
c	Speed of sound,	[m/s]
C_p	Propeller power coefficient , $P/(\rho n^3 D^5)$,	[-]

*Msc Student, Sustainable Air Transport, Faculty of Aerospace Engineering, Delft University of Technology

¹This research has not been conducted in collaboration with Maeve, only their configuration was chosen as a reference aircraft

C_t	Propeller thrust coefficient , $T/(\rho n^2 D^4)$,	[–]
D	Propeller diameter,	[m]
i	Imaginary number defined as $i^2 = -1$,	[–]
J	Advance ratio, $V_f/(nD)$,	[–]
J_{mB}	Bessel function of the first kind of order mB ,	[–]
k	Acoustic wave number, $2\pi f_0/c_0$,	[rad/m]
k_x, k_y	Non-dimensional wave numbers,	[–]
m	Number of harmonics ,	[–]
M_x, M_t, M_r	Flight, rotational tip and effective Mach number,	[–]
n	RPM/60,	[1/s]
N_p	Number of propellers,	[–]
$OASPL$	Overall A-weighted sound pressure level,	[dBA]
$OSPL$	Overall sound pressure level,	[dB]
P_{mB}	Fourier coefficients of pressure-time signal at the m th harmonic of the BPF,	[–]
r	Distance between observer and source,	[m]
t_b	Maximum thickness to chord ratio,	[–]
V_f	Free stream velocity,	[m/s]
y	Vertical distance between observer and the propeller axis,	[m]

1 Introduction

From aviation pioneers in the early 1900s to the British-French supersonic Concorde aircraft, it can be said that the aviation industry experienced a spectacular development in the 20th century. It all started when one of the Wright brothers, Orville Wright, took off in 1903 with their aircraft, known as the Wright Flyer III. This aircraft relied on propellers to produce the thrust necessary for the historical moment of the first ever controlled, powered, and heavier-than-air flight. Their breakthrough resulted in the propeller being the subject of many research programs worldwide, which led to numerous successful propeller powered aircraft that showed impressive propulsive efficiencies for subsonic velocities [1]. It was only towards the end of World War II that a radically different propulsion system was introduced. We now know this new piece of technology as the jet engine. The invention of the jet engine and its derivatives (the turbofan and turboshaft), resolved some of the drawbacks experienced when using propeller driven aircraft, such as the limited service ceiling and flight velocity. Even though the jet engine came with a lot of benefits, it is important to note that the jet engine was not superior in every aspect, as it for instance had and generally still has a lower efficiency than a propeller driven aircraft [2]. Nevertheless, the introduction of the jet engine resulted in a stagnation in propeller research during the second part of the 20th century.

Consequently, in the past couple of decades, turboprops were mostly disregarded by commercial carriers (or mostly only used for regional/short haul flights), which is one of the main reasons why nowadays civil aviation mostly relies on turbofan engines. Turboprops were found to be noisy and old-fashioned. However, with the ever-increasing demand of air travel from before the pandemic expected to return [3], the world's concerns with the environment-related issues linked to aviation have also increased. The need for environmentally-friendly solutions in the aviation sector has become one of the global technological challenges that have emerged in the last couple of decades. The Advanced Air Vehicles Program at NASA has taken note of these challenges and launched several initiatives to tackle them [4]. One of its key projects involves investigating subsonic aircraft designs that can significantly decrease energy consumption and emissions related to passenger planes. With these issues becoming increasingly important, it is not surprising that the propeller, with generally a superior efficiency, has regained the interest of the aviation sector. Among the various concepts being explored, one particular propeller configuration stood out as promising: the distributed electric propulsion (DEP) configuration. This concept showed a lot of potential, and is therefore currently the subject of numerous research projects studied by various academic, government, and industry bodies [5].

To introduce the concept of DEP, it is first necessary to understand the more common concept of distributed propulsion (DP) more broadly. In a DP system, the thrust of an aircraft is generated by an array of propulsive devices distributed along the wing span, as opposed to a single centralised engine. One of the key features of an aircraft equipped with distributed propulsion is the close integration of the propulsion system into the wing and body surfaces. This results in a form of aero-propulsive coupling due to the increased number of propulsion units near the aerodynamic surfaces of the aircraft. Therefore, the advantage of a distributed propulsion system lies in the design of the propulsion-airframe integration, which could lead to several benefits. Firstly, a variety of vehicle configurations claim improved propulsive efficiency through boundary-layer ingestion. Secondly, strategic propulsor placement can effectively reduce vehicle drag through mechanisms such as wake filling and vortex suppression. Lastly, DP configurations utilise the interaction between the propeller or fan slipstream and aerodynamic surfaces, producing enhanced lift or improved control authority [5]. In addition to this, DEP systems use electrically driven propulsors that are connected to energy sources or power generating devices through electrical means. It is worth noting that power sources for said system are not limited to a specific type and can include any combination of devices that generate electrical power, such as electric generators or fuel cells, as well as energy storage devices like batteries or capacitors.

As mentioned before, the DEP concept has gained significant popularity in recent times. However, due to the limited specific energy density of existing hardware, the adoption of this technology has mainly been observed in small aircraft applications up until now. Nevertheless, due to the persistent interest in improving efficiency, reducing operating costs, and promoting sustainability in larger commercial aircraft, several organisations are now also investing in DEP aircraft systems capable of carrying more passengers and cargo. In Figure 1, example concepts of both cases are shown. In Figure 1(a), NASA’s X-57 Maxwell aircraft can be seen. This is NASA’s experimental aircraft, intended to investigate the DEP concept. The aircraft is a conventional fixed-wing configuration that utilises twelve small electrically driven propellers mounted to the leading edge of the wing and two larger ones placed at the wing-tips. All the required power is provided exclusively by a set of lithium-ion battery packs. In Figure 1(b), Dutch startup Maeve Aerospace’s concept for electric flying is depicted. They are trying to develop a 44-seat fully-electric regional aircraft, known as Maeve-01, and are aiming to have their aircraft in the skies by 2029 [6].



(a) DEP concept by NASA: X-57 Maxwell [7]



(b) All electric aircraft concept by Maeve Aerospace [6]

Figure 1: Examples of distributed electric propulsion aircraft

While DEP configurations have the potential to revolutionise aircraft designs and their performance, there are still several technological and operational challenges that must be addressed before these configurations start roaming the skies. One of the research areas that still needs to be explored further, for example, is the noise pollution caused by a DEP aircraft, and consequently the impact it has on society. For existing aircraft the noise can be measured by using a microphone array, for example. However, for new aircraft concepts this is not possible. Therefore, a different approach needs to be selected to assess the noise of a DEP system. An example of a suitable approach is the concept of auralization, which is the procedure of modelling a noise source and subsequently transforming the created noise sample into an audible result. Due to the pressing need for a noise sample of a DEP system, the objective of this research was to develop an analytical noise model of a DEP aircraft, so that the annoyance experienced by observers from such an aircraft can be evaluated in a later stage.

In this paper, the process of generating a noise model for a DEP aircraft flyover will therefore be discussed. Two noise prediction models of an isolated propeller are used as a starting point. The first model is developed by Netherlands Aerospace Centre (NLR), and will mainly be used for validation purposes, due to the fact that this model is more computationally intensive. The second model is called the Helix tool, and is developed by Haddaoui at Delft University of Technology [8]. This model will be the main building block to simulate and analyse the acoustic effects of a DEP flyover. The DEP noise model will focus on the tonal noise generated by

the propellers, because this represents the dominant noise source at the vertical of the aircraft [9]. This means that airframe noise, propeller broadband noise, and propeller-propeller aerodynamic interactions are disregarded in this study. The paper begins by introducing the methodology used in the isolated propeller models. In the same section, both models will also be compared to literature data for verification purposes. Subsequently, the approach used to model the noise of multiple propellers will be presented. In this section, the verification of the superposition of multiple propellers is also examined. Next, the validation of the DEP model will be discussed. The validation process is carried out by comparing the DEP model results with literature data and by performing real-life flyover experiments with a fixed wing drone. Finally, the results of the model will be presented for a flyover of Maeve-01.

2 Methodology

2.1 Isolated propeller

In this section, the methodology of the Helix and NLR tools will be compared to each other, and consequently their similarities and differences will be discussed. The Helix and NLR tools both consist of three major processes: the aerodynamic analysis, the performance analysis ², and the noise analysis. A representation of the flow of these processes is provided in Figure 2, where the yellow blocks stand for the outputs of the different analyses.

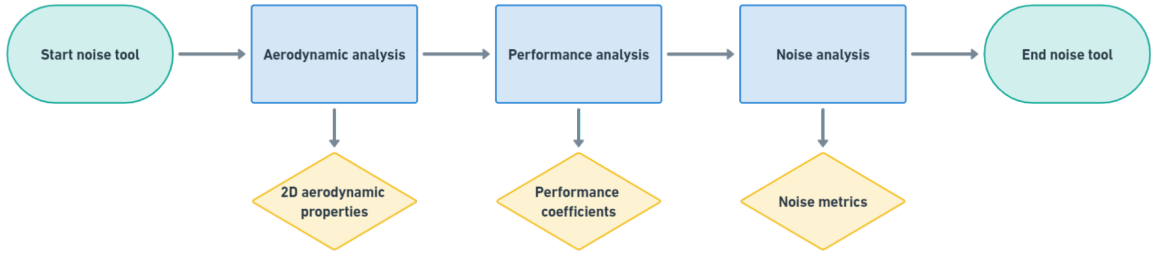


Figure 2: Flow chart of a general isolated propeller noise model

For both tools, the aerodynamic analysis consists of defining the operating conditions and propeller geometry. This is followed by determining the 2D aerodynamic properties per propeller blade section with XFOIL, which are needed for the performance analysis. XFOIL is a tool designed by M. Drela [10], and can be used to develop and analyse airfoils. The input for XFOIL consists of the airfoil coordinates of the analysed propeller, the Reynolds number per blade section (Re), and a range of angle of attack (α) values. Consequently, the output of XFOIL are the $C_l - \alpha$, $C_d - \alpha$ and $C_m - \alpha$ distributions. These outputs can then be used as the inputs for the performance analysis.

The objective of the performance analysis is to obtain the power coefficient (C_p), the thrust coefficient (C_t), and the radial loading distribution, which is needed to predict the loading noise of a propeller. For the performance analysis, both tools use a blade element model. Blade element models involve breaking down each blade of a propeller into small segments. It is assumed that each segment acts aerodynamically as a wing in a 2D flow. The lift and drag coefficients of each segment are considered functions of the local angle of attack, Mach number, and Reynolds number. These parameters in turn depend on the cross-sectional resultant velocity (V_{eff}), which is determined by combining the contributions from the axial flight velocity (V_F), rotational velocity ($\Omega \cdot r$), and induced velocity. While the axial velocity and the rotational velocity stem from the flight conditions, the induced velocity components remain unknown. To determine these unknowns, it is necessary to complement the blade element model with another model, and on this point the NLR tool and Helix tool differ. The NLR tool uses a standard BEMT model in combination with a Newton Raphson iteration to compute the induced velocity components. How the model is implemented is described in more detail in Geng et al. [11]. On the other hand, the Helix tool uses an external tool called XRotor [12]. XRotor utilises a propeller lifting line theory that employs an iterative approach to compute the circulation and induced velocities. When all the components of the cross-sectional resultant velocity are computed, it is possible to determine the inflow angle (ϕ). Subsequently, the angle of attack is derived by subtracting the inflow angle from the local pitch angle (β). Ultimately, the lift and drag per radial position can be computed following Equation 1 and Equation 2 respectively, where $C_l(\alpha, M, Re)$ and $C_d(\alpha, M, Re)$ are the corresponding 2D aerodynamic properties obtained in the aerodynamic analysis.

$$L'(r) = \frac{1}{2} \cdot \rho \cdot V_{eff}(r)^2 \cdot c(r) \cdot C_l(\alpha, M, Re) \quad (1) \quad D'(r) = \frac{1}{2} \cdot \rho \cdot V_{eff}(r)^2 \cdot c(r) \cdot C_d(\alpha, M, Re) \quad (2)$$

²The performance analysis is in fact a 3D aerodynamic analysis, but will be referred to as performance analysis to avoid confusion

The final step is to compute the noise emitted by an isolated propeller, for which both tools use the same methodology. This methodology is better known as the Helicoidal Surface Theory (HST). This theory was developed by Hanson, and predicts the propeller noise characteristics in the frequency domain. The advantage of the model being in the frequency domain is that the equations are straightforward enough to be coded on a personal computer. Following this methodology, both models have implemented the thickness noise and the loading noise as the main contributors, as in this study only tonal noise is taken into account. Furthermore, for this comparison the source noise will be used to compare both models, which means that the propagation effects are not included. The equations of the Helicoidal Surface Theory are derived in full detail in Hanson [13], but the most important equations will be introduced below. In his analysis, Hanson made the assumption that the thickness and loading sources act on the advance helix, which is the surface swept by a radial line rotating at a specific angular velocity, and moving forward with the flight speed. By determining the angle of attack relative to the helical surface (which is done in the performance analysis), the loading of a propeller blade can be computed. With this information the thickness and steady loading noise can then be modelled following a set of mathematical expressions, for which Equation 3 is the end result, which models the acoustic pressure of an isolated propeller.

$$p(t) = 2Re \left[\sum_{m=-\infty}^{\infty} P_{mB} \exp(-imB\Omega t) \right] \quad (3)$$

In the above equation, P_{mB} represents the Fourier transform of the pressure at the m^{th} harmonic of the BPF. The variable B represents the number of blades, and Ω denotes the angular frequency associated with the propeller rotational speed. Furthermore, the term P_{mB} consists of three components. P_{Vm} is the volume displacement component, which can be calculated using Equation 4. P_{Dm} represents the drag dipole, which can be calculated using Equation 5, and P_{Lm} stands for the lift dipole, which can be calculated using Equation 6. P_{mB} is then calculated by adding these components together. It should be noted that the quadrupole sources from the original theory are omitted in this paper. This decision was made as these sources account for the rise of non-linear effects that occur at high Mach numbers, and in this study only Mach numbers were considered up to where compressibility effects have a negligible impact.

$$P_{Vm} = -\frac{\rho_0 c_0^2 B \sin\theta \exp \left[imB \left(\frac{\Omega_D r}{c_0} - \frac{\pi}{2} \right) \right]}{8\pi \left(\frac{y}{D} \right) (1 - M_x \cos\theta)} \cdot \frac{1}{2} \int_{root}^{tip} M_r^2 e^{i(\phi_s)} J_{mb} \left(\frac{mBz M_t \sin\theta}{1 - M_x \cos\theta} \right) \cdot 2k_x^2 t_b \psi_V(k_x) dz \quad (4)$$

$$P_{Dm} = -\frac{\rho_0 c_0^2 B \sin\theta \exp \left[imB \left(\frac{\Omega_D r}{c_0} - \frac{\pi}{2} \right) \right]}{8\pi \left(\frac{y}{D} \right) (1 - M_x \cos\theta)} \cdot \frac{1}{2} \int_{root}^{tip} M_r^2 e^{i(\phi_s)} J_{mb} \left(\frac{mBz M_t \sin\theta}{1 - M_x \cos\theta} \right) \cdot ik_x C_D \psi_D(k_x) dz \quad (5)$$

$$P_{Lm} = -\frac{\rho_0 c_0^2 B \sin\theta \exp \left[imB \left(\frac{\Omega_D r}{c_0} - \frac{\pi}{2} \right) \right]}{8\pi \left(\frac{y}{D} \right) (1 - M_x \cos\theta)} \cdot \frac{1}{2} \int_{root}^{tip} M_r^2 e^{i(\phi_s)} J_{mb} \left(\frac{mBz M_t \sin\theta}{1 - M_x \cos\theta} \right) \cdot ik_y C_L \psi_L(k_x) dz \quad (6)$$

In these equations θ stands for the radiation angle from the propeller axis to the observer, y represents the vertical distance between the observer and the propeller axis, r stands for the distance to the observer, D is the propeller diameter, M_x , M_r and M_t represent the flight, effective and rotational tip Mach number respectively, ϕ_s is the phase lag due to propeller blade sweep, J_{mB} is the first order Bessel function, z represents the radial position, C_L and C_D correspond with the lift and drag coefficient of the blade section, i represents the imaginary unit, and t_b stands for the thickness to chord ratio. Furthermore, Ψ_V , Ψ_D and Ψ_L stand for the thickness, drag and lift distributions, and k_x and k_y represent the non-dimensional wave numbers, which can be computed with Equation 7 and Equation 8 respectively, in which the variable B_D represents the chord to diameter ratio.

$$k_x = \frac{2mBB_D M_t}{M_r (1 - M_x \cos\theta)} \quad (7)$$

$$k_y = \frac{2mBB_D}{z M_r} \left(\frac{M_r^2 \cos\theta - M_x}{1 - M_x \cos\theta} \right) \quad (8)$$

2.1.1 Verification

In this section, the results from both models are compared to literature data. This is done to assess the performance and the acoustic signature of an isolated propeller. For the performance analysis, the SR-2 propeller has been selected, as an extensive data set is available for this propeller. The data is obtained from Stefko [14], where measurements were taken for an 8-bladed SR-2 propeller in the NASA Supersonic Wind Tunnel. For the

acoustic analysis, both models are compared to experimental data obtained from Block (test case 1) [15], and from a full-scale outdoor experiment, which was conducted by Elbers (test case 2) [16]. Block [15] performed an experimental study on the SR-2 propeller to measure propeller noise. For test case 2, the Pipistrel Velis Electro was used in combination with the propeller configuration described in Elbers [16]. This aircraft is a fully-electric aircraft, which makes it a very suitable aircraft to compare both models with, as the propeller noise will be the primary noise source of this aircraft due to its electric engine.

Performance results

In Figure 3(a) and Figure 3(b), the thrust and power coefficient respectively are presented as a function of the advance ratio for a freestream Mach number of 0.2 and a blade setting of 45.8 deg. This operating condition was chosen as, according to Stefko [14], it represents the operating condition experienced during initial climb-out. The results reveal that there is excellent agreement between the literature data and the values computed by both models at high advance ratios. However, at lower advance ratios (or static conditions), the agreement diminishes. This deterioration can be attributed to substantial blade elements entering a stalled condition. The blade element model, relying on two-dimensional aerodynamic data, struggles to predict the intricate three-dimensional stall behaviour of these blade cross sections. This is also the reason why the Helix tool fails to converge for the complete range of advance ratios, as XRotor does not provide results for blade segments in stalled conditions. Furthermore, at lower advance ratios, the induced velocity's magnitude increases, amplifying its impact on the propeller's performance, and consequently the differences between the models become more apparent. It can be seen that the Helix tool seems to overpredict the data obtained in literature, while the NLR tool underpredicts the values for both performance coefficients. This finding is in accordance with the conclusions drawn in the research conducted by Gur [17], where several blade element models are compared.

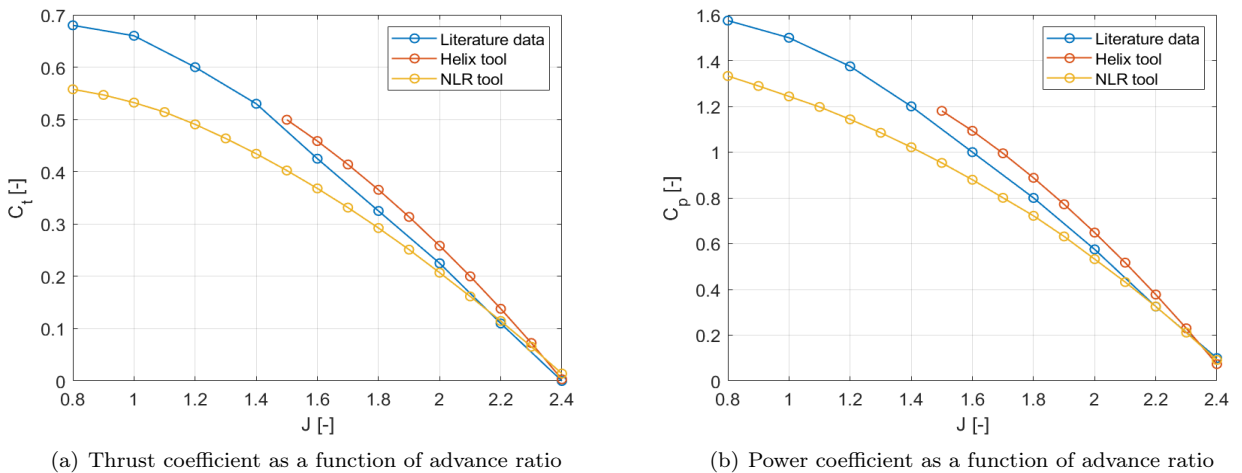


Figure 3: The thrust and power coefficient for an axial Mach number of 0.2 and $\beta_{0.75} = 45.8$

Acoustic results

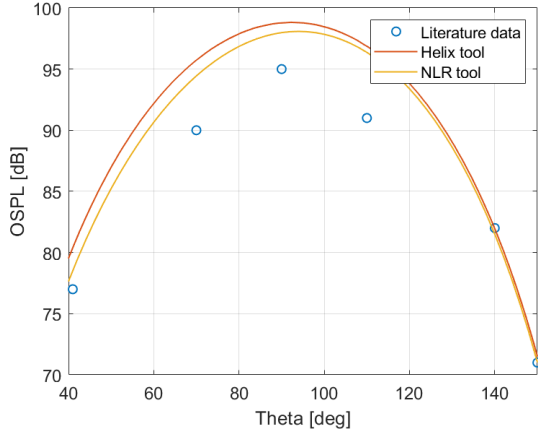
For the acoustic verification, both models have been compared to experimental data. The input parameters for the different cases can be found in Table 1. The results of test case 1 are presented in Figure 4(a). It can be seen that both models show relatively good agreement with the measured data for the angles ranging from 40 deg to 150 deg. The maximum OSPL value obtained from the measurements is 95 dB, whereas both models compute a maximum OSPL of around 98 dB. It can be seen that for the lower and higher emission angles both models show even better resemblance to the literature data. A possible explanation for the 3 dB difference at 90 deg between the models and the literature data is that in the research conducted by Block [15], the wind tunnel was not perfectly acoustically treated, and to account for pressure doubling at the hard surfaces, 6 dB was subtracted from the measured pressure levels, which could potentially be an overestimation of the reality.

Besides the results of test case 1, the results of the comparison with the flyover experiment can be found in Figure 4(b). It can be observed that, similarly to test case 1, the OSPL has been predicted relatively well by both models. The peak OSPL value measured is 98 dB, and both models predict an OSPL of roughly 101 dB. The difference between the graphs of the two models can be attributed to how the different noise components have been modelled. A visual representation of this comparison is presented in Figure 5. It can be seen that the thickness noise graphs of both models show great resemblance, but that there are small discrepancies between the graphs of the lift and drag noise. These differences are a result of the different radial loading computations of

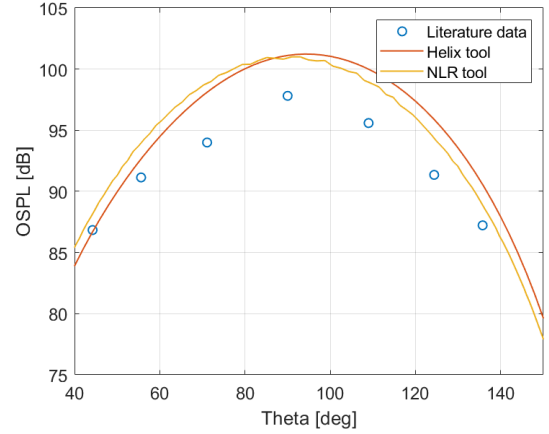
both models. The Helix tool, for example, computed a power coefficient of 0.076, where the NLR tool predicted a power coefficient of 0.045. Following the definition of the power coefficient, it can be determined that, with a similar drag, a higher power coefficient will result in a higher power, which on its turn will result in a higher noise level due to a higher loading. The difference in loading noise between the two models is also the reason for the shift between the two graphs, where the peak OSPL value of the Helix tool can be found at a higher emission angle due to the noise component of the lift pushing the peak to the right in Figure 4(b).

Table 1: Input parameters for the different test cases

	M_x [-]	J [-]	y [m]	n_{blades} [-]	$\beta_{0.75}$ [deg]
Test case 1	0.09	0.592	0.889	4	20.6
Test case 2	0.12	0.597	12.19	3	18



(a) Case 1: Directionality plot comparing experimental data from Block [15] with both models



(b) Case 2: Directionality plot comparing flyover data from Elbers [16] with both models

Figure 4: Directionality plots of test cases 1 and 2

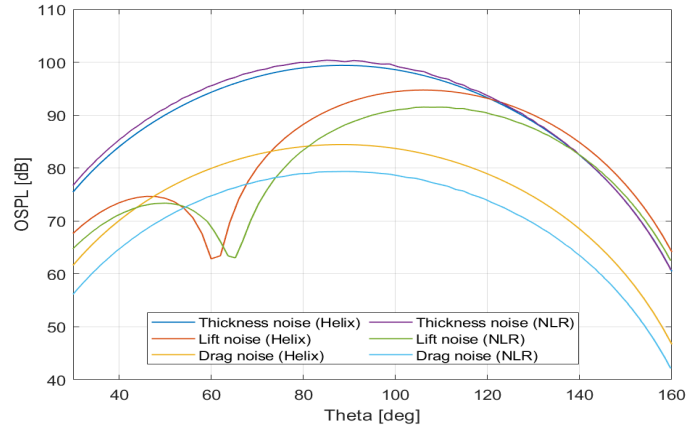


Figure 5: Directionality plot of all noise components computed by the Helix and NLR tools

2.2 DEP configuration

A noise sample of a DEP aircraft flyover is created by following the methodology presented in Figure 6. It can be seen that the DEP model consists of four major parts, referred to as: the aerodynamic analysis, the performance analysis, the source noise computation and the auralization. First of all, a reference aircraft with a corresponding propeller blade must be selected. This aircraft will determine a number of input parameters for the DEP model, such as the locations of the propellers and the aircraft's operating conditions. With the propeller geometry known, it is possible to determine the 2D aerodynamic properties with XFOIL, as described in more detail in section 2.1. For this research, the aircraft concept developed by Maeve Aerospace, known as Maeve-01, has been selected as the reference aircraft. Its respective results will be presented in section 4.

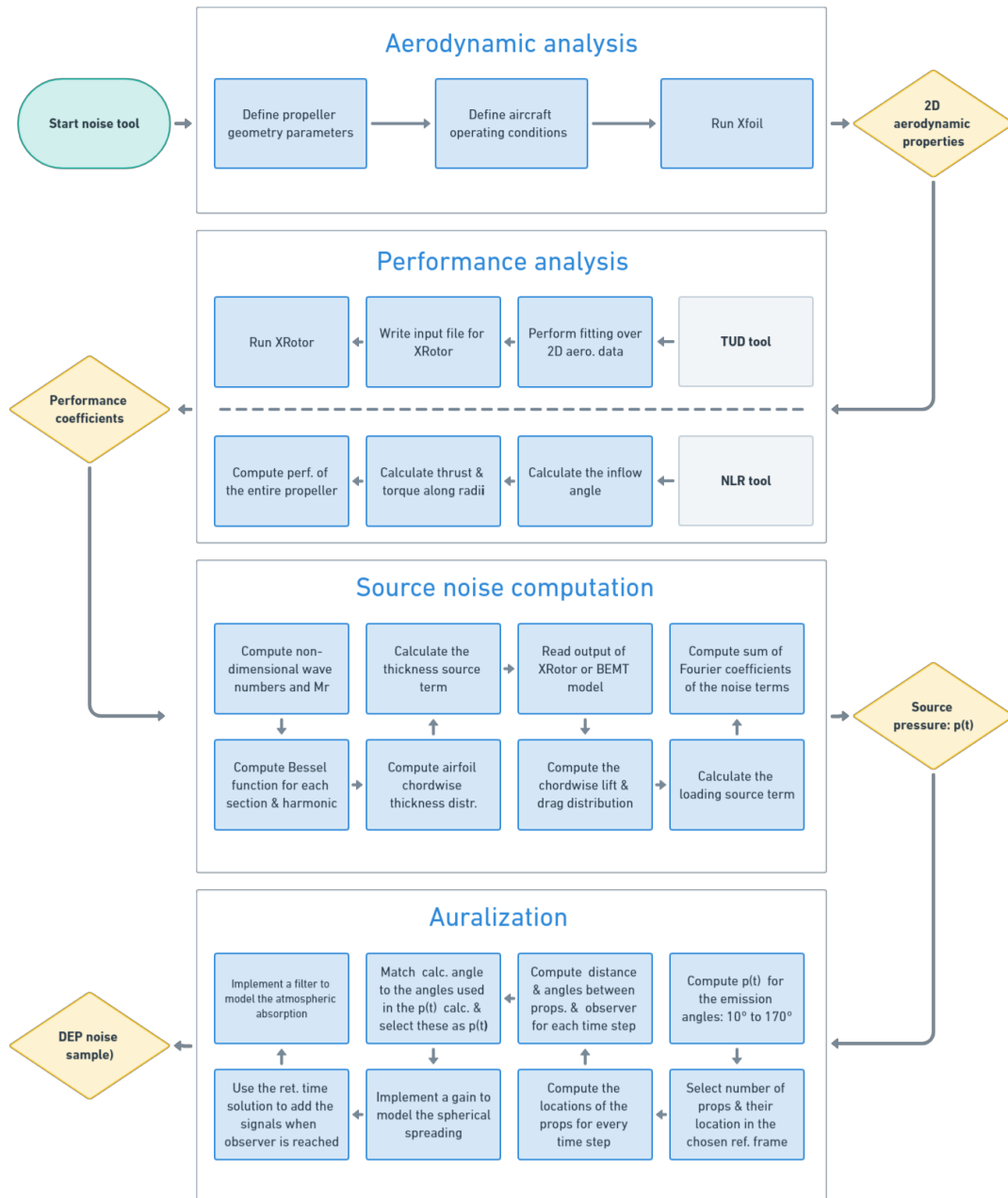


Figure 6: Flowchart of the DEP model

Secondly, the propeller performance and the source noise will be computed using the isolated propeller models from Delft University of Technology (Helix) and NLR. It was chosen to adopt both models in the research. The NLR tool will mainly be used for validation purposes, as it is more computationally intensive than the Helix tool. The Helix tool runs several orders of magnitude faster and will therefore be the main tool that will be used to identify and analyse the acoustic effects of the distributed propeller configuration. First, the performance coefficients and the radial loading will be computed using the performance prediction tools. Computing the source noise is done by following the Helicoidal Surface Theory, and, consequently, pressures at a specific distance for a range of emission angles are computed. By doing so, a database is created with the pressures at specific emission angles. In the auralization step the actual emission angles for a given observer position will be computed, and these will subsequently be matched to the corresponding source noise pressures from the database.

Finally, the source noise needs to be processed to incorporate the propagation effects, and the single propeller noise sample should be expanded to include the noise of multiple propellers. In order to apply the propagation characteristics to the source noise, three primary Digital Processing Steps (DPS) are required: a gain, a delay line, and a filter.

The first propagation effect that is accounted for in the DEP model is known as spherical spreading. The theory behind the spreading loss is based on the fact that when a sound wave moves away from a noise source, it spreads out in all directions, forming a spherical wavefront, causing the intensity of the sound wave to diminish further away from the source. This is accounted for by incorporating a gain, which scales the source pressure amplitude based on the additional distance travelled to the observer, i.e., R_s/r_n . To clarify, R_s is the distance at which the source pressure has been computed, and r_n is the additional distance to the observer.

Subsequently, the DEP model uses the retarded-time solution of the Ffowcs Williams and Hawkings (FWH) analogy to simulate the noise of multiple propellers. This analogy evaluates the signal received at a given time t through summation of all the disturbances reaching the observer at that same time t . These disturbances are potentially emitted at different times and cover different distances before reaching the observer. A technique to address this phenomenon involves the utilisation of a Variable Delay Line (VDL), accounting for the time it takes for the signal to travel from the source to the observer. For situations involving moving sources or observers, the VDL intrinsically accounts for the Doppler shift as well, solving two problems at once. The operation of the VDL is described in full in Casalino [18], but can be summarised as follows:

$$y[n] = x[n - m[n]], \quad (9)$$

where $m[n]$ represents the time varying delay, which can be computed by multiplying the sampling frequency with the time it takes for the sound wave to reach the observer. This will result in the amount of samples the signal needs to be delayed for. For example, consider an audio signal that is sampled at 50.0 kHz, which means that an audio sample is stored at every $1/50 = 0.02$ ms. Additionally, suppose the propagation distance between the source and receiver is 1 meter, which results in a travel time of 2.94 ms, at a speed of sound of 340 m/s. This results in a delay of $2.94/0.02 = 147$ samples, which means the audio signal needs to be held by 147 samples in a buffer before integrating it to the audio signal that reaches the observer. In this example, the delay is composed of an integer amount of samples, but it is also possible to have a fractional number of samples. The fractional part also needs to be considered, because ignoring it will result in audible aliasing effects as pieces of the signal are being neglected. Including the fractional part is essentially an interpolation task. Throughout this paper, spline interpolation will be used to incorporate the fractional delays as this minimises the chances of aliasing occurring due to waveform gradients being taken into account [19]. This process will be repeated for every propeller over the entire time span of the flyover, and subsequently all the noise signals can be summed up at the time t at which the signals reach the observer.

Lastly, when an aircraft is airborne, its produced sound waves propagate through the atmosphere to reach an observer on the ground. During this process, a portion of the sound energy is absorbed by the atmosphere, which leads to a decrease in sound level at the observer. This phenomenon arises due to the interaction of an acoustic wave with molecules in the atmosphere during propagation, wherein energy is transferred from translational motion to rotational and vibrational modes upon collision. This energy transfer is directly linked to the relaxation time, which represents the duration necessary for a molecule to attain equilibrium following excitation [19]. The extent of this energy loss is determined by the sound attenuation coefficient, which depends on the frequency of the sound wave, and the humidity, pressure and temperature of the atmosphere. Following the fact that the unit of the attenuation factor is dB/m , the attenuation of the sound energy will increase with an increase of the aircraft's altitude as the sound wave must travel through a larger portion of the atmosphere. In order to account for atmospheric absorption, a FIR filter has been included in the DEP model for every propeller signal, using the approach of Arntzen [19].

Combining the theory of the propagation effects with the theory of the Helicoidal Surface Theory, the pressure-time signal of a DEP aircraft can be computed with Equation 10. It should be noted that atmospheric absorption still needs to be accounted for in the signal created by Equation 10, where N_p represents the number of propellers in the analysed configuration. A visual representation of the auralization process is presented in Figure 7 for a configuration with two propellers, but can easily be extended to more propellers by following the same steps. It can be seen that for each propeller two sound waves reach the observer, i.e., one represents the direct wave and the other stands for the sound wave that is reflected from the ground. This takes into account that when an acoustic wave encounters a surface, it is reflected and/or absorbed. If the surface is rough, the reflected wave can scatter in various directions, resulting in diffuse reflection. An often convenient assumption is to consider specular reflection, where the sound is fully reflected in the direction perpendicular to the incident field, which is also how the ground reflection has been modelled in the DEP model.

$$p(t) = \sum_{n_p=1}^{N_p} \sum_{m=1}^m 2Re \left[\frac{R_s}{r_n} P_{mB} \exp(-imB\Omega(t - t_0)) \right] \quad (10)$$

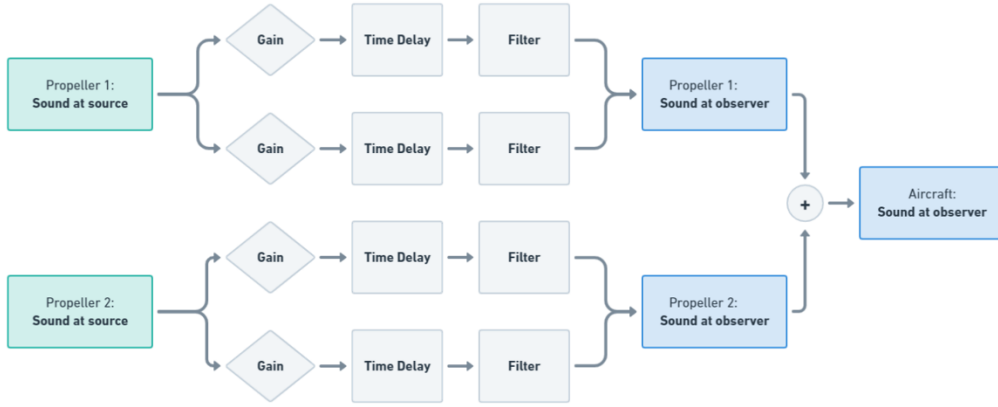


Figure 7: The required steps to incorporate the propagation effects in a multi-propeller configuration

2.2.1 Verification

The verification of the DEP model consists of two parts. First of all, numerous unit tests have been conducted to ensure the accurateness of the model. An example of such a unit test is a control check to see if the interference effects have been incorporated correctly. To verify this, a configuration with two propellers was selected, and their produced pressure-time signals were replaced with simple sine functions. For this unit test, two scenarios have been analysed. The first one is when the propellers are located in the same position but on opposite wings with the observer right underneath the aircraft. In this scenario, the distance from both propellers to the observer should be the same, which consequently should lead to constructive interference at the observer. The aircraft configuration and the result of this scenario are presented in Figure 8. It can be seen that the signals of both propellers indeed reach the observer at the same time and as a result constructive interference occurs.

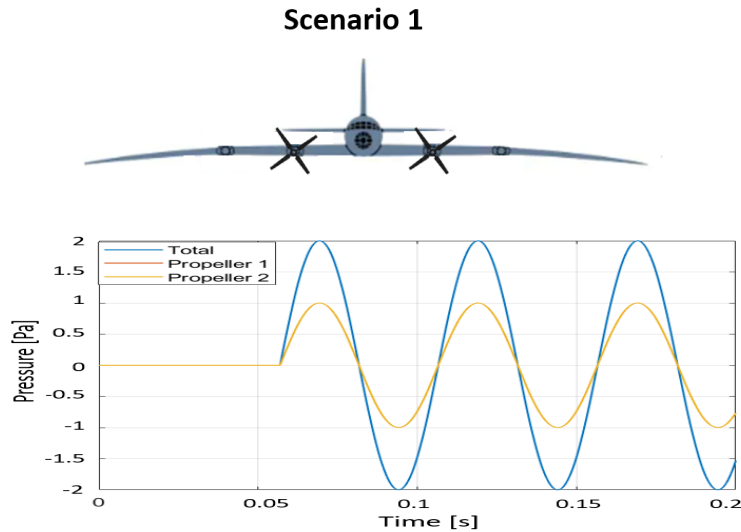


Figure 8: Scenario 1, with both propellers located 4 m from the middle on opposite wings

In the second scenario, the location of one of the propellers is changed in such a way that the signals from both propellers should be out of phase at the observer, leading to destructive interference. In a scenario where one propeller is located 4 m from the middle, and the aircraft is 20 m above the ground, the position of the second propeller can be calculated as follows. First, the time it takes for the signal from propeller 1 to reach the observer should be calculated. This can be achieved by dividing its distance by the speed of sound, and was calculated to be 0.05946 s. Subsequently, a δt should be added to this value to incorporate the phase shift between the propeller signals. This δt can be calculated by dividing the total running time by the number of local maxima of the sine wave, i.e. $(1/BPF)/2$. In this case the model was run for 0.25 s, and there were 10 local maxima, therefore the δt was calculated to be 0.02500 s. This means that the wave produced by propeller 2 will take $0.05946 \text{ s} + 0.02500 \text{ s} = 0.08446$, which results in a distance of 28.97 m from the observer to propeller 2. From this distance, the propeller location can be computed using the Pythagorean theorem, keeping the 20 m altitude in mind. In the end, the hypothetical location of propeller 2 was calculated to be at 21 m on the other wing. With these input parameters the model was run, and if the interference in the model works correctly, it

is expected to observe destructive interference for this scenario. The results are presented in Figure 9, and, as expected, there indeed occurs destructive interference, as both propeller signals are out of phase.

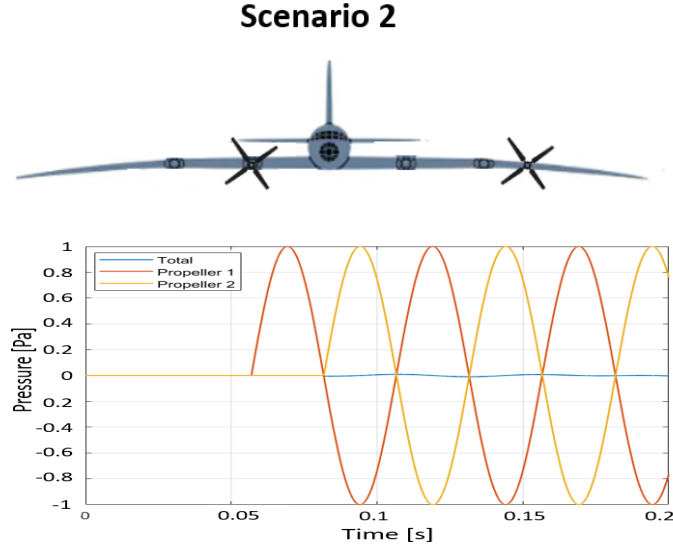


Figure 9: Scenario 2, with one propeller placed 4 m from the middle, and the second propeller located 21 m from the middle on the opposite wing, results in destructive interference

For the second part of the verification, the fact that loading and thickness noise exhibit axisymmetry around the axis in the flight direction is utilised. Consequently, the directivity patterns of multiple propellers can be assessed by comparing them to configurations of basic monopole sources along the axis orthogonal to the flight direction, i.e., along the wing span. Blackstock [20] has outlined that the directivity pattern of two monopoles separated by a distance d follows a pattern that can be modelled with Equation 11. While the patterns are dependent on the separation distance d , it can be seen that, besides the separation distance, the acoustic wave number k is also present in the equation. Combined, the variable kd is known as the compactness ratio, and needs to be included, because a doubling of the frequency and a halving of the separation distance yield the same results.

$$D(\phi) = \cos\left(\frac{kd}{2} \sin(\phi)\right) \quad (11)$$

In Figure 10, the interference patterns modelled by Equation 11 are compared to the directivity patterns produced by the DEP model. The DEP model shows acceptable results with Blackstock, in particular at low kd . As kd increases, some deviations arise at specific emission angles, i.e., it can be seen that the DEP model underestimates the minimum values predicted by Blackstock. The hypothesis is that the model underestimates the minima because, firstly, only the distance between the propellers was changed in the DEP model in this verification step, and secondly, the model was run for five harmonics instead of only the BPF, which means that the exact values of $kd/2$, and therefore the emitted sound waves, between the model and Blackstock are slightly different. However, it can also be observed that the model does follow the same shape as Blackstock's plot, which confirms the functioning of the interference modelling in the DEP model.

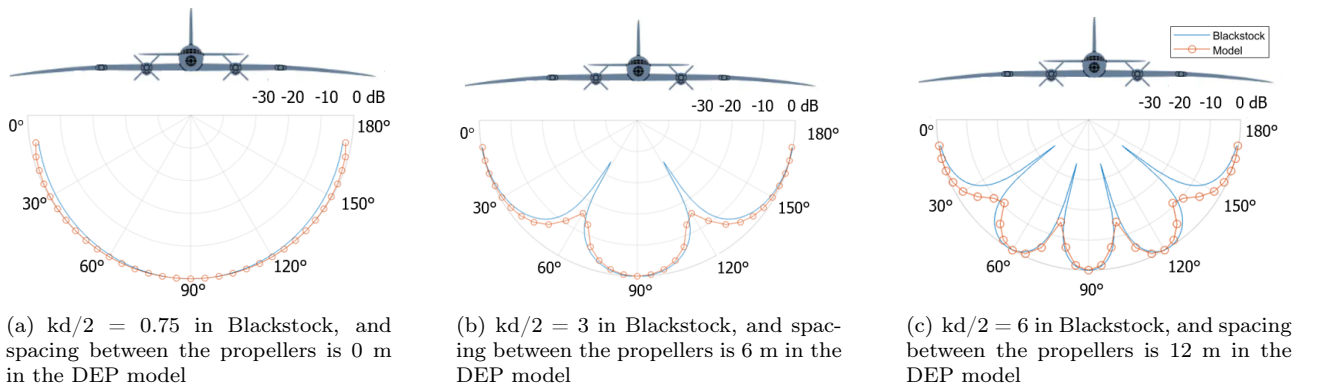


Figure 10: In-plane directivity of a two propeller simulation with different spacing between the propellers

3 Validation

The validation of the model is divided into two parts. First of all, the model will be validated with the research performed by Guerin [9] and Rizzi [21]. In both papers, the tonal contributions of a DEP configuration flyover have been analysed for a reference aircraft. In this part of the validation, the directivity plots presented in Guerin and the heat maps produced by Rizzi will be compared to the output as developed in this research. The second part of the validation consists of comparing the outcome of the DEP model with real-life flyover experiments of a drone with four propellers.

3.1 Literature

In this section, the DEP model will first be compared to the results produced by Guerin et al. [9]. They have analysed the acoustics of the regional aircraft investigated in IMOTHEP [22]. This aircraft is a distributed electric propeller configuration with eight identical propellers, and is visually depicted in Figure 11(a). Each of the eight propellers has five blades, which have a diameter of 2.6 m. The exact propeller coordinates can be found in Guerin [9], and should be modified accordingly in the DEP model. Additionally, it is assumed that all propellers operate at the same speed and generate the same thrust. A summary of the operating conditions used in Guerin [9] can be found in Table 2. It should be noted that Guerin uses a propeller blade geometry that is not available to the general public. For that reason, the model uses the propeller blade geometry introduced by Elbers [16] as input, but with the same operating conditions used in Guerin’s research.

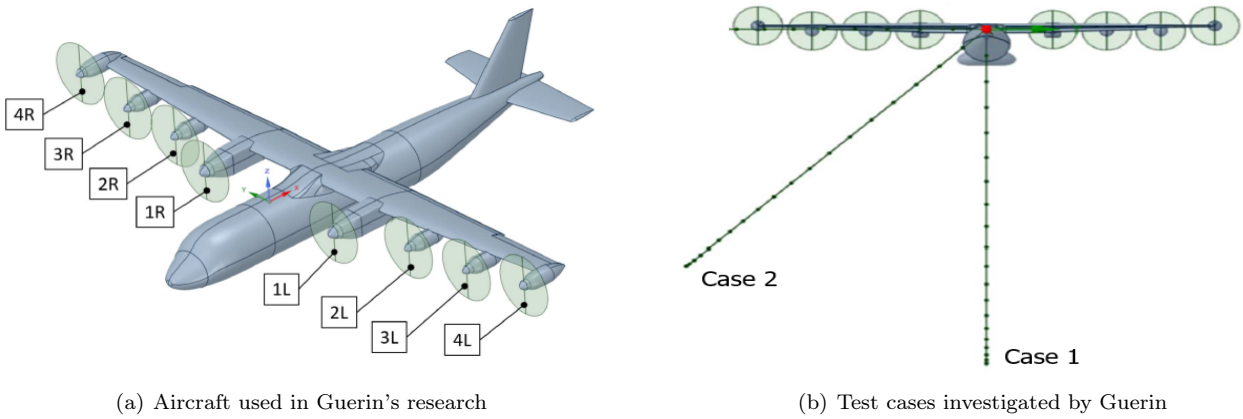


Figure 11: Research conducted by Guerin [9]

Table 2: Operating conditions used in Guerin [9]

Mach	Propeller RPM	Altitude [m]	Number of blades	Propeller diameter [m]	$\beta_{0.75}$ [deg]	J
0.31	1350	260	5	2.6	40.67	1.82

Guerin analyses two test cases with the observer located at different azimuthal angles ϕ , i.e., the axis along the wing span. First of all, the noise directivity is predicted when the observer is located exactly underneath the flight path in test case 1. Thereafter, a scenario is analysed when the observer is located at the azimuthal angle of 45 deg in test case 2. For both test cases the observer is located at a distance of 260 m. Both test cases are visually presented in Figure 11(b). Guerin’s results and the results obtained from the DEP model are compared in Figure 12(a) and Figure 12(b) for test cases 1 and 2 respectively. The agreement is satisfactory. For test case 1 it can be seen that the absolute levels agree particularly well for the higher emission angles. However, it must be said that there are some discrepancies between the shape of the (orange and blue) graphs for the lower emission angles, i.e. at 60 deg there is a difference of 20 dB. These differences can be clarified by realising that a different propeller geometry has been used to validate the model, i.e., for the used propeller geometry in the DEP model the thickness noise was the main noise contributor, which as presented in Figure 5 shows symmetrical behaviour. On the other hand, the main noise contributor for Guerin’s propeller was stated to be the steady loading noise, which, as presented in Figure 5, sometimes features a curve in the directivity plot. The hypothesis is that, with a more similar propeller geometry, the shape of both graphs will become more alike. This hypothesis was tested by altering the propeller used in the DEP model by making it thinner to reduce the influence of the thickness noise on the total directivity plot. The results of this analysis are presented in Figure 12(a), as the yellow graph. It can be seen that the shape of the obtained directivity plot indeed shows better

resemblance to the plot presented in Guerin’s research. However, to be absolutely certain that the differences between the graphs can be attributed to the used propeller, it is necessary to run the DEP model in the future with the propeller used in Guerin’s research to increase the confidence in the DEP model. For test case 2 it can be seen that for both graphs the noise directivity is no longer axisymmetric due to the interference effects between the propellers. Similar to test case 1, it can be seen that the overall noise levels between Guerin and the DEP model are comparable, and that the shapes of the graphs again present some differences. All in all, the model shows adequate results when being compared to test cases 1 and 2, and it was observed that with a more comparable propeller the shape of the graphs becomes more similar.

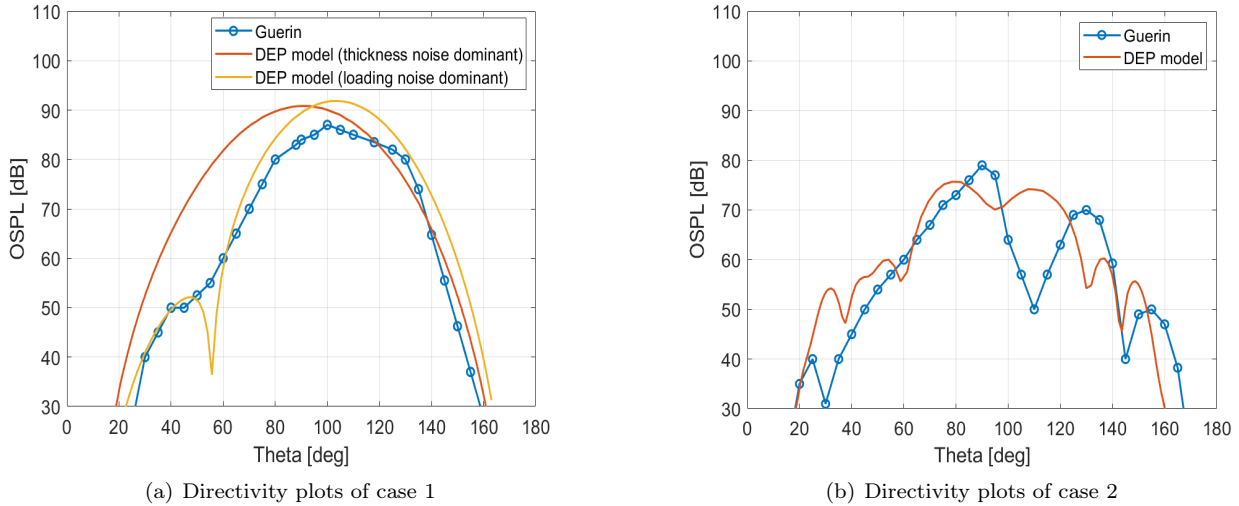


Figure 12: OSPL directivity comparison of case 1 and 2 between Guerin’s results and the developed DEP model

Now the DEP model will be compared to the heat maps produced by Rizzi et al. [9]. In their paper, Rizzi et al. have introduced a noise prediction scheme for a DEP aircraft, which they have applied to a specific vehicle configuration, namely, the Greased Lightning-10, which is presented in Figure 13. The DEP configuration comprises eight propellers distributed along the wingspan and two propellers positioned on the tail. Each propeller has a diameter of 0.4064 m, and is constructed with three AeroNaut 16x8 CAM folding carbon blades. The right side of Figure 13 shows a schematic of the propeller locations as a fraction of half the wing span, which in this case equals 1.6 m. Furthermore, it can be seen that the propellers are labelled $n_1 - n_{10}$ and that the propellers are installed on a swept wing with an angle of 10.6 deg.

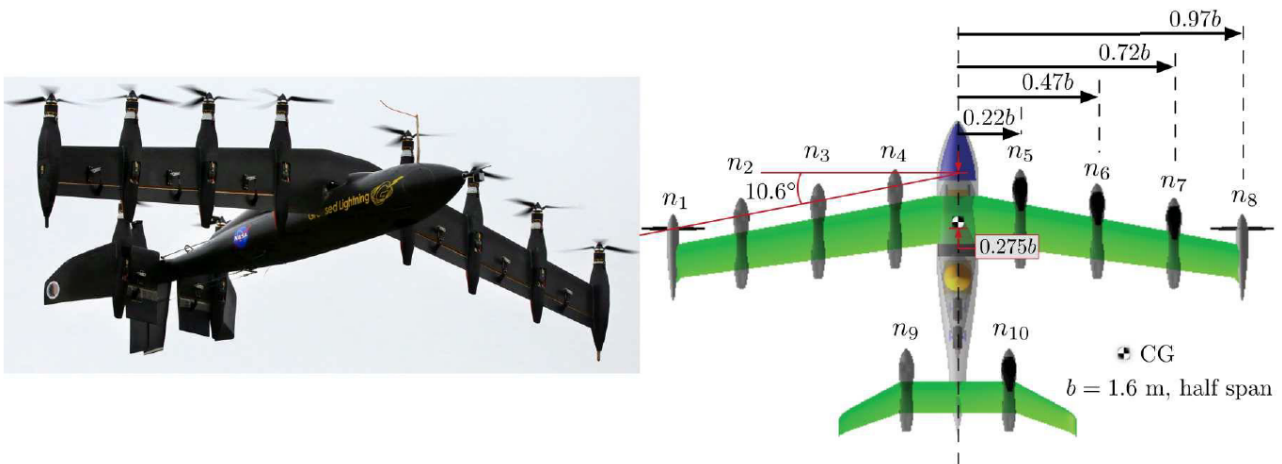


Figure 13: GL-10 in hover mode (left) and top view of the forward flight configuration (right) [21]

The total noise from the GL-10 configuration will now be discussed. Rizzi states that the noise contours on the ground exhibit a comparable dependence on the acoustic wave number as explained in the verification example in section 2.2.1. What he means by this is that lower rotation rates, i.e., lower frequencies, have a tendency to generate a wider main lobe directly beneath the aircraft. This can be explained by realising that lower rotation rates result in lower acoustic wave numbers, which in turn decreases the compactness ratio, resulting in an

increase of the main lobe width as shown in Figure 10. Consequently, Rizzi decided to verify if his approach was modelled correctly by introducing two scenarios, one with the propellers rotating at 3,500 RPM, and for the other, he increased the RPM to 8,000, while keeping the advance ratio constant at $J = 0.6$. The DEP model was run for the same operating conditions with the aircraft located at an altitude of 30.5 m. The DEP model was run numerous times for a period of 0.2 s with the observer location changing in increments of 5 m every run. In order to compute the noise levels at the remaining observer locations linear interpolation between two known points was applied. The results of Rizzi and the DEP model are presented in Figure 14. Note that all noise contours are normalised by subtracting the maximum value per case. It can be seen that there are some differences present between the heat maps produced by the DEP model and Rizzi's model. The main difference that can be observed is that Rizzi predicts the noise behind the aircraft to be greater than the noise in front of the aircraft, which is not visible in the plots generated by the DEP model, which show more symmetrical behaviour over the axis in the flight direction. A first suggestion to why this could be, is that different propellers were used for both analyses. Rizzi used a propeller where the loading noise was dominant for all observer locations, which suggests that Rizzi's directivity plots have a similar shape as Guerin's directivity plot in Figure 12(a). Guerin's directivity plot shows that for the low emission angles, which correspond to the area in front of the aircraft, the OSPL values are significantly lower than the OSPL values for the higher emission angles, which correspond to the area behind the aircraft. Following this reasoning, it is logical that a heat map of a propeller where the loading noise is dominant shows the behaviour predicted by Rizzi, i.e., it can be observed that the OSPL values behind the aircraft are higher than the OSPL values in front of the aircraft. In the appendix, a heat map is plotted of a propeller where the loading noise was dominant, to verify whether the DEP model would also predict the noise levels to be greater behind the aircraft in such a scenario. Even though there are still differences visible between both heat maps, it can be seen that the noise levels predicted by the DEP model are indeed higher behind the aircraft than in front of the aircraft, and that generally more similar patterns arise between both heat maps. Furthermore, it can also be observed that Rizzi's heat maps vary over the axis along the wing span, and the heat maps produced by the DEP model do not. This difference can be explained by realising that Rizzi's model takes into account the rotation direction of the propellers, which is not considered in the DEP model. Therefore, the DEP model is symmetrical over the axis along the wing span. Besides the differences, it can be seen that the elementary expectation that the main lobe width decreases with higher rotation rates holds for both models. Furthermore, it can also be seen that for both models at the higher rotation rate secondary side lobes are present next to the main lobe.

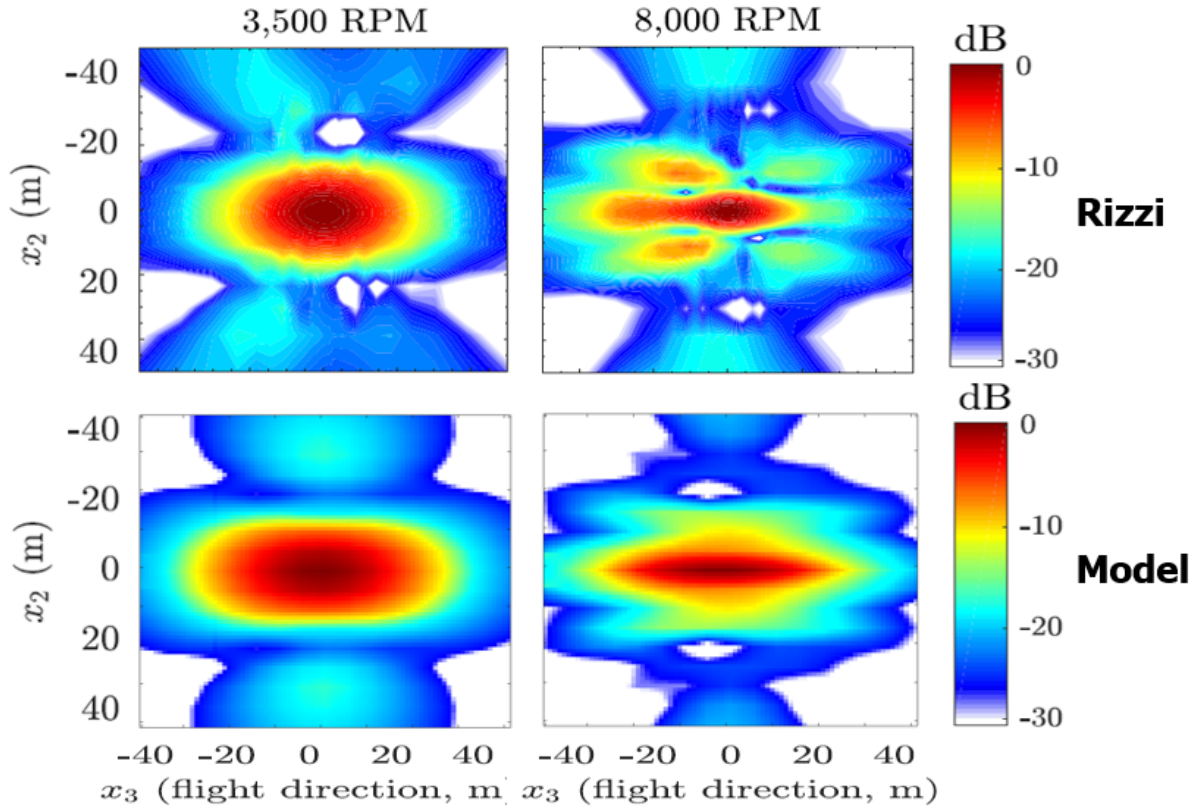


Figure 14: Noise contours comparison between the results produced by Rizzi and the DEP model

3.2 Experiments

In addition to validating the model based on literature data, real-life flyover measurements were performed. These measurements were performed with the drone presented in Figure 15(a). It can be seen that the drone is not exactly a DEP configuration. However, the drone does possess four propellers that point in the flight direction, and for lack of a more suitable configuration being available, it was assumed that since the tonal noise contributions are the main interest of this research, the drone would be a fitting configuration to validate the model with. The drone is part of the Micro Air Vehicle Laboratory (MAVLab) group at Delft University of Technology, and possesses four identical two-bladed T-Motor carbon fibre propellers with a diameter of 0.254 m. For the recordings of the drone flyover, the Bionic M-112 microphone array from CAE was used. This array has a diameter of 1 m and contains 112 microphones, which are divided over seven detachable arms. The positions of these microphones are presented in Figure 15(b). As a form of validation, beamforming has been performed on the measured data to ensure that the sound picked up by the array was in fact created by the drone. The results of the beamforming can be found in the appendix.

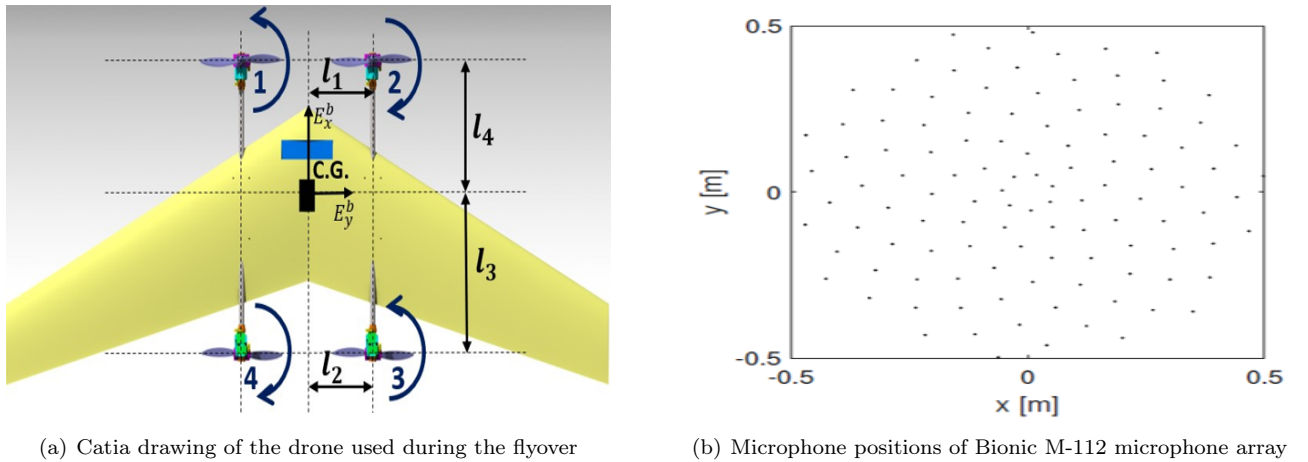


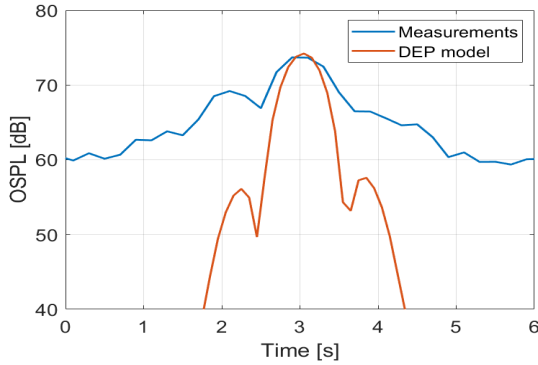
Figure 15: Experimental setup used for the flyover validation

The operating conditions of the drone during the flyover are presented in Table 3. These parameters were used as input for the DEP model in order to simulate the flyover and compare the results of the DEP model with the recorded data. The results of this flyover are presented in Figure 16. Figure 16(a) presents the OSPL over time plot. It can be seen that the maximum OSPL predicted by the DEP model shows excellent agreement with the recorded data. Both plot an OSPL of around 72 dB. However, what also stands out is that the model underestimates the OSPL values at low and high emission angles. There are two possible explanations for this. First of all, it is important to note that during the experiments there was some background noise present from a lawnmower that could have been picked up by the microphone array. The spectrogram of the flyover is included in Figure 17, and indeed shows that a constant noise is present of around 60 dB at low frequencies, which is not created by the drone. This can indicate that the microphone has picked up some type of background noise, which could be a possible explanation for the higher OSPL values at low and high emission angles. A second possibility is that in these regions the broadband noise is more dominant. This corresponds to the results presented by Guerin [9]. This finding has to be considered carefully as the interaction with the airframe and the propeller-propeller aerodynamic interaction effects are neglected in this study. The hypothesis is that it is a combination of the two possibilities, as literature tells us that broadband noise is more dominant in these regions, but by listening to the recording it was verified that at a certain point in time when the drone was no longer audible the OSPL values stayed around the 60 dB region, which indicates some type of background noise has been picked up by the array. Furthermore, it is good to realise that in this specific scenario the drone flyover happens very quickly, which means that the tonal noise contributions are restricted to a very short time period, as can be seen in Figure 16(a). In a scenario where an aircraft is climbing to its cruise altitude the tonal noise contributions will be spread out over a longer time period, for which the expectation is that the DEP model will show satisfactory agreement with the reality for a longer period of time.

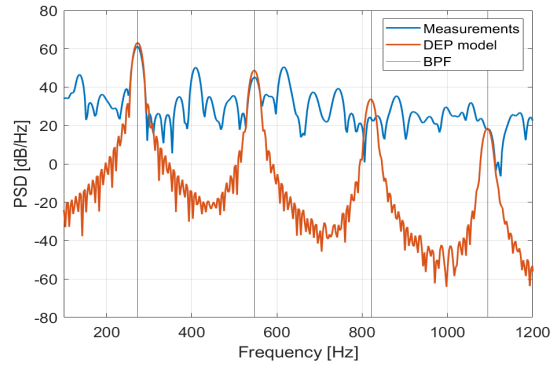
Table 3: Operating conditions and other inputs of the drone during the flyover

Flight speed [m/s]	RPM	Altitude [m]	Number of blades	Propeller diameter [m]	l_1 [m]	l_3 [m]
15	8220	15	2	0.254	0.228	0.38

In addition to the OSPL over time plot, the frequency spectrum comparison, for which a 0.1 s snapshot was taken at the peak of the pressure-time signal, is presented in Figure 16(b). The DEP model is run for four harmonics, which are clearly visible and decrease with increasing harmonics. The experimental data and the output of the DEP model have been processed by applying a Hanning window and by zero-padding the time signal. It can be seen that for the experimental data multiple tones are present in between the harmonics. The spectrogram of the flyover shows that the ground effect is notably visible at around 15 seconds, which is the time period that was taken for this comparison. The tones created by this effect could potentially explain the differences between the spectra of the experimental data and the DEP model. Furthermore, it can be observed that the RPM during the actual flyover experiment varied over time, which might also have had an influence on the differences between both spectra, as in the DEP model the RPM can only be set to a constant input value, i.e., in this case the average RPM during the flyover experiment. Additionally, a comparison between the spectra produced by the DEP model and the measurements for the time period of 3.8 to 3.9 s is presented in the appendix. It can be seen that the differences between the spectra become more pronounced when the drone is further away from the microphone array, as the spectrum from the measurements remains more constant, and the spectrum from the DEP model decreases with increasing harmonics.



(a) OSPL over time plot of the DEP model and outdoor measurements



(b) Frequency spectra of the DEP model and outdoor measurements at 3 sec for a 0.1 s interval

Figure 16: Comparison of the DEP model with the performed flyover measurements

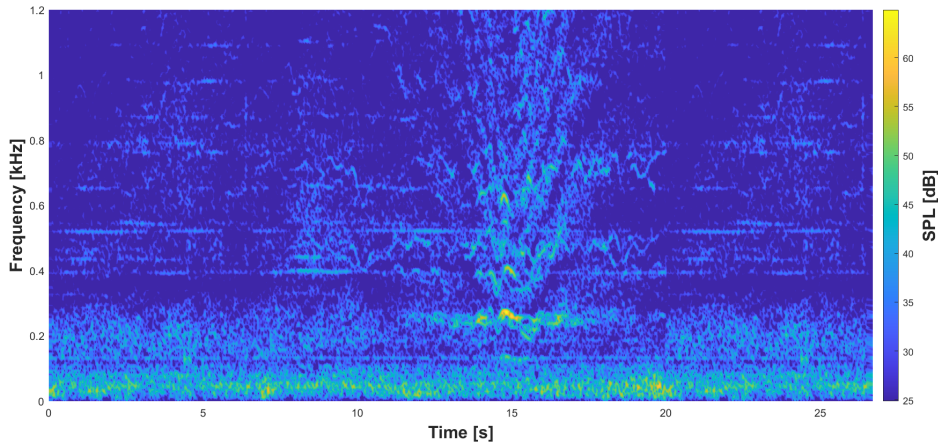


Figure 17: Spectrogram of the self performed flyover experiment

4 Results

The regional aircraft investigated in this research is developed by Maeve Aerospace. Their configuration is called Maeve-01, and has four wingspan-distributed propellers as shown in Figure 18. The required information regarding the aircraft configuration and its operating conditions was gathered from Maeve Aerospace's website [6], and is summarised in Table 4. Maeve-01 has four identical propellers of seven blades each and a diameter of 2.7 m. For this research, the assumption was made that each propeller is operated at the same speed and therefore produces the same thrust, i.e., spread frequency configurations will not be considered. The position of the propellers are illustrated in Figure 18. Unfortunately, Maeve-01's blade geometry is not available to the general public, and for that reason a different propeller was selected to perform the noise analysis with. The

chosen propeller was used by Elbers during her research on the Helix tool. A more detailed explanation on the propeller geometry can be found in Elbers [16].

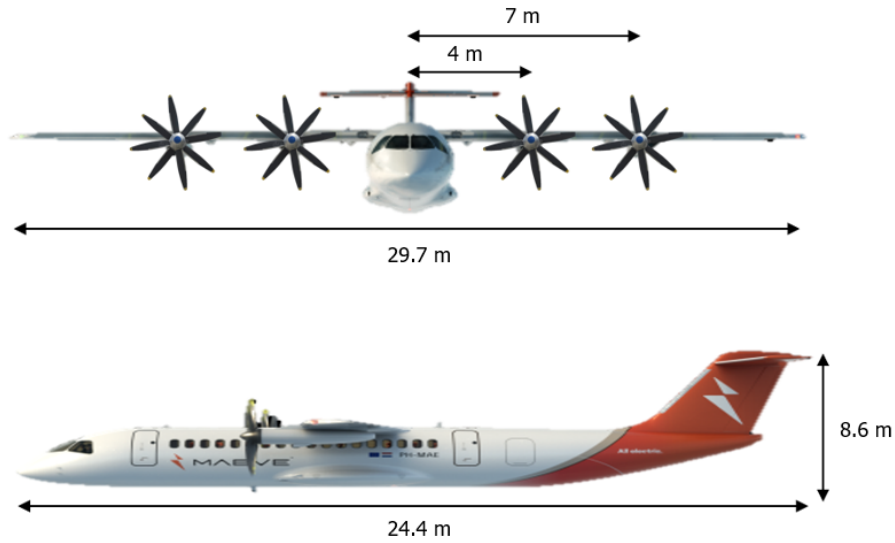


Figure 18: Front and side view from Maeve-01 [6]

Table 4: Operating conditions used for Maeve-01 [6]

Mach	Propeller RPM	Altitude [m]	Number of blades	Propeller diameter [m]	$\beta_{0.75}$ [deg]	J
0.35	1500	260	7	2.7	40	1.78

The results of a Maeve-01 flyover are presented in Figure 19 and Figure 20. Figure 19(a) presents the directivity plot and Figure 19(b) displays the same flyover in polar form. It can be seen that two directivity plots have been included in this analysis, i.e., one where the ground reflection is included and one without the contribution of the ground effect. It can be observed that the directivity plot created by only the direct waves of Maeve-01 has a maximum OSPL of 94 dB, which is located at an emission angle of 84 deg. When the reflected sound waves are included, the maximum OSPL increases to 98 dB, which can now be found at an emission angle of 86 deg. Furthermore, it can be seen that, besides an increase in the maximum OSPL, the shape of both directivity plots differs when the ground reflection is included. The directivity plot of only the direct waves shows symmetrical behaviour during the flyover, whereas two dips in OSPL values appear, at around 55 deg and 125 deg, when the ground reflection is included. These dips are a result of the waves being out of phase in these regions. It should be noted that for this analysis it was assumed that the observer was located right underneath the flight path at a height of 1.8 m.

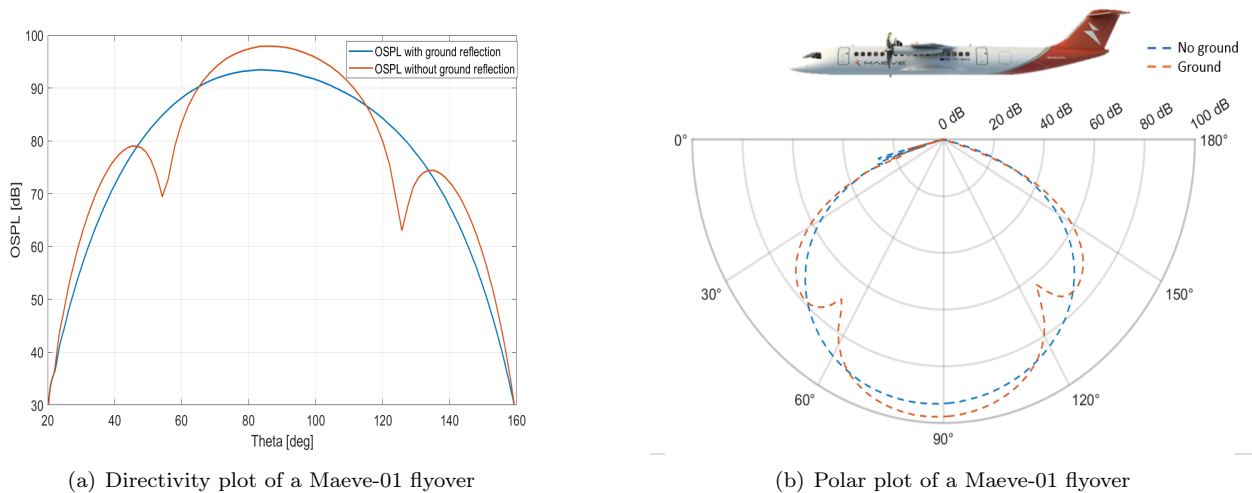


Figure 19: OSPL results of a Maeve-01 flyover

Besides the directivity of the aircraft, the spectrogram of the flyover, which presents the sound pressure level as a function of time and frequency, for the scenario without ground reflection is illustrated in Figure 20. In this figure it can be seen that the frequency composition of the signal depicting the aircraft’s flyover changes over time. Furthermore, it can also be observed that in the current version of the DEP model only the tonal noise components of the signal are considered, as noise is only produced at the BPF (equal to 175 Hz) and its harmonics. The BPF and the Doppler shifted frequency bounds are also presented in Figure 20 as a form of verification. It can be seen that from 0 to 15 seconds the aircraft is approaching the observer, resulting in a higher frequency, and that from 15 seconds onwards the aircraft has passed the observer, resulting in a lower frequency due to the Doppler shift. Finally, it can also be observed that the atmospheric absorption is present in the DEP model, since the higher frequency noise is filtered out for a large part.

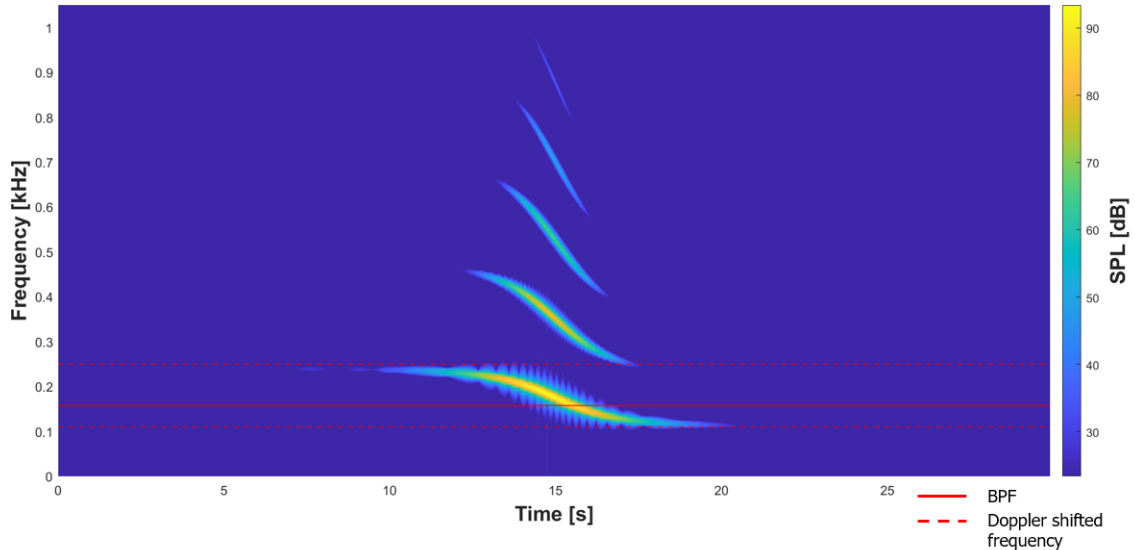


Figure 20: Spectrogram of a Maeve-01 flyover

5 Conclusion & recommendations

In this paper, a tonal noise prediction model of a DEP configuration has been introduced. The developed model expands on the Helix tool, which is an isolated propeller noise model developed at Delft University of Technology. It was found that the noise of multiple propellers could be superimposed at observers in the far field by making use of the retarded-time solution of the Ffowcs Williams and Hawkings (FWH) analogy to mimic a DEP configuration. In addition to the FWH analogy, spherical spreading is included as a gain and atmospheric absorption as a filter to incorporate the propagation effects into the model. Additionally, the ground reflection has also been included in the DEP model, as the reflections of the sound waves from the ground create additional paths, which result in an extra number of sound waves (equal to the number of propellers) reaching the observer. For these signals the same processing steps are performed, and subsequently they can all be summed when they reach the observer at the same time t .

The DEP model has been validated with the research performed by Guerin [9] and Rizzi [21], and with self-performed flyover experiments. During the comparison with literature data, it became apparent that the used propeller has a significant impact on the directivity pattern of a DEP aircraft (or a propeller in general). During the first comparison with Guerin’s data, the directivity plots predicted by the DEP model and by Guerin showed significant discrepancies between the shape of both graphs. The hypothesis was that these differences existed because of the differences in propeller geometry, as the DEP model used a propeller where the thickness noise was dominant, and Guerin used a propeller where the loading noise was dominant. It was observed that by altering the selected propeller to a propeller with a thinner blade geometry, better agreement was found between the directivity patterns produced by the DEP model and by Guerin. The same holds for the comparison between the heat maps produced by Rizzi and the DEP model. For the self-performed flyover experiments, it was found that the maximum OSPL predicted by the DEP model showed excellent agreement with the recorded data. However, for the low and high emission angles the DEP model underestimated the recorded OSPL. This was attributed to a combination of background noise, and the fact that broadband noise is dominant in these regions. All in all, the DEP model showed satisfactory agreement with the validation data. However, due to the limited literature data and flyover data available to validate the DEP model with, it is recommended to perform more

flyover experiments with an actual DEP configuration, to increase the confidence in the developed DEP model.

The regional aircraft investigated in this research is developed by Maeve Aerospace. Their configuration is called Maeve-01, which has four wingspan-distributed propellers of seven blades and a diameter of 2.7 m. Running the DEP model for this aircraft resulted in a maximum OSPL value of 94 dB at an altitude of 260 m, and 98 dB with the ground reflection included. What stands out is that the maximum OSPL is roughly 5 dB louder than the maximum OSPL found for Guerin’s configuration. This finding raises the question whether the difference in noise levels can be attributed to the fact that Maeve-01’s propellers rotate at a higher frequency, or that it has to do with the selected configuration (i.e., whether configurations with more but smaller propellers produce less noise)? This could be an interesting follow-up research project, which could potentially reduce Maeve-01’s noise levels before they start roaming the skies. This research could focus on aerodynamic properties, but also on the acoustic signatures of the aircraft by determining which design choices and operating conditions have the most impact on the noise levels.

As the findings of the performed research have been discussed, it is time to transition to a forward-looking perspective, offering recommendations that acknowledge the study’s limitations, but also pave the way for future research possibilities. For example, in this version of the DEP model, only the tonal noise contributions have been included. The first recommendation is therefore to develop a method that will incorporate the broadband noise of a DEP configuration in the model. From a brief search online it was concluded that no analytical model exists currently that predicts the broadband noise of a DEP configuration. For that reason, an experimental approach might be the more suitable technique to tackle this problem.

This research has shown that an equal relative blade position between propellers has the ability to affect noise patterns due to interference patterns. However, a potential research topic might be to analyse how these patterns change when a difference in initial blade positions amongst the propellers is introduced. This phenomenon is also known as clocking and is expected to have a significant effect on the interference patterns. Clocking might also enable the possibility to steer the noise away from noise sensitive areas, and direct it towards regions where the noise can do less harm.

For the final recommendation, the DEP model could be used to conduct psychological assessments, thereby gauging the annoyance levels associated with distributed electric propulsion aircraft. This research will be essential for the development of DEP aircraft, as understanding the human factors involved in the perception of aircraft noise is paramount. By incorporating psychological assessments into the evaluation process, we can derive valuable insights that contribute not only to the refinement of DEP technologies but also to the establishment of more user-friendly and socially acceptable air transport solutions. This integration of human-centric perspectives will undoubtedly play a pivotal role in shaping the future landscape of sustainable aviation.

Acknowledgements

This work was supported by NLR and Delft University of Technology, whose collaborative contributions significantly enriched the scope of this research. The author expresses sincere gratitude to Mirjam Snellen, Wouter de Haan, and Sander Heblj for their invaluable guidance throughout the project. Special appreciation extends to Bieke von den Hoff for engaging in numerous insightful discussions that stimulated critical thinking. Lastly, heartfelt thanks are extended to Fernanda do Nascimento Monteiro, Alessandro Mancinelli, and Anique Altena for their assistance during the validation experiments.

References

- [1] T. Sinnige. Aerodynamic and aeroacoustic interaction effects for tip-mounted propeller. 09 2018.
- [2] L. Veldhuis. Propeller wing aerodynamic interference, 2005.
- [3] IATA. Air passenger numbers to recover in 2024. <https://www.iata.org/en/pressroom/2022-releases/2022-03-01-01/>, 2022. Online; accessed 9 May 2023.
- [4] L. Gipson. Advanced air vehicle program (aavp). <https://www.nasa.gov/aeroresearch/programs/aavp/description/>, 2020. Online; accessed 9 May 2023.
- [5] D. Kim, T. Perry, and J. Ansell. A review of distributed electric propulsion concepts for air vehicle technology, 2018.
- [6] Maeve Aerospace bv. Maeve Aerospace’s concept for distributed electric propulsion. <https://maeve.aero/home>, 2023. Online; accessed 7 March 2023.

- [7] NASA. NASA's X-57 concept for distributed electric propulsion. <https://www.nasa.gov/specials/X57/>, 2017. Online; accessed 7 March 2023.
- [8] M. Haddaoui. Development of a propeller noise source model, 2019.
- [9] S. Guerin and D. Tormen. A contribution to the investigation of acoustic interferences in aircraft distributed propulsion, 2023.
- [10] M. Drela and H. Youngren. Xfoil 6.94 user guide, 2001.
- [11] X. Geng, T. Hu, P. Liu, T. Sinnige, and G. Eitelberg. Analysis of thrust-scaled acoustic emissions of aircraft propellers and their dependence on propulsive efficiency, 2021.
- [12] M. Drela and H. Youngren. Xrotor user guide. http://web.mit.edu/drela/Public/web/xrotor/xrotor_doc.txt, 2003. Online; accessed 30 May 2023.
- [13] D. Hanson. Helicoidal surface theory for harmonic noise of propellers in the far field, 1980.
- [14] G.L. Stefko and R.J. Jeracki. Wind tunnel results of advanced high speed propellers at takeoff, climb, and landing mach numbers, 1985.
- [15] P. Block. Experimental study of the effects of installation on single and counter-rotation propeller noise, 1986.
- [16] N. Elbers. Assessment of an aircraft propeller noise model by verification & experimental validation, 2021.
- [17] O. Gur and A. Rosen. Comparison between blade-element models of propellers, 2008.
- [18] Damiano Casalino. Analytical and numerical methods in vortex-body aeroacoustics, 2002.
- [19] M. Arntzen. Aircraft noise calculation and synthesis in a non-standard atmosphere, 2014.
- [20] D.T. Blackstock. Fundamentals of physical acoustics, 2000.
- [21] K.A. Pascioni, S.A. Rizzi, and N.H. Schiller. Noise reduction potential of phase control for distributed propulsion vehicles, 2019.
- [22] IMOTHEP. Investigation and maturation of technologies for hybrid electric propulsion. www.imothep-project.eu, 2023.
- [23] P. Chiariotti, M. Martarelli, and P. Castellini. Acoustic beamforming for noise source localization - reviews, methodology and applications, 2019.
- [24] D. Schoorl. A comparison of 3-dimensional acoustic localization methods based on global optimization and neural networks, 2021.

Appendices

A Heat maps verification

To verify whether the differences between the heat maps produced by Rizzi and the DEP model could be explained by the different propellers used in both cases, a heat map is created with the DEP model making use of a thinner propeller. Even though there are still differences between the heat maps, it can be seen that the noise levels behind the aircraft are indeed higher than in front of the aircraft, and that the general patterns become more similar. To be absolutely sure that the difference in propeller is the main reason for the difference in heat maps, the DEP model should be run in the future with the same propeller as Rizzi, but for now the hypothesis stands that with a more similar propeller both heat maps will become even more alike.

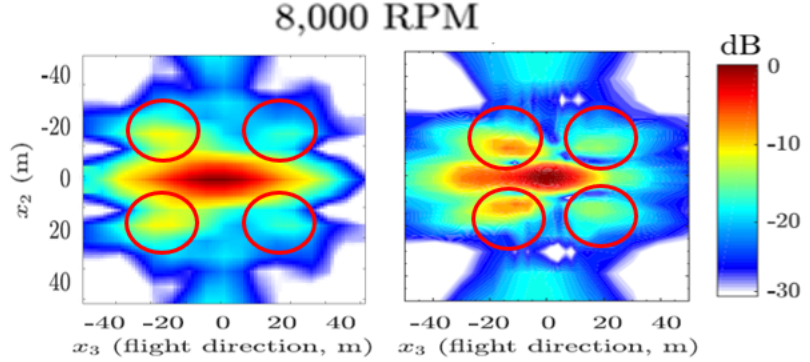


Figure 21: Example heat map when the loading noise is dominant produced by the DEP model

B Beamforming

In this appendix the results of beamforming of the real-life flyover experiments will be presented. It was decided to perform beamforming as a form of verification to be certain that the measured sound came from the drone. Beamforming relies on analysing input signals from multiple microphones positioned at slightly different positions. By combining these input signals, it is possible to extract information about the location and intensity of the source [23]. Figure 22 presents the microphone array setup used during the experiments.

It was decided to perform conventional frequency domain beamforming, which is a popular method to obtain beamforming plots for acoustic experiments. The algorithm considers the Fourier transforms of the measured pressures from the N microphones in the array as a vector $p(f) \in \mathbb{C}^{N \times 1}$, as described in Equation 12. The measured signal can be denoted as $s_j g_j$. This is the product of two factors: s_j , which represents the strength of the source, and $g_j \in \mathbb{C}^{N \times 1}$, which stands for the steering factor associated with a potential location. The steering vector g_j comprises N components, representing the modelled pressure amplitudes at microphone locations for a sound source of unit strength. The g_j that is used is determined by Equation 13, where $\tau = r/c$. The parameter r is defined by Equation 14, where x_n and y_n represent the coordinates of the different microphones, x_j and y_j stand for the coordinates of the scan grid, and h depicts the distance from the grid plane to the microphone plane.

$$p(f) = \begin{pmatrix} p_1(f) \\ \dots \\ p_N(f) \end{pmatrix} \quad (12) \quad g_j = \frac{e^{-2i\pi f \tau}}{r} \quad (13) \quad r = \sqrt{(x_n - x_j)^2 + (y_n - y_j)^2 + h^2} \quad (14)$$

The autopower of a source, denoted as A , at a specific potential source location represented by grid point ξ_j can be computed with Equation 15. In this equation, an asterisk stands for the complex conjugate transpose and C represents the cross-spectral matrix (CSM) of the experimentally obtained pressures, which has a size of $N \times N$. By evaluating the acoustic source strength at each grid point, it becomes possible to generate a map illustrating the acoustic landscape at a fixed plane above the microphone array. Analysing the beamform outputs at all grid points reveals that the grid point exhibiting the highest beamform output is likely to be the location of an acoustic source. A more elaborate explanation on beamforming can be found in School [24].

$$A(\xi_j) = \frac{g_j^* \langle pp^* \rangle g_j}{\|g_j\|^4} = \frac{g_j^* C g_j}{\|g_j\|^4} \quad (15)$$

At around 15 s, the drone passes directly in front of the microphone array during the flyover measurement. A time snap of 0.1 s is chosen for beamforming and starts at 14.95 s. The result plot of the beamforming procedure is presented in Figure 23. The displayed beamform plot is the result of incoherent averaging for the frequencies from 2 kHz to 5 kHz. It can be seen that the drone is flying at an altitude of 15 m and has already passed the middle of the microphone array as it is located roughly 4 m to the right.



Figure 22: The array test setup during the experiments

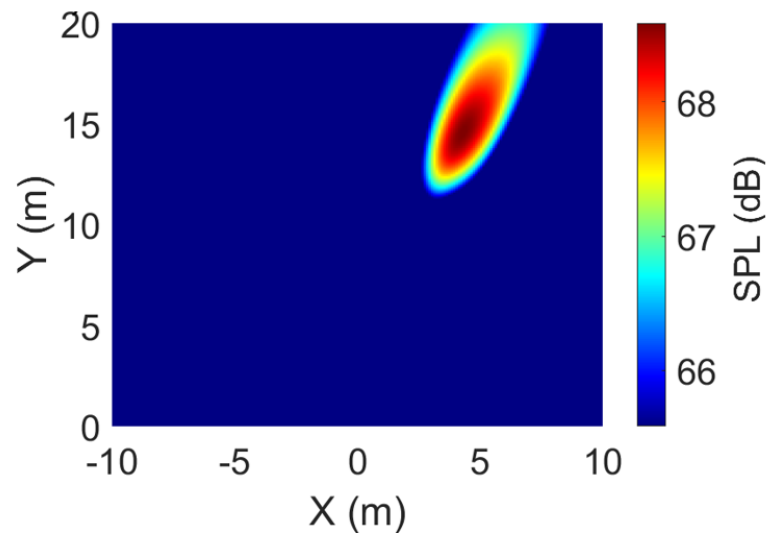


Figure 23: Beamform plot for a frequency range of 2 - 5 kHz

C Spectrum comparison

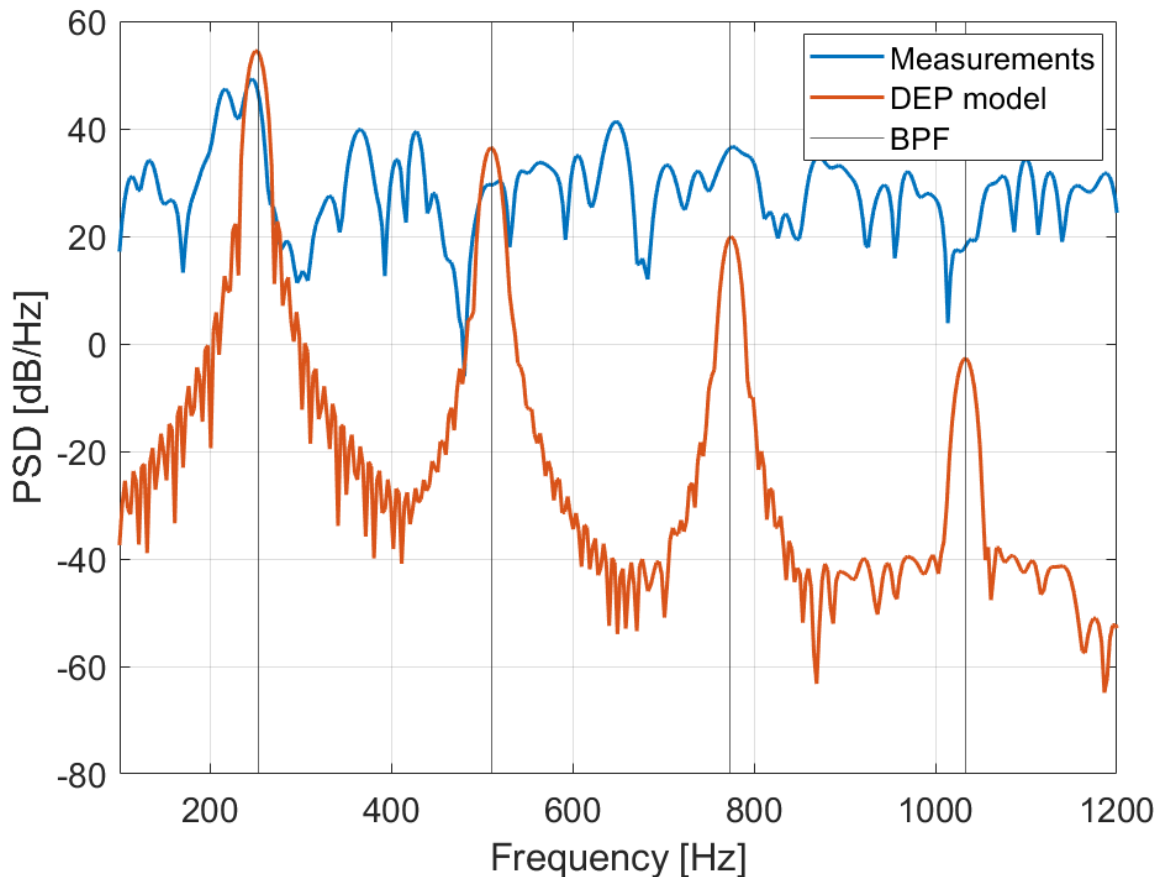


Figure 24: Frequency spectra of the DEP model and outdoor measurements at 3.8 sec for a 0.1 s interval

II

Literature Study previously graded under AE4020

Literature Study

The development of a
DEP noise model
C. Bononi Bello

Delft University of Technology

Literature Study

The development of a distributed electric propulsion (DEP) noise model

by

C. Bononi Bello - 4667530

on

Monday 4th December, 2023

to obtain the degree of Master of Science
at the Delft University of Technology,

Project duration: February 1, 2023 – TBD
Supervisors: M. Snellen, TU Delft
S. Heblj, NLR
W. de Haan NLR

Nomenclature

Abbreviations	
BPF	Blade passage frequency
CFD	Computational fluid dynamics
DEP	Distributed electric propulsion
DFT	Discrete Fourier transform
DP	Distributed propulsion
DPS	Digital processing steps
FWH	Ffowcs Williams and Hawkings
HST	Helicoidal Surface Theory
NLR	Dutch Aerospace Centre
OASPL	Overall A-weighted sound pressure level
OSPL	Overall sound pressure level
PBL	Pressure band level
PSD	Power spectral density
RMS	Root mean square
RPM	Rotations per minute
SEL	Sound exposure level
TUD	Delft University of Technology
UAV	Unmanned aerial vehicle
VCNS	Virtual Community Noise Simulator
VDL	Variable delay line

Symbols		
α	Angle of attack	$^{\circ}$
β	Blade pitch angle	$^{\circ}$
η	Efficiency	–
γ	Specific heat	–
∞	Free stream	–
Λ	Blade sweep	$^{\circ}$
λ	Wave length	m
μ	Dynamic viscosity	Pa · s
Ω	Rotational speed	rad/s
ϕ	Inflow angle	$^{\circ}$
Ψ_D	Drag distribution function	–
Ψ_L	Lift distribution function	–
Ψ_V	Thickness distribution function	–
ρ	Air density	kg/m ³

σ_b	Blade solidity	–
θ	Radiation angle	$^{\circ}$
a	Attenuation factor	–
B	number of blades	–
c	Blade chord length	m
c	Speed of sound	m/s
C_m	Moment coefficient	–
C_P	Power coefficient	–
C_T	Thrust coefficient	–
D	Drag	N
f	frequency	Hz
J	Advance ratio	–
k	Wave number	–
L	Lift	N
L_A	OASPL	dB
M	Mach number	–
m	Number of harmonics	–
n	Angular speed term	rev/s
N_b	Number of blades	–
N_p	Number of propellers	–
P	Power	W
$P(f)$	Power spectral density	Pa ² /Hz
$p(t)$	pressure time signal	Pa
p_e	Effective pressure	Pa
P_{mb}	Fourier coefficients of pressure time signal	–
Q	Torque	N
R	Propeller radius	m
R	Specific gas constant	m ² /(s ² K)
r	Distance between observer and source	m
T	Thrust	N
T	Time period	s
t	time	s
t_b	Maximum thickness to chord ratio	–
T_{air}	Ambient air temperature	K
V	Velocity	m/s
y	Altitude	m
z	Radial position of a blade element as a fraction of the radius	–

Contents

Nomenclature	i	5 Theory on auralization process	43
1 Problem Breakdown	31	5.1 The concept of auralization	43
2 Research questions	33	5.2 Atmospheric propagation.	44
3 Theory on isolated propeller aerodynamics	34	5.3 Signal processing for auralization	45
3.1 Propeller geometry	34	6 State-of-the-art	46
3.2 Fundamentals of propeller propulsion	35	6.1 Isolated propeller model	46
3.3 Propeller performance coefficients	36	6.2 DEP model	54
4 Theory on isolated propeller acoustics	37	7 Research plan and timeline	59
4.1 Basics of acoustics	37	8 Conclusion	60
4.2 Isolated propeller noise sources	39	References	62

Problem Breakdown

From aviation pioneers in the early 1900s to the British-French supersonic Concorde aircraft, it can be said that the aviation industry experienced a spectacular development in the 20th century. It all started when one of the Wright brothers, Orville Wright, took off in 1903 with their aircraft, known as the Wright Flyer III. This aircraft relied on propellers to produce the thrust necessary for the historical moment of the first ever controlled, powered and heavier-than-air flight. Their breakthrough resulted in the propeller being the subject of many research programs worldwide, which led to numerous successful propeller powered aircraft that showed impressive propulsive efficiencies for subsonic velocities [1].

It was only towards the end of World War II that a radically different propulsion system was introduced. This new piece of technology we now know as the jet engine. The invention of the jet engine and its derivatives (the turbofan and turboshaft), resolved some of the drawbacks experienced when using propeller driven aircraft, such as the limited service ceiling and flight velocity. Even though the jet engine came with a lot of benefits, it is important to note that the jet engine was not superior in every aspect, as it for instance had and still has a lower efficiency than a propeller driven aircraft [2]. Nevertheless, the introduction of the jet engine resulted in a stagnation in propeller research during the mid 50s to the mid 70s. During this time period fuel prices were low, and for that reason the lower propulsive efficiencies of the jet engine did not matter too much. A turning point was the 1973 oil crisis, which resulted in an imminent need for more fuel-efficient aircraft. This is when NASA started to research the possibilities of high-speed propeller passenger aircraft. The research resulted in various studies indicating that at high cruise speeds, such as $M = 0.8$, an advanced propeller driven aircraft would have a significant performance advantage over a similar turbofan aircraft [3]. One can think of fuel savings and reduced life cycle costs as examples. This concept was extensively researched, but due to the high Mach numbers the aircraft designers were faced with serious structural and aerodynamic problems, such as fatigue and shock wave formation over the wing. Even though solutions for these problems would definitely have been found over time, the research on the advanced turbofan concept was stopped, due to a drop in oil prices [1, 2].

Consequently, the past couple of decades turboprops were mostly disregarded by commercial carriers, which is one of the main reasons why nowadays civil aviation mostly relies on turbofan engines. Turboprops were found to be noisy and old-fashioned. However, with the ever-increasing trend of air travel from before the pandemic expected to return [4], the world's awareness of the environmental related issues linked to aviation have also increased. The need for environmentally-friendly solutions in the aviation sector has become one of the global technological challenges that have emerged in the last couple of decades. The Advanced Air Vehicles Program at NASA has taken note of these challenges and launched several initiatives to tackle them [5]. One of its key projects involves investigating subsonic aircraft designs that can significantly decrease energy consumption and emissions related to large passenger planes. With these issues becoming increasingly important, it is not surprising that the propeller, with its superior efficiency, has sparked the interest again of the aviation sector. Among the various concepts being explored, one particular propeller configuration stood out as promising: the distributed electric propulsion (DEP) configuration. This concept showed a lot of potential, and is therefore currently the subject of numerous research projects studied by various academic, government and industry bodies [6].

To introduce the concept of DEP, it is first necessary to understand a more common concept called distributed propulsion (DP) more broadly. In a DP system, the thrust of an aircraft is generated by an array of propulsive devices distributed along the wing span, as opposed to a single centralised engine. While there is no formal definition of a DP system yet, it generally refers to a propulsion setup that enhances the overall efficiency, capabilities, or performance of an aircraft by spreading the thrust output across multiple propulsors [6]. In addition to this, DEP systems use electrically driven propulsors that are connected to energy sources or power generating devices through electrical means. It is good to know that power sources for said system are not limited to a specific type and can include any combination of devices that generate electrical power, such as electric generators or fuel cells, as well as energy storage devices like batteries or capacitors.

As mentioned before, the DEP concept has gained significant popularity in recent times. However, due to the limited specific energy density of existing hardware, the adoption of this technology has mainly been observed

in small aircraft applications up until now. Nevertheless, due to the persistent interest in improving efficiency, reducing operating costs, and promoting sustainability in larger commercial aircraft, several organisations are now also investing in DEP aircraft systems capable of carrying more passengers and cargo. In [Figure 6.8](#) example concepts of both cases are shown. In [Figure 1.1\(a\)](#), NASA's X-57 Maxwell aircraft can be seen. This is NASA's experimental aircraft, intended to investigate the DEP concept. The aircraft is a conventional fixed-wing configuration that utilises twelve small electrically driven propellers mounted to the leading edge of the wing and two larger ones placed at the wing-tips. All the required power is provided exclusively by a set of lithium-ion battery packs. On February 3, 2023 NASA released an update on the progress of the development of the X-57 Maxwell, stating that the testing of its cruise motor controllers was a success, which puts the aircraft a major step closer to performing its first test flight [7]. In [Figure 1.1\(b\)](#) Maeve Aerospace's (a Dutch startup) concept for electric flying is depicted. They are aiming to develop a 44-seat fully-electric regional aircraft, known as Maeve-01, and are aiming to have their aircraft in the skies by 2028 [8].



((a)) DEP concept by NASA: X-57 Maxwell [7]



((b)) All electric aircraft concept by Maeve Aerospace [8]

Figure 1.1: Examples of distributed propulsion aircraft

While DEP configurations have the potential to revolutionise aircraft designs and performance, there are still several technological and operational challenges that must be addressed before the production of these vehicles can start. One of these research areas that for example still needs to be explored is the noise pollution caused by a DEP configuration and how this sound is experienced by people. Normally aircraft noise pollution is measured using a microphone array to evaluate the impact an aircraft flyover has on the community. However, for new aircraft concepts this is not possible. Therefore, a different approach needs to be selected to assess the noise pollution of a DEP system. An example of a suitable approach is the concept of auralization, which is the procedure of modelling a noise source and subsequently transforming the created noise sample into an audible result. Due to the pressing need for a noise sample of a DEP configuration, the aim of this thesis will be to develop a noise model of such an aircraft in order to assess the annoyance experienced by people caused by such an aircraft. If the project is a success, the noise of a DEP concept can be evaluated and compared to a conventional aircraft, and provided the annoyance experienced lays within an acceptable range, the production of such an aircraft will be one step closer to reality.

For this project, the Delft University of Technology (TUD) and the Netherlands Aerospace Centre (NLR) will combine their forces to work on the auralization of a DEP aircraft. The ideal result of this project will be to create a DEP noise model, which potentially can be implemented in NLR's Virtual Community Noise Simulator (VCNS) tool. This tool makes it possible to experience an aircraft flyover in a virtual-reality environment utilising 360 degrees video and 3D audio samples. It is a perfect way to analyse new types of aircraft and new procedures before implementing them. Consequently, the VCNS enables policy makers to experience the effects of their intended policy changes, and additionally helps communicating the consequences to the affected community.

This report will function as the literature study of this project, and has the objective to provide the reader with the underlying principles to create a DEP noise model in the future. Consequently, this report will form the basis of the master thesis that is being carried out. The report is structured as follows. In [Chapter 2](#) the research objective and resulting research questions will be presented. This will be followed by three short chapters on pure theory about propeller aerodynamics, propeller noise and auralization in [Chapter 3](#), [Chapter 4](#) and [Chapter 5](#) respectively. [Chapter 6](#) summarises the research on propeller noise modelling that already exists today, and ultimately proposes a methodology to tackle the problem at hand. This will be followed by proposing a detailed research plan and according time line in [Chapter 7](#). Finally, the report is concluded in [Chapter 8](#).

Research questions

Before one can say if a research project has been a success, it is necessary to first define the research objective. This will serve as the overarching goal of the thesis and provides a basis for formulating a research question that will guide the study. The research objective for this thesis was largely provided by NLR and is defined as follows:

The research objective is to develop a realistic noise signal over time of a DEP aircraft flyover by expanding the isolated propeller model of either NLR or TUD, which ultimately can be integrated in the VCNS tool of NLR to help experience a flyover event of such an aircraft in its climbing phase while considering uniform inflow.

Before a DEP aircraft configuration can be implemented in the fleet of airlines, the noise pollution of such an aircraft concept compared to a conventional passenger aircraft needs to be evaluated. By developing a noise model of a DEP aircraft, this research aims at contributing to paving the way for the production of a DEP regional passenger aircraft in the future, which due to its superior efficiency over jet engines will most likely have a significant impact on the emissions of regional air travel [6]. Moreover, this research aims to provide insights into the potential benefits or drawbacks of using distributed propulsion in order to reduce the annoyance experienced by humans due to an aircraft flyover. The associated main research question in order to achieve the research objective is the following:

What is the influence of adding multiple propellers along the wingspan of a regional aircraft on the noise experienced by humans of an aircraft flyover, compared to a single propeller aircraft?

In order to address the main research question, it is necessary to formulate several sub-questions that are more specific and capture the essence of the complete research. These sub-questions will either be answered in the remainder of the literature study or they will be answered during the actual research.

The associated research sub-questions are the following:

1. **What are the primary noise sources associated with an isolated propeller?**
 - (a) Which aerodynamic parameters influence the noise produced by an isolated propeller?
 - (b) What type of noise does a propeller produce, and what is the dominant noise in forward flight?
 - (c) How can these noise sources be modelled and simulated using available acoustic prediction tools?
 - (d) What are the most appropriate noise metrics one can use to evaluate the noise generated by a DEP?
2. **How can the noise generated by individual propellers be modelled in a DEP configuration to create a realistic noise signature?**
 - (a) How are current DEP auralization models programmed, i.e., what type of noise do they include in their analysis/ which methods do they use?
 - (b) How will the sound produced by a DEP aircraft flyover be experienced by the community, i.e., is it true that a number of small propellers combined will create a much higher frequency noise, and therefore will die out more quickly?
 - (c) Which propagation effects are relevant to include when considering the noise impact of a DEP aircraft on an observer in the far-field?
3. **How can the accuracy of the noise model be verified and validated using experimental data and/or computational simulations?**
 - (a) Is there a representative aircraft that can be used to validate the model? It can either be in the form of wind tunnel data or measurements from an actual flyover.
 - (b) Which parameters have the most impact on the noise produced by a DEP configuration? This could for example be evaluated during a sensitivity analysis.

Theory on isolated propeller aerodynamics

This chapter will provide the reader with background on the aerodynamic performance of an isolated propeller. This will be done by first describing the most important design parameters of a propeller in [Section 3.1](#). Secondly, the fundamentals of propeller propulsion will be discussed in [Section 3.2](#). To conclude this section, the propeller performance coefficients will be presented in [Section 3.3](#). It is important to note that these concepts are not only essential in understanding the upstream and downstream effects of an isolated propeller, but considering the fact that in a distributed propulsion system the propellers operate in very close proximity to each other, they are fundamental in the research on the performance of a distributed propulsion system.

3.1. Propeller geometry

Aerodynamic research for a formula-1 car or a new aircraft configuration has always been an area of high investment. The reason for this is that changing different design parameters can have a significant impact on the performance of the vehicle. The same reasoning holds when designing a propeller. For this reason, the most important design parameters will be described in this section.

The design of a propeller can be described by top-level and planform design parameters, and the design process normally starts by selecting the top-level design parameters. These parameters can be found in [Figure 3.1\(a\)](#), and consist of the diameter (D), the hub ratio (D_{hub}/D), the number of blades (N_B) and the blade solidity (σ_B), which stands for the blade area divided by the disk area [9]. The combination of these four design parameters defines important performance characteristics of the propeller, such as the disk loading (thrust per unit disk area) and the blade loading (thrust per unit blade span). These parameters are sufficient for a very basic description of the propeller, enabling preliminary performance predictions. However, they do not describe the shape of the propeller blades. In order to deal with this the planform design parameters are introduced.

The planform design parameters of a propeller are visually presented in [Figure 3.1\(b\)](#). It is important to know that the propeller blade planform is described in the same way as a wing, and similarly also consists of airfoils. First of all, the chord (c) represents the width of the blades. Secondly, the pitch (β) describes the twist of the blades with respect to the rotational plane. The pitch consists of a twist distribution (θ) and a collective pitch setting (β_{ref}). Next, there is the sweep (λ), which represents an angular rotation of the blade section. Additionally, there is one more planform design parameter which is not visible in the figure. This parameter is called the lean angle (γ), which represents the out of plane angle of the blade. This is comparable to the dihedral of a wing [9].

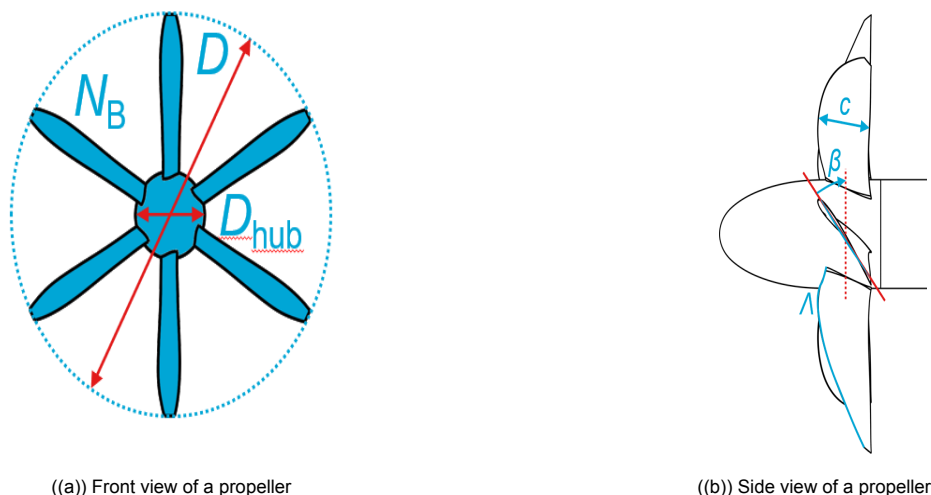


Figure 3.1: The top level and planform parameters of a propeller [9]

The optimal planform design is a complex compromise between conflicting requirements and depends on the design objective and design requirements of the propeller. Once the blade shape is defined, the propeller can still be operated in different ways. To achieve this the following operational parameters are introduced: the rotational speed (Ω) and the blade pitch setting (β_{ref}). These parameters are used to change the propeller performance in a given flight condition. There are two types of propellers: the fixed pitch propeller and the variable pitch propellers. For fixed pitch propellers, the blade pitch is fixed throughout the flight and therefore the propeller loading is modified by changing the rotational speed. For variable pitch propellers, the pitch setting can be varied to change the blade loading. In that case the rotational speed is usually fixed at a value that gives optimal efficiency of the motor that is driving the propeller [9].

3.2. Fundamentals of propeller propulsion

Propellers are propelling devices that accelerate the airflow in order to produce thrust. A simplification of the thrust generating principle can be explained through the actuator disk theory. The actuator disk theory is in fact a mathematical model that describes the performance of a propeller or a fan. According to the actuator disk theory a propeller can be modelled as a thin circular disk that generates thrust by accelerating a stream of air [2]. It should be noted that the original theory, as formulated by Rankine and Froude, assumes the flow of air over the propeller to be axisymmetric, inviscid and incompressible. A visual representation of the actuator disk theory can be found in [Figure 3.2](#). Here the propeller is approximated by an infinitely thin actuator disk and a stream tube defines the flow domain of the moving air in the upstream and downstream direction of the disk. The basic premise of this theory is that the thrust (T) generated by the propeller is computed by implementing the momentum theory to the flow in the stream tube. This results in the relation presented in [Equation 3.1](#), where the thrust can be calculated by multiplying the mass flow rate of air (\dot{m}) through the disk by the velocity increment ($V_3 - V_\infty$) as it passes through the stream tube. Combining this theory with [Equation 3.2](#), also explains the significant propulsive efficiency (η) gain from turboprops over turbofan engines. The increased efficiency directly follows from the simple thrust momentum balance which states that the efficiency decreases as the axial velocity increment (ΔV) through the propulsor increases, and as turboprops induce smaller velocity increments to a larger mass flow than turbofans, the efficiency of a turboprop is higher than that of a turbofan [2].

$$T = \dot{m}(V_3 - V_\infty) \quad (3.1) \quad \eta = \frac{1}{1 + \frac{\Delta V}{V_\infty}} \quad (3.2)$$

As mentioned before it is important to realise that while the actuator disk theory provides a useful framework for understanding the performance of propellers, it is a simplification of the complex physics involved in real-world flows. In practice, the actual performance of propellers can be significantly influenced by factors such as viscosity and turbulence, which are not accounted for in the actuator disk theory. Therefore, to shed some light on the shortcomings of the actuator disk theory the propeller blade loading, which is used in blade element models that predict the propeller performance, will be discussed in [Subsection 6.1.1](#).

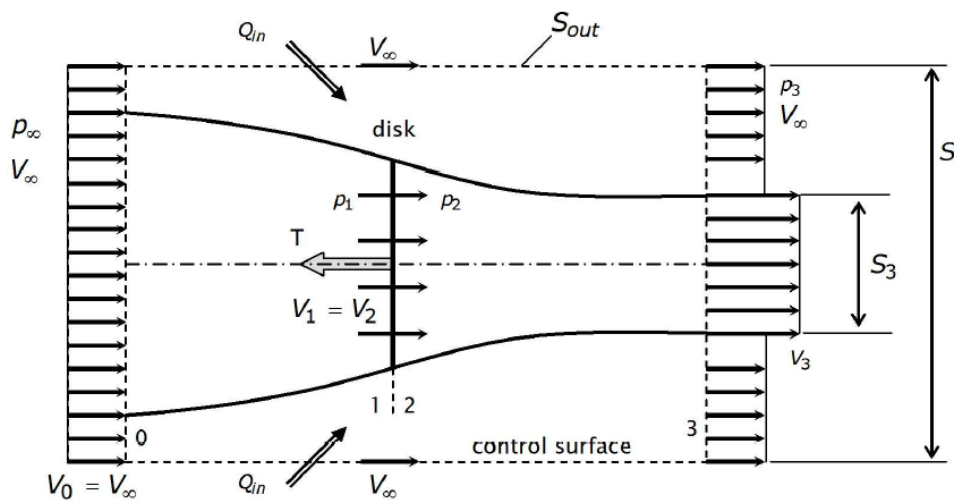


Figure 3.2: Actuator disk model with control volume for the application of the momentum equation [10]

3.3. Propeller performance coefficients

The propeller performance can be described by three key performance indicators: thrust (T), shaft power (P) and propeller efficiency (η). In order to compare the performance of propellers of different scales and operating conditions the use of dimensional quantities, like thrust and shaft power are not useful. Instead, making these quantities non-dimensional is required to describe the performance independently of the scale. The following non-dimensional parameters are often used to express the propeller performance: the thrust coefficient (C_T), the power coefficient (C_P) (or the torque coefficient C_Q) and the propeller efficiency (η) [1].

$$C_T = \frac{T}{\rho_{\infty} n^2 D^4} \quad (3.3) \quad C_P = \frac{P}{\rho_{\infty} n^3 D^5} (= 2\pi C_Q) \quad (3.4) \quad \eta = \frac{TV_{\infty}}{P} \quad (3.5)$$

Another parameter related to the performance of a propeller is the advance ratio (J). This non-dimensional number is the ratio between the axial and rotational velocity components, and can also be seen as the distance travelled per one revolution over the diameter. The advance ratio can be computed with Equation 3.6. This relation tells us that for small values of the advance ratio, the rotational speed is dominant over the forward direction. On the contrary, for high values the forward motion overshadows the rotational motion. Furthermore, now with the advance ratio known the efficiency equation can be rewritten to Equation 3.7.

$$J = \frac{V_{\infty}}{nD} \quad (3.6) \quad \eta = J \frac{C_T}{C_P} \quad (3.7)$$

In order to describe the propeller performance, it is essential to know how the key scaling parameters vary as a function of the propeller operating conditions. An example of a propeller performance diagram for a fixed pitch setting can be found in Figure 3.3. As shown in Figure 3.3, the thrust and power coefficients increase with a decreasing advance ratio. This can be explained by considering the definition of the advance ratio: the advance ratio is equivalent to the ratio of axial to tangential velocity. Equation 6.1 shows that the inflow angle to the blade section (ϕ), scales with the same ratio. Consequently, when the advance ratio decreases ϕ will decrease and since the local angle of attack at the blade sections is defined as the difference between the local pitch and inflow angle, the local angle of attack will increase with a decreasing advance ratio. As a result, the thrust and power coefficients will increase with a decreasing advance ratio. Additionally, it can be seen that the efficiency curve has a distinct shape with a maximum at a single advance ratio, usually for modern full-scale props this is in the order of 85% and 90% [9].

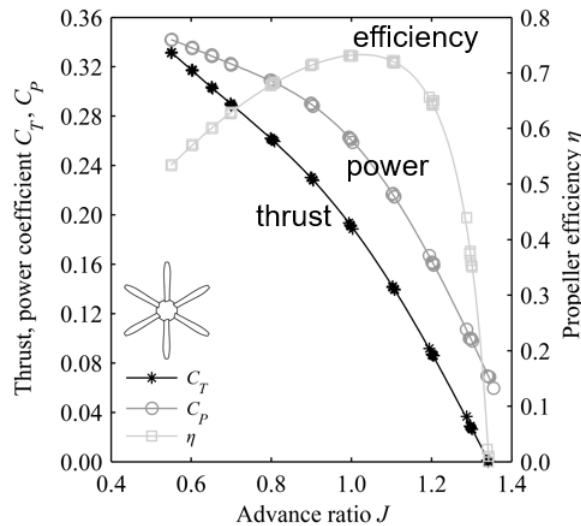


Figure 3.3: Propeller performance diagram: thrust and power coefficient and efficiency as a function of advance ratio [11]

Theory on isolated propeller acoustics

As mentioned in [Chapter 1](#), air transport has grown significantly in the past century. This growth can mainly be attributed to the combination of technical innovation, and the willingness of consumers to explore the world. The boost in innovation made it possible for the general public to travel around the globe, and consequently air travel contributed towards global economic development. The sky was the limit for the aviation industry, but in the last 10 years this romanticised view has faded away and turned into a more critical perspective, which focuses more on the current issues facing the aviation industry. One of these issues, and perhaps the most pressing one is the effect aviation has on the climate and the environment. An example of such an environmental issue is the noise pollution of an aircraft. Noise can be defined as sound that is unwanted by the observer and according to the WHO [12], the noise of a low-flying aircraft can affect human health and well-being in a variety of ways, such as disruption of sleep, community annoyance and could increase the risk of cardiovascular disease of people living in the vicinity of airports [13]. Even though the aircraft of today are the most silent ones in the history of flight, the negative environmental issues are a revelation that there is still a long way to go and that continuous research is needed to reduce aircraft noise at the source. One specific research area is the investigation of new aircraft concepts, such as the DEP configuration, and how these concepts would influence the annoyance experienced by humans compared to conventional aircraft. In order to analyse this, the first step is to get a good understanding on the basics of acoustics in general. This will be examined in [Section 4.1](#). Subsequently, in [Section 4.2](#) the noise produced by an isolated propeller will be discussed.

4.1. Basics of acoustics

In aerospace engineering, noise issues can be categorised into two types: interior noise, which refers to noise within the cabin, and exterior noise, which concerns the surrounding community. In this literature study the focus will be on exterior noise. This will be done by first treating the theory on sound waves in [Subsection 4.1.1](#). Followed by discussing how sound is quantified in [Subsection 4.1.2](#).

4.1.1. Theory on sound waves

Sound can be classified as a propagating pressure disturbance, which travels through the atmosphere in the form of an acoustic wave. While sound waves can also propagate through other mediums, this literature study will focus solely on sound propagating in the atmosphere due to an aircraft flyover. Acoustic waves are longitudinal waves, which means that the particles' displacement is in the same direction as the propagation of the sound wave. The propagation of a sound wave is visually depicted in [Figure 4.1](#). As the sound wave moves forward, it generates compression areas, which cause local increases in pressure, and expansion areas, which create local decreases in pressure. The sound source in [Figure 4.1](#) is producing noise at a single frequency. Assuming that the sound source is also a point source, the sound pressure at time t and distance r can be computed with [Equation 4.1](#).

$$p'(r, t) = \frac{A}{r} \cos(\omega(t - r/c)), \quad (4.1)$$

where ω represents the single radial frequency in [rad/s], A is the amplitude of the pressure disturbance at 1 meter from the source, and c stands for the speed of sound in the medium at hand in [m/s]. Furthermore, the notation of p' is chosen, because the pressure of sound is generally much smaller than the governing atmospheric pressure.

The wavelength (λ [m]), frequency (f [Hz]) or period (T [s]), and propagation speed (c [m/s]) are key properties of a sound wave, and for any sinusoidal sound wave these properties can be computed using [Equation 4.2](#).

$$\lambda = cT = \frac{c}{f} \quad (4.2) \quad c = \sqrt{\gamma_{air} R_{air} T_{air}} \quad (4.3)$$

This equation indicates that the wave length and frequency of a sound wave are inversely proportional to each other, which means that as the wavelength increases, the frequency decreases correspondingly, and vice versa.

In order to compute the propagation speed through a medium Equation 4.3 can be used. This equation tells us that the propagation speed depends on several factors, such as the specific heat ($\gamma [-]$), which is equal to 1.4 for air, the specific gas constant ($R [J/kg * K]$) is equal to 287, and the ambient air temperature ($T [K]$). Following this equation, the speed of sound at a temperature of 20° C (293 K) is computed to be approximately 343 m/s.

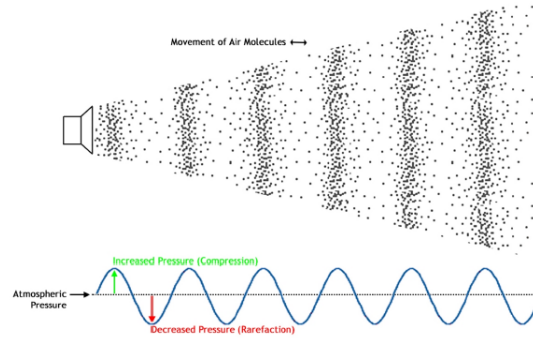


Figure 4.1: Visualisation of the motion of air molecules within an acoustic wave [14]

4.1.2. Quantification of sound

The strength of a sound wave can be quantified using a measure known as the *effective sound pressure* (p_e). This measure is generally expressed in units of pascals [Pa], and depicts the root-mean-square (RMS) value of the pressure fluctuations in the sound wave over a period of time. This value can be calculated using Equation 4.4, where T represents a sufficiently large integration time. Moreover, the energy content of a sound wave is generally measured and expressed in decibels [dB] as a metric known as the overall sound pressure level (OSPL), which can be calculated making use of the effective sound pressure. This relation can be found in Equation 4.5, where p_{e0} is the reference effective pressure which is equal to $2 \times 10^{-5} N/m^2$.

$$p_e = \left[\frac{1}{T} \int_0^T (p'(t))^2 dt \right]^{1/2} \quad (4.4) \quad OSPL = 10 \log \left(\frac{p_e^2}{p_{e0}^2} \right) \quad (4.5)$$

Aircraft sound can be categorised into two noise metrics: single event noise metrics and long-term noise metrics. Single event noise metrics can be used to describe the characteristics of a single noise event, such as an aircraft flyover. By using these single event metrics, researchers and policy makers can get a better understanding of the impact of a specific noise event. On the contrary, long-term noise metrics can be used to quantify the average noise exposure over a specified period of time. These metrics provide a more extensive picture of the overall noise pollution in a given area. Therefore, the long-term noise metrics are often used to develop noise control regulations aimed at protecting the general public in a specific region exposed to a lot of acoustic events, such as the inhabitants of a neighbouring town to an airport. Collectively, these two different noise metrics help to provide a complete picture of the impacts of aircraft noise on human health and the environment. For this reason, both metrics will be discussed more elaborately below. However, before this, a short intermezzo is added to this report on how the decibel values of multiple noise events can be added together.

Adding decibel values

The decibel scale is logarithmic in nature, and due to this, the addition of two decibel values may not be very intuitive, meaning that one cannot simply add noise levels arithmetically. For example, adding two noise events of 35 dB does not equal 70 dB. In order to illustrate how this process works several examples are added below.

$$\begin{aligned} 60 \text{ dB} + 60 \text{ dB} &= 10 \log_{10} \left(10^{\frac{60}{10}} + 10^{\frac{60}{10}} \right) \approx 63.0 \text{ dB} \\ 70 \text{ dB} + 60 \text{ dB} &= 10 \log_{10} \left(10^{\frac{70}{10}} + 10^{\frac{60}{10}} \right) \approx 70.4 \text{ dB} \\ 80 \text{ dB} + 60 \text{ dB} &= 10 \log_{10} \left(10^{\frac{80}{10}} + 10^{\frac{60}{10}} \right) \approx 80.0 \text{ dB} \end{aligned}$$

It becomes clear that the impact a less dominant sound signal has, quickly reduces when the difference in sound level between the signals is more than 10 dB. For example, when there are two sound sources, with one producing a sound level of 80 dB and the other producing a sound level of 60 dB, the effect the 60 dB signal on the overall sound level will be negligible.

Single event noise metrics

There are multiple metrics that can be used to describe the noise impact of a single noise event. Two of which are the $L_{A_{max}}$, which stands for the maximum overall A-weighted sound pressure level (OASPL), and the sound exposure level (SEL), which also accounts for the duration of a noise event. These two metrics can be calculated with Equation 4.6 and Equation 4.7 respectively.

$$L_{A_{max}} = \max(L_A(t)) \quad t_0 \leq t_1 \quad [dBA] \quad (4.6) \quad SEL = 10 \log_{10} \left(\int_{t_0}^{t_1} 10^{\frac{L_A(t)}{10}} dt \right) \quad t_0 \leq t_1 \quad [dBA] \quad (4.7)$$

It should be noted that the A subscript in these equations is used to denote the weighting that is applied to the sound level. As mentioned, $L_{A_{max}}$ represents the maximum OASPL value of a noise event, such as an aircraft flyover. To determine this value the entire time interval, i.e., from the beginning of the measurement (t_0 in [s]) to the end of the measurement (t_1 in [s]), should be analysed. On the other hand, to determine the SEL value the time interval should be selected such that at both t_0 and t_1 the sound level is 10 dBA lower than the $L_{A_{max}}$ value. This time interval is known as the '10 dBA down time'. Lower values are not necessary to include as was established that only the highest values of $L_A(t)$ contribute significantly to the end value [15]. To get a better understanding of these metrics the procedure to compute L_A will be discussed on the next page, and additionally an example of an aircraft flyover will be included at the end of this chapter.

Long-term noise metrics

An example of a long-term noise metric is the Day-Evening-Night average sound level, which is the standard metric adopted in Europe since 2002 [16]. The entire day is divided into three parts: day-time (07:00 - 19:00), evening (19:00 - 23:00) and night-time (23:00 - 07:00), and consequently a weight is assigned to aircraft noise events based on when they occur during the day. For example, for noise events that take place during the evening or at night a penalty is imposed. The purpose of including a penalty for the noise production during evening and night hours is to reduce the heightened annoyance perception that people experience during these quieter times. This metric is generally used to assess noise levels from airports, busy roads, and railway lines. The value for L_{DEN} can be determined using Equation 4.8, where L_{day} , $L_{evening}$ and L_{night} represent the A-weighted sound levels, respectively, calculated for all the corresponding periods during the year.

$$L_{DEN} = 10 \log_{10} \left(12 \cdot 10^{\frac{L_{day}}{10}} + 4 \cdot 10^{\frac{L_{evening}+5}{10}} + 8 \cdot 10^{\frac{L_{night}+10}{10}} \right) - 10 \log_{10}(24) \quad [dBA] \quad (4.8)$$

4.2. Isolated propeller noise sources

As we know, there are propellers in different shapes and sizes, as they are used in various applications. Despite these differences in geometry, the principles underlying the generation of noise are essentially the same. Propeller noise namely results from the interaction of a fluid with a rotating body. When examining propellers, there are two primary categories of noise that can be distinguished: harmonic noise, also known as tonal noise and broadband noise, also known as random noise [13, 17]. A more detailed representation of the propeller noise sources is provided in Figure 4.2. In the remainder of this section the reader will be introduced to the concepts behind harmonic noise and broadband noise, in Subsection 4.2.1 and Subsection 4.2.2 respectively.

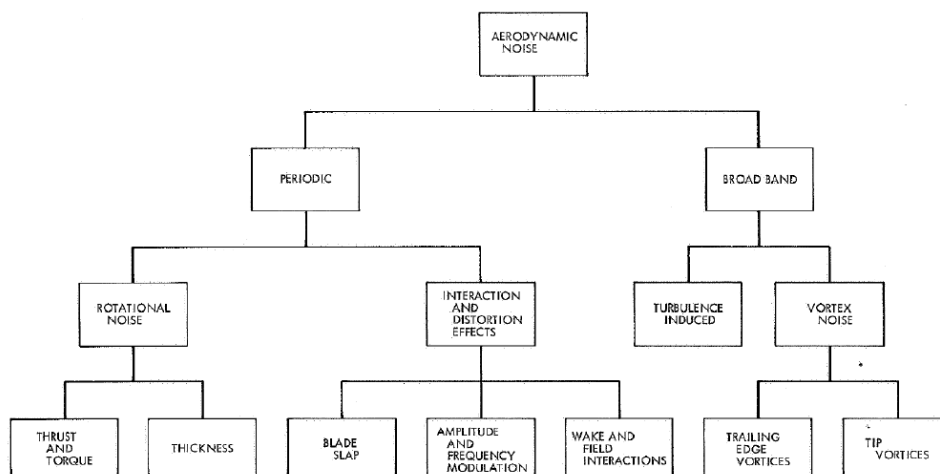


Figure 4.2: Overview of the aerodynamic noise sources [18]

4.2.1. Harmonic noise

Harmonic noise produced by a propeller is known as the periodic component. This means that it is assigned to noise sources that repeat themselves at a constant rate. In the case of an ideal propeller, the harmonic noise component repeats itself at the Blade Passage Frequency (BPF) [13]:

$$BPF = BN = B \frac{RPM}{60} \quad (4.9)$$

In this equation B represents the number of blades of the propeller, N stands for the constant rotational speed, which can be calculated with the revolutions per minute, also known as RPM. Usually the generated pulse of a propeller is not a pure sinusoid, which means that there exist many harmonics. These harmonics occur at an integer multiple of the BPF. An example of a harmonic noise signal in the time and frequency domain is provided in Figure 4.3. It can be seen that the signal in the time domain repeats itself after a period of $\frac{1}{BPF}$ and in the frequency domain the spectrum shows peaks at the BPF and multiples of the BPF.

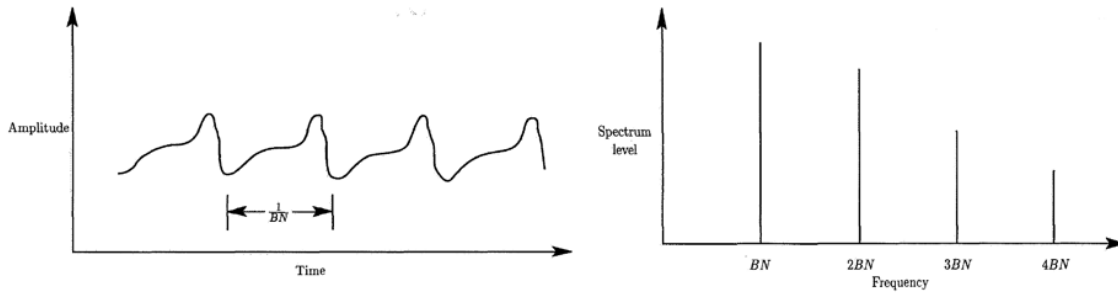


Figure 4.3: Characteristics of propeller harmonic noise [13]

It is important to note that the signals in Figure 4.3 are in fact the same signal, only represented in a different manner. It is in fact possible to go from the time to the frequency signal and the other way around. This is done by applying the Fourier transform, which transforms the signal from the time domain to the frequency domain. To become more familiar with analysing a signal in the frequency domain, the process will be discussed below.

Signal analysis in the frequency domain

When the signal of interest has a finite time interval, a Discrete Fourier transform (DFT) is required to transform the signal from the time domain to the frequency domain. This results in a spectrum that contains the amplitudes at the harmonic frequencies. Subsequently, the Power Spectral Density (PSD) in $[Pa^2/Hz]$ can be calculated with Equation 4.10, where $P(f)$ stands for the PSD, which is a measure of the signal's power in the frequency domain, $X(f)$ is the DFT of the propeller time signal, Δt represents the time interval and T is the duration of the signal.

$$P(f) = \frac{|X(f)|^2 (\Delta t)^2}{T} \quad (4.10)$$

With the PSD known, it is possible to compute pressure band levels (PBL) using a bandwidth analysis. The PBL represents the SPL within a specified frequency band and is defined according to Equation 4.11. After a bandwidth analysis the PBL for the consecutive bands are available. Typically the PBL values are denoted as $SPL(f_i, \theta)$, where f_i represents the centre frequency of band i , and θ stands for the angle at which the measurements were taken. The OSPL from the frequency domain can then be computed using Equation 4.12, which should achieve the same value as the OSPL in the time domain.

$$PBL(dB) = 10 \log_{10} \left(\frac{P(f) \Delta f}{p_{e0}^2} \right) \quad (4.11) \quad OSPL(\theta) = 10 \log_{10} \sum_{i=1}^n 10^{SPL(f_i, \theta)/10} \quad (4.12)$$

Next, the overall A-weighted sound pressure level can be calculated. The OASPL includes a weighting which accounts for the loudness of a noise event as perceived by the human ear. The function for the A-weighting is given in Equation 4.13. The OASPL can subsequently be determined using Equation 4.14.

$$\Delta L_A = -145.528 + 98.262 \log f - 19.509 (\log f)^2 + 0.975 (\log f)^3 \quad (4.13)$$

$$L_A = 10 \log_{10} \sum_i 10^{\frac{SPL(i) + \Delta L_A(i)}{10}} \quad (4.14)$$

After this short intermezzo, let us continue discussing the harmonic noise of a propeller. The noise sources that occur periodically, and therefore contribute to the harmonic noise of a propeller, are known as thickness noise and (un)steady-loading noise [13]. Thickness noise is the noise that arises due to the displacement of air induced by the rotating blades. This type of noise becomes more evident at high velocities and can be represented by a monopole source distribution [19]. A monopole is an elementary source, depicting a harmonic pulsating sphere [20]. Next, there exists steady-loading noise, which is caused by the pressure field of the blades as they produce lift and drag (or thrust and torque). The principle behind this is that as the blades move through the air, they create a fluctuating pressure field that generates noise. The steady-loading noise is most noticeable at low to moderate speeds. Similar to the thickness noise, the steady-loading noise can be represented as an elementary source, but in this case a dipole is required [19]. A dipole is actually two closely spaced monopoles in opposite phase. Besides the steady sources, there also exist unsteady sources. Unsteady-loading noise for example is created by inflow distortions that occur continuously. A typical example of this is when a propeller experiences non-axial inflow, such as the angle of attack. As a result of this constant inflow distortion fluctuations in blade loading occur that repeat after each revolution. It is important to mention that the impact of unsteady-loading noise on the overall noise level depends on the location of the loading disturbance on the blade during the rotation relative to the observer. As a result, the unsteady-loading noise can add or subtract from the steady-loading noise. Besides a monopole and a dipole there is another elementary source, called a quadrupole source, which consists of two dipole sources in opposite phase. This source becomes more dominant when non-linear effects arise, which happens when sonic or supersonic speeds are achieved, and shock waves form over the blade. Numerous researchers have investigated the importance of the quadrupole source term. H. Blackburn for example conducted an analysis into the significance, and he found that the non-linear effects are particularly noteworthy at high Mach numbers when shocks occur on the blade, and the noise of these shock waves can then be modelled with a quadrupole source. [21].

4.2.2. Broadband noise

Broadband noise is characterised by a random and unpredictable nature, which results in a wide range of frequencies for the noise components. There are two main contributors to the broadband noise. First of all, the interaction of turbulent inflow with the leading edges of the blade causes an unsteady pressure field, which contributes to the broadband noise produced by propellers. The significance of this noise source depends on the amount of inflow turbulence. However, it can be quite substantial under operating conditions of high turbulence at low air speeds. Another contributor to broadband noise is the so called vortex noise, which has been defined as the sound that is generated by the formation and shedding of vortices in the flow behind a blade [18]. A common example of broadband noise generated by propellers is represented in Figure 4.4. It can be seen that the signal in the time domain plot indeed shows aperiodic behaviour, which results in a line in the frequency spectrum containing pressure perturbations at all frequencies.

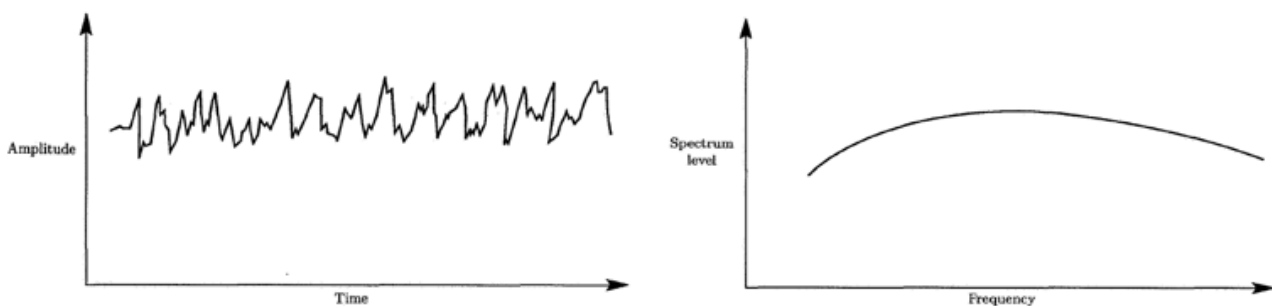


Figure 4.4: Characteristics of propeller broadband noise [13]

To conclude this chapter an example of an aircraft flyover analysis will be presented on the next page. This example was part of the Advanced Aircraft Noise Modelling and Measurements course taught as an elective at the aerospace faculty at the Delft University of Technology. The goal of this example is to become familiar with the concepts used when assessing an audio signal.

Analysis of an aircraft flyover

In this example, data of an aircraft flyover will be processed and analysed. The flyover data was obtained using a microphone array, which measured a total of 730,000 samples. The audio signal is modelled at a sample frequency of 40 kHz. A visualisation of the noise signal is presented in Figure 4.5. With the theory discussed in this chapter, the calculation for the OSPL, OASPL and the SEL values will be discussed in this example

Overall sound pressure level & Overall A-weighted sound pressure level

It was already established that the OSPL value can be determined with both the time domain signal and the frequency domain signal. In the time domain, one simply has to calculate the effective pressure for consecutive chunks of data, and by subsequently filling these values into Equation 4.5, the SPL values can be determined for the consecutive chunks, resulting in the OSPL-graph in Figure 4.6. To verify that the correct graph is obtained the OSPL signal should also be plotted using the frequency domain. This is done by again first dividing the signal into chunks. Subsequently, for every chunk a DFT should be performed, which makes it possible to obtain the PSD spectrum for the different chunks. Making use of a constant bandwidth analysis, the PBL values can be obtained for the successive bands making use of Equation 4.11. Finally, the OSPL value can be computed making use of Equation 4.12, which should be equal to the OSPL obtained in the time domain.

To get a more realistic view of how the noise level is perceived by the human ear, the OASPL is plotted. This is done by following a similar approach as determining the OSPL graph in the frequency domain. First of all, the data is again divided into chunks, and each data chunks is subsequently Fourier transformed. Next, the SPL values are obtained for a constant bandwidth analysis and subsequently, these values are A-weighted. The OASPL (for each chunk of data) can then be calculated according to Equation 4.14. Finally, the OASPL values for the different chunks of data are plotted as the orange graph in Figure 4.6.

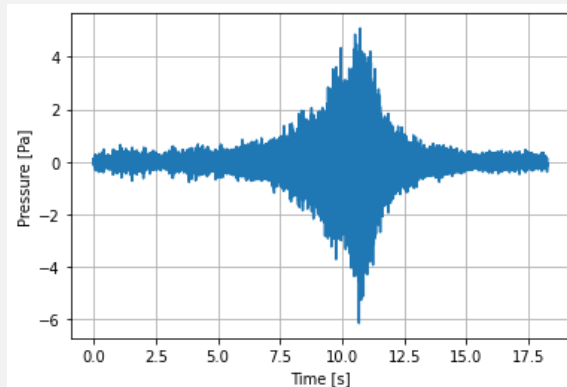


Figure 4.5: Audio of a flyover event

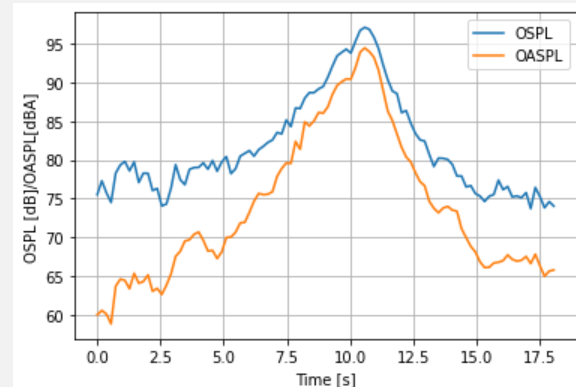


Figure 4.6: OSPL and OASPL plotted over time

Sound Exposure Level

Now the OSPL and OASPL values are obtained, it is time to calculate the SEL value of this aircraft flyover. Following the procedure explained in Subsection 4.1.2, the SEL value corresponding to the aircraft flyover can be calculated. First of all, the L_{Amax} and the 10 dBA downtime need to be determined. When this is done, the part of the signal that contributes to the SEL value calculation is found. Subsequently, the value of SEL can be calculated using Equation 4.7. The SEL corresponding to this aircraft flyover was found to be 95.8 dBA.

Theory on auralization process

In the past decades, the technique of auralization has emerged as a useful tool for designing and analysing acoustic environments. Auralization can be described as the process of creating an audible representation of an acoustic event happening in a virtual environment. It can be used to model the predicted noise levels in a variety of applications, ranging from noise assessment of new aircraft configurations to architectural acoustics. This chapter will discuss the theory behind the auralization technique, starting by discussing the concept of auralization in [Section 5.1](#). Followed by a section on sound propagation in [Section 5.2](#), and finally this chapter will be completed with a section on the signal processing steps required for auralization in [Section 5.3](#).

5.1. The concept of auralization

In the field of acoustics, the term *auralization* is used to describe the process of artificially creating an audible representation of an acoustic event. This can be compared to how *visualization* creates a visual representation of an environment. In other words, auralization is a technique that converts a calculated forecast into an audible sound, which can then be experienced in a virtual reality setting like the VCNS. Consequently, auralization enables humans to listen to non-existent acoustic scenarios, which for example makes it possible to experience the flyover of a new aircraft concept or new take-off procedures that are still in development. This process can be used to help communicate the expected changes to the affected community. There are various definitions of auralization found in literature, for example Vorländer presented the following definition in his book, which fittingly is called "Auralization" [22]:

"Auralization is the technique of creating audible sound files from numerical (simulated, measured, or synthesised) data."

The auralization process generally consists of three main steps: sound generation, sound transmission and sound reproduction. Below a brief overview on these three steps can be found:

1. **Sound generation:** The first step of auralization involves creating (or recording) a primary noise signal, which can then be fed to the sound transmission model. Additionally, a digital model of the environment needs to be generated in the first step. For a flyover, this includes specifying the aircraft geometry and the surrounding area. The model must also include the aircraft's operating conditions, such as information about the flight path and its speed and altitude.
2. **Sound transmission:** The second step ensures that the simulated sound is as realistic as possible when it reaches the observer. This is guaranteed by modelling how sound waves will behave in the modelled environment. The sound transmission model will take into account how sound waves propagate through the air, interact with the terrain, and finally reach the observer. To achieve this, factors such as the Doppler effect, atmospheric absorption and ground reflections will be taken into account when modelling an aircraft flyover.
3. **Sound reproduction:** The final step of the process is to generate an audio simulation of the aircraft flyover. This procedure involves using specialised software to create a realistic audio experience from the simulated sound waves. The produced audio can be listened to through headphones or speakers, and can subsequently be implemented into the VCNS to create a 3D experience of an aircraft flyover.

The use of auralization provides several insights that can be useful in a variety of applications. For example, regarding airport planning, auralization can help in understanding the acoustic impact of aircraft noise on neighbouring communities. Furthermore, in aircraft design, auralization can be useful as it allows for the evaluation of different design parameters in terms of their acoustic impact, which enables engineers to optimise new aircraft configurations for a minimum noise impact. Overall, the three steps of the auralization process for an aircraft flyover are critical in helping policy makers and designers understand the acoustic impact of a flyover and consequently enables them to make informed decisions about noise mitigation strategies.

5.2. Atmospheric propagation

This section will discuss how sound propagates from a source to a receiver on the ground. During this trip the sound travels through the atmosphere, and is influenced by four distinct propagation effects that alter the sound from the source to how it is perceived by the listener on the ground. The propagation effects that are considered in this section are the Doppler effect in [Subsection 5.2.1](#), the ground reflection in [Subsection 5.2.2](#), spherical spreading in [Subsection 5.2.3](#), and the atmospheric absorption in [Subsection 5.2.4](#). By considering these four propagation effects, a better understanding is obtained on how sound travels through the atmosphere and how it interacts with its environment.

5.2.1. Doppler effect

The Doppler effect is a phenomenon that comes into play when there is relative motion between a noise source and an observer. The Doppler effect is commonly observed in our daily lives, such as the sound of an ambulance passing by or an aircraft flying over your head. The effect describes the perceived change in frequency of the emitted sound as the noise source moves towards, and away from the observer. This phenomenon of the frequency shift can be calculated with [Equation 5.1](#).

$$f_o = \frac{f_s}{1 - M_x \cos\theta} \tag{5.1}$$

In this equation, the frequency perceived by the observer is denoted as f_o , and the frequency emitted by the noise source is expressed as f_s . Furthermore, M_x stands for the Mach number, which divides the aircraft's speed V by the speed of sound c . Finally, θ represents the angle between the observer and the aircraft. The cosine of the angle θ can be computed with $\cos\theta = -\frac{vt}{r}$, with t being the elapsed time and r the distance from the noise source to the observer. This angle ensures that when the source is moving towards the observer, the frequency of the sound wave increases, resulting in a higher pitch. On the other hand, when the noise source is moving away from the observer, the frequency decreases, resulting in a lower pitch of the sound [15].

5.2.2. Ground reflection

When a sound wave encounters a surface, such as the ground or a building, it can be reflected or even absorbed. If the surface is rough, the reflected wave can be scattered in multiple directions, which results in a diffuse reflection. However, most of the times, it is assumed that the reflection is specular, which means that the sound wave is perfectly reflected of the ground, as shown in [Figure 5.1](#). Consequently, in the case portrayed in the figure, a microphone or more generally an observer will receive a direct (r_1) and a ground-reflected wave (r_2). The path lengths of these two rays can be calculated with [Equation 5.2](#) and [Equation 5.3](#).

$$r_1 = \sqrt{(x_s - x_m)^2 + (h_s - h_m)^2} \tag{5.2} \quad r_2 = \sqrt{(x_s - x_m)^2 + (h_s + h_m)^2} \tag{5.3}$$

In the given equations, the variable x refers to the horizontal position and h represents the height above the ground. The subscripts used in these equations refer to either the position of the source or the microphone. To be more specific subscript s refers to the position of the sound source, while subscript m stands for the position of the microphone (or observer). A detailed explanation on how this event can be included in the noise analysis is described by Salomons [23]. However, during this Msc. thesis the assumption is made that the ground is acoustically hard, and therefore the reflection of the sound is assumed to be 100%.

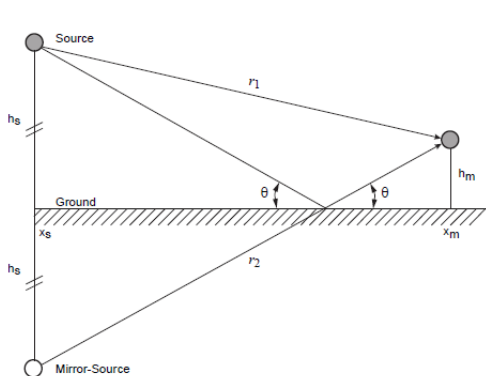


Figure 5.1: Reflection of a sound ray via the ground [24]

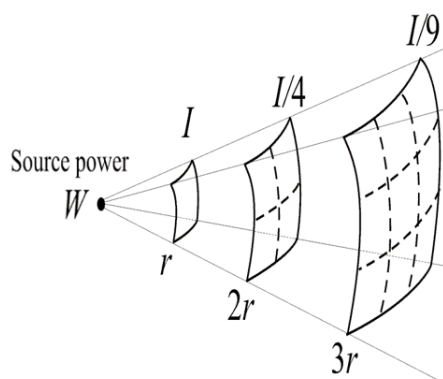


Figure 5.2: Effect distance has on the noise intensity: the spherical spreading effect

5.2.3. Spherical spreading

Spherical spreading is an acoustic phenomenon that occurs when sound waves move through a medium, such as air, in a three-dimensional space. The theory behind the spreading loss is that when a sound wave moves away from a noise source, it spreads out in all directions, forming a spherical wavefront. In other words, it can be said that the power is radiated equally in all directions around the noise source, which leads to a decrease in sound intensity further away from the source. This effect is depicted in [Figure 5.2](#). The relationship introduced above between the sound intensity and the distance is generally known as the *inverse square law*, which ultimately will result in a decrease in sound level. The loss in sound level due to spherical spreading can be calculated using [Equation 5.4](#). In this equation r represents the distance away from the noise source, and r_{ref} is the reference distance at which the sound level is known. When the distance between the point source and the observer is doubled, the ratio between the distance r and the reference distance r_{ref} also doubles. As a result, there is a 6.0 dB loss due to spherical spreading, as given by $\Delta SPL = 20 \log_{10}(2) \approx 6.0$ [15]. It should be noted that the spherical spreading as indicated by [Equation 5.4](#) only applies for a point source. In the case of an aircraft, if the distance between its noise sources (e.g. its engines, flaps and landing gear) is relatively small compared to the distance between the aircraft and the observer, only then the aircraft can be approximated by a single point source. Additionally, the noise sources should be incoherent, which means that no destructive interference occurs between them.

$$\Delta SPL = 20 \log_{10} \left(\frac{r}{r_{ref}} \right) \quad (5.4)$$

$$\Delta SPL = \alpha \Delta r \quad (5.5)$$

5.2.4. Atmospheric absorption

When an aircraft is airborne, it produces sound waves that propagate through the atmosphere. As a result, a portion of the sound energy is absorbed by the atmosphere during this process, which leads to a decrease in sound level at the observer. The extent of this energy loss, also known as attenuation, is determined by the sound attenuation coefficient. This coefficient depends on numerous factors such as the frequency of the sound wave, the humidity of the atmosphere and the temperature. Following the fact that the unit of the attenuation factor is $[dB/m]$, the attenuation of the sound energy will increase with an increase of the aircraft's altitude as the sound wave must travel through a larger portion of the atmosphere. Moreover, the speed and direction of the wind can also affect the propagation of the emitted sound waves, leading to further changes in the sound level at the ground. With the attenuation factor known, the transmission loss of sound can be computed using [Equation 5.5](#), where Δr denotes the path length [15]. In order to account for the atmospheric absorption in the analysis, an atmospheric filter will be applied to the direct and reflected sound waves [24].

5.3. Signal processing for auralization

The overall acoustic transmission loss of the sound produced by an aircraft flyover is accumulated from the propagation effects, as described in [Section 5.2](#). In order to apply the propagation characteristics to the source noise three primary Digital Processing Steps (DPS) are required: a gain, a delay line and a filter. Including a gain allows for spherical spreading to be incorporated into the model, while the time delay line takes into account the absolute delay, which can vary over time in order to model the Doppler effect. By adding a filter the atmospheric absorption is included in the simulation. Together these steps allow for the implementation of the required propagation effects to the noise produced by the source [24]. In [Figure 5.1](#), it was established that the reflection of the sound wave from the ground creates an additional path to reach the observer, which results in two audio signals that need to be processed before being summed. It is critical that the signal processing steps follow a special order to guarantee correct modelling. In the auralization process, this sequence is either TGF, TFG or GTF, where an example of GTF is presented in [Figure 5.3](#) and stands for Gain-Time-Filter processing steps. One important aspect to take into consideration is that the Doppler effect (time delay) is applied before the absorption (filter). This is necessary to guarantee the correct modelling of the propagation effects.

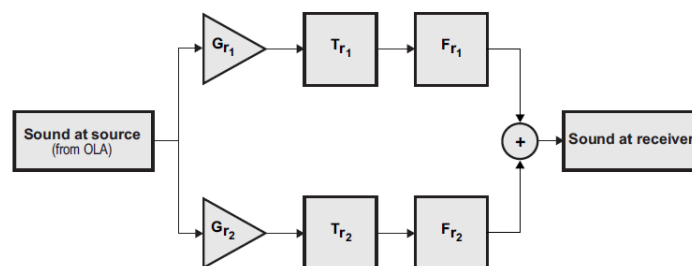


Figure 5.3: The necessary signal processing steps to incorporate the propagation effects [24]

State-of-the-art

To make a contribution to the scientific community, it is important to generate new knowledge that was either unknown beforehand, or that significantly advances existing knowledge by providing new insights that improve upon previous conducted research. Therefore, it is of utmost importance to conduct a comprehensive literature review on the existing research to ensure that the proposed project will add something to the current state of knowledge. To achieve this the objective of this section will be to understand what research has been conducted in the past, and consequently obtain ideas on how to develop a noise model for a DEP aircraft.

The majority of the analytical DEP noise models that were analysed roughly follow the same structure and flow, which is illustrated in [Figure 6.1](#). The standard procedure is to start by defining the propeller geometry and the operating conditions of the aircraft. This is followed by implementing an aerodynamic model which calculates the propeller performance coefficients. With these coefficients known, the noise generated by an isolated propeller can be computed. Subsequently, a reference DEP aircraft is introduced for which the isolated noise sources will be implemented on the location of the propellers to compute the noise produced by the entire DEP configuration. As every analytical DEP noise model builds upon the noise produced by an isolated propeller, [Section 6.1](#) will discuss the methodology of modelling the noise of an isolated propeller. In addition to discussing the theory, it will also be put into practice in this section by comparing the isolated propeller models from NLR and Delft University of Technology in [Subsection 6.1.3](#). Following this section, multiple methods which describe the modelling of the noise of a DEP configuration will be discussed in [Section 6.2](#).

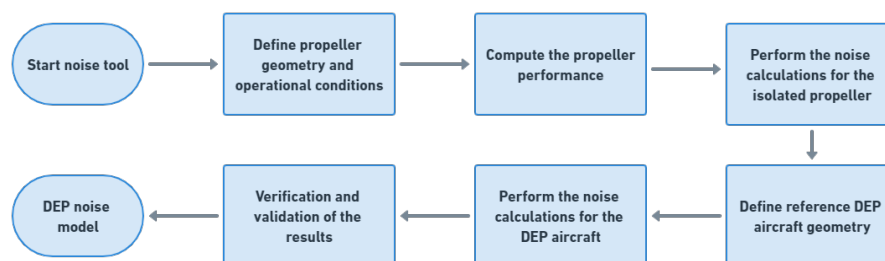


Figure 6.1: Flowchart showing the general overview of the main processes involved in a DEP noise model

6.1. Isolated propeller model

In this section the most commonly used methodology used in a noise model of an isolated propeller will be discussed. This will be done by first examining the used propeller performance prediction methods in [Subsection 6.1.1](#). Followed by a section on the Helicoidal Surface Theory (HST), which is a theory developed by Hanson to determine the noise levels of an isolated propeller analytically in [Subsection 6.1.2](#). This section is concluded by a comparison of the isolated propeller models of NLR and TUD in [Subsection 6.1.3](#)

6.1.1. Propeller performance prediction methods

The most commonly used models to design and analyse propellers rely on standard blade element theory. Typically, blade element models are designed for propellers operating in axial flight, which means that the axis of rotation is aligned parallel to the direction of the free stream. Additionally, these models usually assume the propeller to have straight blades. However, this can easily be modified if a propeller with sweep is desired, following the work by S. Burger [25]. The primary advantages of these blade element models are their relatively low computation time, combined with high accuracy. For these reasons blade element models are preferred over more complex methods, like computational fluid dynamics (CFD) codes, when a large number of computations is required. Furthermore, it is noteworthy that according to O.Gur and A.Rosen [26], using more complicated models for propeller performance calculations in axial flight does not necessarily result in superior results over the simple blade element models.

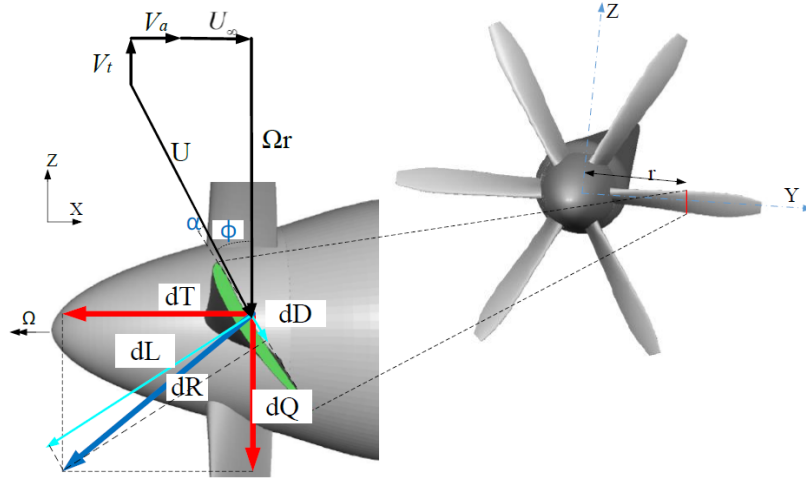


Figure 6.2: Velocity and force vectors of a blade element [27]

In a nutshell, the theory behind these models is based on dividing each of the propeller's blades into small segments (elements), which are all assumed to behave aerodynamically similar to a wing in two-dimensional flow. On top of this, it is also assumed that there is no interaction between neighbouring segments. This last assumption was validated by C.Lock and H.Bateman [28]. In Figure 6.2 a cross section of such a blade element is presented. When a blade has been divided into segments, the lift and drag coefficients of each segment can be determined by several variables, such as the local angle of attack, Mach number and Reynolds number. These parameters, in their turn, are all dependent on the cross sectional resultant velocity, which is obtained by combining the free stream velocity, rotational velocity of the blade and the induced velocities. While the free stream velocity and rotational velocity are known, as they stem from the operating conditions, the induced velocity components remain unknown. In order to compute these induced velocities a different model is required, which needs to be used along with the blade element model. Numerous models have been employed over time to achieve this objective, including momentum models [29], lifting-line models [30], and vortex models [31]. When the induced velocities are computed with one of the additional models, all components of the cross sectional velocity are available, which means that the effective velocity (U) can be calculated. This velocity determines the inflow angle (ϕ) with its tangential velocity component (V_t) and the axial component (V_a), as presented in Equation 6.1. With ϕ known the angle of attack (α) can be calculated by subtracting ϕ from the local pitch angle (β), as described in Equation 6.2. Furthermore, the effective velocity also determines the cross-sectional Mach number (M) and the Reynolds number (Re).

$$\phi = \tan^{-1}\left(\frac{V_{ax}}{V_{tgt}}\right) \quad (6.1)$$

$$\alpha = \beta - \phi \quad (6.2)$$

With the values of the effective velocity, cross-sectional Mach number and Reynolds number known, the lift and drag coefficients per segment, $C_l(\alpha, M, Re)$ and $C_d(\alpha, M, Re)$ respectively, can be computed utilising a two-dimensional aerodynamic data base, like XFOIL. Subsequently, the lift and drag forces per segment can be calculated using Equation 6.3 and Equation 6.4 respectively. The lift and drag values computed are then used to calculate the thrust and torque per section using Equation 6.5 and Equation 6.6.

$$dL = \frac{1}{2} \rho U^2 C_l(\alpha, M, Re) \quad (6.3) \quad dD = \frac{1}{2} \rho U^2 C_d(\alpha, M, Re) \quad (6.4)$$

$$dT = dL \cos\phi - dD \sin\phi \quad (6.5) \quad dQ = dL \sin\phi + dD \cos\phi \quad (6.6)$$

The method explained above, describes how to compute the thrust and torque at a single section of the blade. The performance of the entire propeller can subsequently be obtained by integrating the thrust and torque contributions of all sections along the blade span and multiplying it with the number of blades (N_B). This procedure is presented in Equation 6.7 and Equation 6.8 [9].

$$T = \rho N_B \int_{hub}^{tip} dT dr \quad (6.7)$$

$$Q = \rho N_B \int_{hub}^{tip} dQ dr \quad (6.8)$$

6.1.2. Isolated propeller noise prediction method

The two isolated propeller models that will be analysed in [Subsection 6.1.3](#), both use the same theory to model the tonal nature of the sound emitted by a propeller. This theory is known as the Helicoidal Surface Theory, which was developed by Hanson [32]. Hanson extended the theory by Gutin [33], who was responsible for the first successful propeller noise theory in harmonic form. Even though there exist many other theories to model propeller noise sources, such as the asymptotic theory by Crighton and Perry [34], or the lifting line model by Brouwer [35], understanding the Helicoidal Surface Theory will be the main objective of this section.

Hanson's method predicts the propeller noise characteristics in the frequency domain. The methods in the frequency domain have a couple of advantages over the methods in the time domain, namely the equations used in the frequency domain are straightforward enough to be coded on personal computers. Furthermore, they provide a clear understanding on how the propeller design features impact the noise characteristics. The theory behind Hanson's method is based on Goldstein's acoustic analogy [36], which was originally used to analyse sound produced by moving surfaces in a moving fluid. His analogy can be expressed as follows:

$$\rho'(x, t) = -\frac{1}{c_0^2} \int_{-T}^T \int_{S(\tau)} \left(\rho_0 V_n \frac{\delta G}{\delta \tau} + f_i \frac{\delta G}{\delta y_i} \right) dS(y) d\tau + \frac{1}{c_0^2} \int_{-T}^T \int_{V(\tau)} T_{ij} \frac{\delta^2 G}{\delta y_i \delta y_j} dy d\tau \quad (6.9)$$

In the given equation, the symbol c represents the speed of sound, ρ denotes the density of the fluid, where the subscript zero corresponds to the equilibrium value of the density. V_n stands for the normal velocity of the surface relative to the fluid, T_{ij} denotes an element of the Lighthill stress tensor, f_i signifies the vector of force per unit area exerted on the surface, G represents the Green's function, $S(\tau)$ is the impermeable surfaces at emission time τ , and $V(\tau)$ represents the source volume. Furthermore, the integration is carried out over the range of the source time, from $-T$ to T .

The far field equations of the Helicoidal Surface Theory are derived in full detail in Hanson [32]. However, the most important equations will be described below. First of all, Hanson has included a Doppler shift term to include forward flight in the analysis. This modifies the frequency perceived by the observer as explained in [Subsection 5.2.1](#). Blade sweep is considered as a phase lag effect, which can be modelled with [Equation 6.10](#). In addition to the phase lag resulting from blade sweep, one can incorporate a phase lag resulting from propeller offset, which can be determined using [Equation 6.11](#). It should be noted that these equations are only used if sweep and/or offset are present in the treated propeller geometry.

$$\phi_s = \frac{2mB M_T}{M_r (1 - M_x \cos(\theta))} \frac{MCA}{D} \quad (6.10) \quad \phi_0 = \frac{2mB}{z M_r} \left(\frac{M_r^2 \cos \theta - M_x}{1 - M_x \cos(\theta)} \right) \frac{FA}{D} \quad (6.11)$$

In the given equations, the symbol m represents the number of harmonics, M_T denotes the rotational tip Mach number, M_r stands for the effective Mach number, M_x corresponds to the flight speed Mach number. D is the diameter of the propeller, θ represents the radiation angle from the propeller axis to the observer point, MCA stands for Mid Chord Alignment and FA denotes the Face Alignment, which is the distance normal to the blade at the tip. Furthermore, the effective Mach number, M_r can be computed using [Equation 6.12](#), where the variable z stands for the radial position of a blade element as a fraction of the radius.

In his analysis, Hanson made the assumption that the thickness and loading sources act on the advance helix, which is the surface swept by a radial line rotating at a specific angular velocity, and moving forward with the flight speed. By determining the angle of attack relative to the helical surface the loading of a propeller blade can be computed. With this information the thickness and steady loading noise can then be modelled following a set of mathematical expressions. First of all, the acoustic pressure can be computed making use of [Equation 6.13](#).

$$M_r = \sqrt{M_x^2 + z^2 M_T^2} \quad (6.12) \quad p(t) = \sum_{m=-\infty}^{\infty} P_{mB} \exp(-imB\Omega t) \quad (6.13)$$

In the given equation P_{mB} represents the Fourier transform of the pressure at the m^{th} harmonic of the BPF. The variable B represents the number of blades, and Ω denotes the frequency associated with the angular speed. Furthermore, the term P_{mB} consists of the following three components: P_{Vm} , which is the volume displacement component, which can be calculated using [Equation 6.14](#). P_{Dm} represents the drag dipole, which can be calculated using [Equation 6.15](#) and P_{Lm} stands for the lift dipole, which can be calculated using [Equation 6.16](#). P_{mB} is then calculated by adding these components together. It should be noted that the quadrupole sources from the original theory are omitted in this thesis. This decision was made as these sources account for the rise of non linear effects that occur at high Mach numbers, and for this thesis Mach numbers above 1 will not be analysed. Furthermore, it is also worth mentioning that axial inflow is assumed in this theory.

$$P_{Vm} = -\frac{\rho_0 c_0^2 B \sin \theta \exp \left[imB \left(\frac{\Omega_D r}{c_0} - \frac{\pi}{2} \right) \right]}{8\pi \left(\frac{y}{D} \right) (1 - M_x \cos \theta)} x \frac{1}{2} \int_{root}^{tip} M_r^2 e^{i(\phi_0 + \phi_s)} J_{mb} \left(\frac{mBz M_t \sin \theta}{1 - M_x \cos \theta} \right) x 2k_x^2 t_b \psi_V(k_x) dz \quad (6.14)$$

$$P_{Dm} = -\frac{\rho_0 c_0^2 B \sin \theta \exp \left[imB \left(\frac{\Omega_D r}{c_0} - \frac{\pi}{2} \right) \right]}{8\pi \left(\frac{y}{D} \right) (1 - M_x \cos \theta)} x \frac{1}{2} \int_{root}^{tip} M_r^2 e^{i(\phi_0 + \phi_s)} J_{mb} \left(\frac{mBz M_t \sin \theta}{1 - M_x \cos \theta} \right) x ik_x C_D \psi_D(k_x) dz \quad (6.15)$$

$$P_{Lm} = -\frac{\rho_0 c_0^2 B \sin \theta \exp \left[imB \left(\frac{\Omega_D r}{c_0} - \frac{\pi}{2} \right) \right]}{8\pi \left(\frac{y}{D} \right) (1 - M_x \cos \theta)} x \frac{1}{2} \int_{root}^{tip} M_r^2 e^{i(\phi_0 + \phi_s)} J_{mb} \left(\frac{mBz M_t \sin \theta}{1 - M_x \cos \theta} \right) x ik_y C_L \psi_L(k_x) dz \quad (6.16)$$

In these equations y represents the vertical distance between the observer and the propeller axis, r stands for the distance from the origin to the observer, D is the propeller diameter, C_L and C_D correspond with the lift and drag coefficient of the blade section, i represents the imaginary unit (defined as $i^2 = -1$), and t_b stands for the thickness to chord ratio, which is dependent on the blade's geometry. Furthermore, k_x and k_y represent the non-dimensional wave numbers and are defined by Equation 6.17 and Equation 6.18 respectively.

$$k_x = \frac{2mBB_D M_T}{M_r(1 - M_x \cos \theta)} \quad (6.17) \quad k_y = \frac{2mBB_D}{zM_r} \frac{M_r^2 \cos \theta - M_x}{M_r(1 - M_x \cos \theta)} \quad (6.18)$$

The functions ψ_V , ψ_D and ψ_L are distribution functions that describe the distribution of the thickness, drag and lift components respectively over the chord. These functions are defined by Equation 6.19, Equation 6.20 and Equation 6.21.

$$\psi_V(k_x) = \int_{-0.5}^{0.5} H(x) e^{ik_x x} dx \quad (6.19) \quad \psi_D(k_x) = \int_{-0.5}^{0.5} f_D(x) e^{ik_x x} dx \quad (6.20) \quad \psi_L(k_x) = \int_{-0.5}^{0.5} f_L(x) e^{ik_x x} dx \quad (6.21)$$

The term $H(x)$ in Equation 6.19 denotes the normalised thickness distribution function of the airfoil section that is being considered. Typically, a propeller becomes thinner near the tip, and therefore the thickness distribution function reflects this trend. An example of such a distribution function is presented in Figure 6.3. Where the maximum value of $H(x)$ equals 1, and the integration is performed from the leading edge to the trailing edge. Furthermore, the functions $f_D(x)$ and $f_L(x)$ represent the drag and lift distribution respectively over the chord.

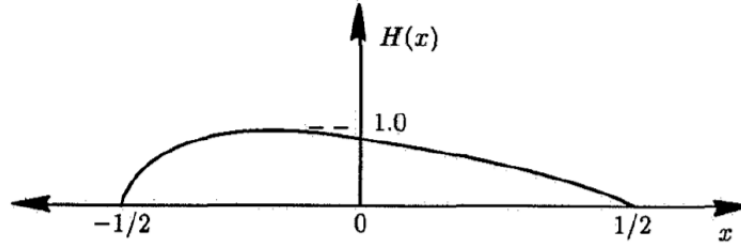


Figure 6.3: Example of a thickness distribution [19]

6.1.3. Comparison of NLR and TUD isolated propeller noise model

In this subsection the isolated propeller noise models of NLR and TUD will be analysed and compared. It is good to know that the isolated propeller model from TUD is known under the name Helix-tool, and will in the future be called accordingly. The objective of this subsection is to determine which of the two models is more suitable to form the basis of the DEP noise model in the remainder of the research. First of all, both models will be analysed on a qualitative-scale, which will be followed by a quantitative analysis where both models will be compared to experimental data.

Qualitative analysis

From a first glance both models consist of three major processes, which are the aerodynamic analysis, the performance analysis and the noise analysis. A representation of the flow of these processes is provided in Figure 6.4, where the yellow blocks stand for the outputs of the different analyses. Furthermore, it is noteworthy that both tools use the same methodology for the aerodynamic and noise analysis, but differ in their approach to compute the propeller performance coefficients.

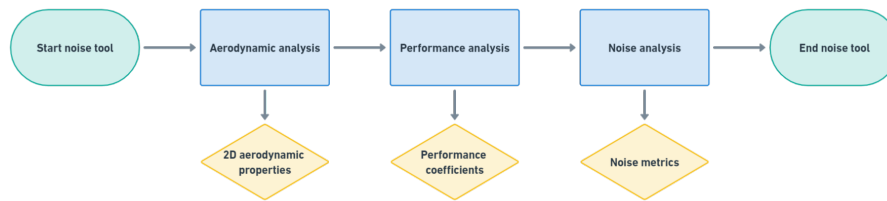


Figure 6.4: Flow chart of a general isolated propeller noise model

For both tools the aerodynamic analysis consists of defining the operational conditions and propeller geometry. Followed by determining the 2D aerodynamic properties with XFOIL, which are needed for the performance analysis. XFOIL is a tool designed by M. Drela [37], and can be used to develop and analyse airfoils. The input for XFOIL consists of the airfoil coordinates of the analysed propeller, the Reynolds number per blade section (Re) and a range of angle of attack (α) values. Consequently, the output of XFOIL are the lift coefficients (C_l), the drag coefficients (C_d), the moment coefficients (C_m) and the corresponding angles of attack. Subsequently, these outputs can be used as the inputs for the performance analysis.

The objective of the performance analysis is to obtain the power coefficient (C_p) and the thrust coefficient (C_T), which are needed to predict the noise produced by a propeller. For the performance analysis both models have a different approach. First of all, the NLR tool uses a standard BEMT model as described in [Subsection 6.1.1](#) combined with a Newton Raphson iteration to compute the induced flow angle. How the model is implemented is described in more detail in Geng et al. [38]. Secondly, the Helix tool uses an external tool called XRotor [39]. XRotor utilises a propeller lifting line theory that employs an iterative approach to compute the circulation and induced velocities. The lifting line theory iteratively calculates these quantities until convergence is attained. In XRotor, there are three models available to calculate the induced velocities: the graded momentum formulation, the potential formulation and the vortex formulation [19]. Among these methods, the graded momentum formulation is the least computationally expensive, while the vortex formulation is the most time consuming. In the case of the Helix tool, the potential formulation is chosen because the analysed propeller blade lacks sweep. Furthermore, the graded momentum formulation is not suitable for this scenario as it is only applicable for advance ratios below 0.5π . Similarly, the vortex formulation would unnecessarily increase the computational time. Furthermore, it is noteworthy that both tools employ the Prandtl-Glauert compressibility correction, which remains valid for Mach numbers up to around 0.7. This correction theory is specifically designed for subsonic conditions and produces unreliable outcomes beyond Mach 0.7 [19]. As the performance analysis is the only substantial difference between the two models, it will be interesting to see the differences between the computed performance coefficients. According to Rosen [26], who analysed different BEMT models, the differences between a standard BEMT model and a lifting line model should be insignificant for propellers in axial flight. If this is also the case for the Helix-and NLR tool, will be analysed in the next section.

As mentioned earlier in this section, both tools use the same methodology to predict the noise produced by a propeller. This methodology is known as the Helicoidal Surface Theory, which is explained in detail in [Subsection 6.1.2](#). Following this methodology, both models have implemented the thickness noise and the loading noise as contributors to the produced noise. In addition to these noise elements, the NLR tool also includes the broadband noise produced by a propeller. This is done by scaling wind tunnel measurements to the diameter of the analysed propeller. However, in the comparison of both models only the contribution of the tonal noise will be analysed in order to assess the differences in both models without changing too many parameters. Additionally, for this comparison the source noise will be used to compare both models, which means that the propagation effects explained in [Section 5.2](#) are also not included in this comparison.

Quantitative analysis

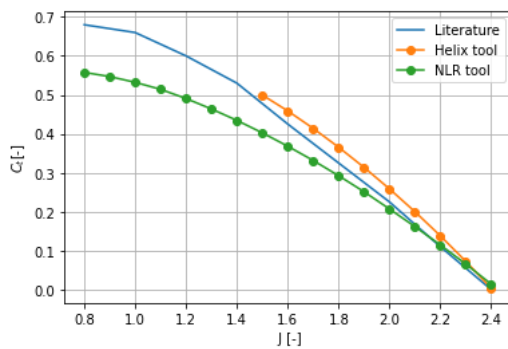
In this section the theoretical results obtained from both models are compared against literature data. First of all, the propeller performance is compared. This is a crucial analysis because the acoustic outcomes of both models are significantly influenced by the propeller performance. The thrust coefficient and the power coefficient calculated by the two tools are compared against experimentally obtained data. Subsequently, the acoustic data obtained from the Helix-and NLR tool are compared with each other, as well as with experimental data. This is done considering various operating conditions and two propeller configurations.

Performance results

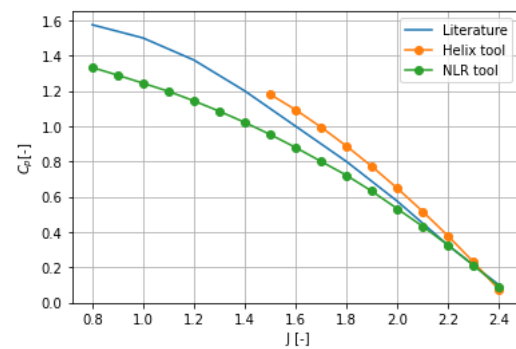
The SR-2 propeller has been selected as the propeller to perform the performance comparison with, as an extensive set of data is available for this propeller. The data is obtained from Stefko [40], where an 8-bladed SR-2 propeller was conducted to measurements in the NASA Supersonic Wind Tunnel. During these measurements various blade angles were tested at different free-stream Mach numbers, representing conditions such as take-off and climb. In order to compare the performance of both models with the experimental data, two

operating conditions were selected and used as input parameters in both models. These operating conditions are a Mach number of 0.2 with a blade setting of 45.8 deg and a Mach number of 0.27 with a blade setting of 45.8 deg . These conditions were selected as according to Stefko [40] they represent what the Mach number would approximately be during lift-off and an initial climb-out, which are the areas of interest for this thesis.

First of all, in Figure 6.5(a) and Figure 6.5(b) the thrust and power coefficient respectively are presented as a function of advance ratio for a freestream Mach number of 0.2 and a blade setting of 45.8 deg . The results reveal that the Helix tool fails to converge for the complete range of advance ratios. This discrepancy could potentially be attributed to a significant portion of the propeller blade being operated in a stalled condition. At lower advance ratios the inflow angles are smaller, and given the current blade setting, this can lead to substantial angles of attack at various blade sections. On the other hand, the NLR tool does provide results for the lower advance ratios. This can be attributed due to the relatively simple BEMT model incorporated in the NLR tool, which neglects the occurrence of stall. This also explains why the NLR tool differs significantly from the literature data at the lower advance ratios, and shows better agreement with the literature data from $J > 1.4$ for both the thrust and power coefficient. This finding is also in accordance with the conclusion presented by Geng et al. [38], whom investigated the BEMT model used in the NLR tool. The Helix tool in general shows good resemblance with the experimentally obtained data for both performance coefficients.



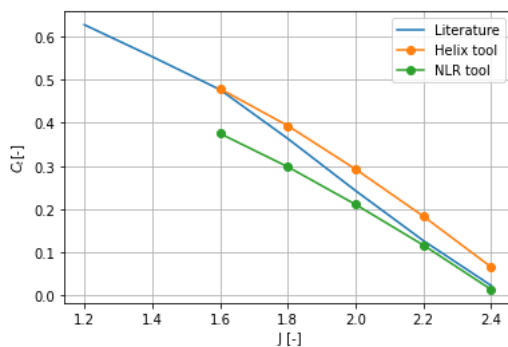
((a)) Thrust coefficient as a function of advance ratio



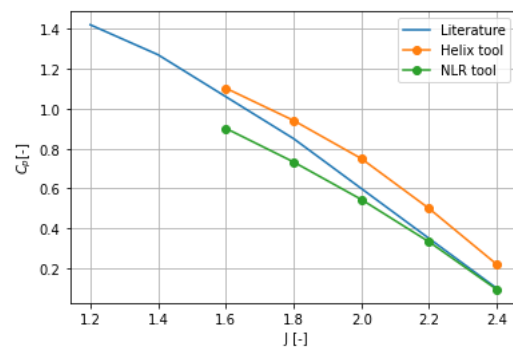
((b)) Power coefficient as a function of advance ratio

Figure 6.5: The thrust and power coefficient for axial Mach number of 0.2 and $\beta_{0.75} = 45.8$

In Figure 6.6(a) and Figure 6.6(b) the performance coefficients are presented as a function of the advance ratio for a Mach number of 0.27 and a blade setting of 45.8 deg . Now, it was chosen to start the range of advance ratios from the first point where the Helix tool would provide results. Again it can be seen that at lower advance ratios the NLR tool performs worse than at higher advance ratios. However, it must be said that from $J = 2.0$ onwards the results show excellent similarities with the performance coefficients obtained in the literature. On the other hand, for the Helix tool an almost constant over-prediction is obtained, and therefore it can be said that for this operating condition the Helix tool performs a little worse compared to the NLR tool and also compared to the results obtained from the Helix tool at the previous operating condition.



((a)) Thrust coefficient as a function of advance ratio



((b)) Power coefficient as a function of advance ratio

Figure 6.6: The thrust and power coefficient for axial Mach number of 0.27 and $\beta_{0.75} = 45.8$

Acoustic results

Now that the performance of both tools has demonstrated satisfactory agreement with the experimentally obtained performance data, it is time to evaluate the acoustics predicted by both models. First of all, both models will be compared against each other at an operating condition where the performance coefficients of both models are similar, such as $M = 0.2$ and $J = 2.3$ (test case 1). This analysis is conducted before comparing both

models with experimental data to verify that both models have been altered correctly to model the acoustics of a noise source, and to analyse if the HST has been implemented correctly in both models. When this has been verified the models will be compared with wind-tunnel data (test case 2) and measurements from an actual flyover (test case 3). The input parameters of all test cases are presented in [Table 6.1](#).

Table 6.1: Input parameters for the different test cases

	Test case 1	Test case 2	Test case 3
M_x [-]	0.2	0.09	0.12
J [-]	2.3	0.592	0.597
y [m]	9.8R	0.889	12.19
n_{blades} [-]	8	4	3
$\beta_{0.75}$ [deg]	45.8	20.6	18

First of all, in case 1 the OSPL of both tools are compared when the performance coefficients are roughly the same. This case is performed to verify if the Helicoidal Surface Theory has been implemented correctly in both models, as with similar performance coefficients both models are expected to compute similar noise levels. The Helix tool computed a thrust coefficient of 0.073 and a power coefficient of 0.23, where the NLR tool computed values of 0.066 and 0.21 for the thrust-and power coefficient respectively. The results of case 1 are presented in [Figure 6.7](#), where it can be seen that the OSPL values of both tools are indeed very similar, and are believed to differ due to the thickness noise being the more dominant noise source.

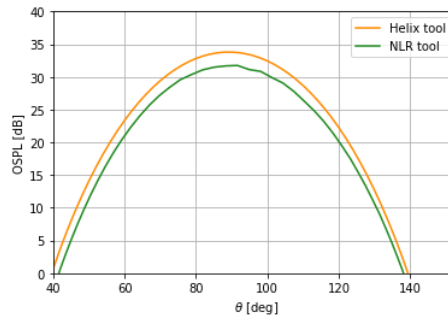
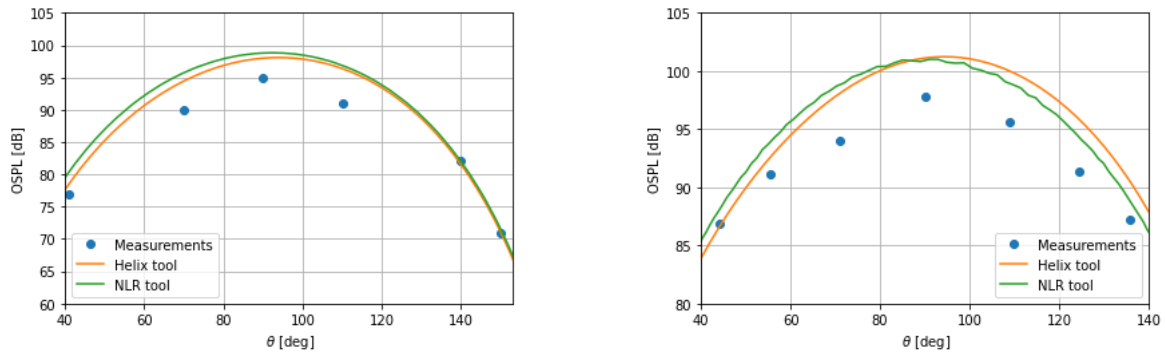


Figure 6.7: Case 1: Directionality plot comparing the OSPL of the Helix-and NLR tool, with $M_x = 0.2$, $J = 2.3$, $y = 9.8R$ m, $n_{blades} = 8$ and $\beta_{0.75} = 45.8$ deg

Next, for test case 2 the directionality plots of both models are compared with experimental data from Block [41]. This report describes an experimental study conducted on the SR-2 propeller to measure propeller noise. The measurements were carried out in the NASA Langley 4-by 7 meter wind tunnel, which has been acoustically treated to minimise noise from other sources within the tunnel. For the measurements, microphones were positioned at a constant vertical distance of 0.889 m below the propeller centre. A total of eleven microphones were mounted on a carriage that could move parallel to the propeller centerline, allowing for the propeller noise to be measured at various angles. Furthermore, the measured sound pressure levels are adjusted for free field level conditions by subtracting 6 dB. This correction accounts for the reflection caused by the presence of hard surfaces. This correction makes it more convenient to compare the experimental data with the calculated results from the Helix tool and the NLR tool. Moreover, it should be noted that for this comparison analysis a blade diameter of 0.429 m is selected. The results of the comparison of test case 2 are presented in [Figure 6.8\(a\)](#). Both models show relatively good agreement with the measured data for the angles ranging from 40 deg to 150 deg. The maximum OSPL value obtained from the measurements is 95 dB, whereas both models compute an OSPL of nearly 100 dB. Taking into consideration that the Helicoidal Surface Theory is actually a method to compute the noise strictly in the far field, a 5 dB difference between the models and the measurements at a vertical distance of 0.889 m is deemed reasonable. The hypothesis is that for a larger distance between the propeller and the microphones both models will predict OSPL values closer to the measured data. To test this hypothesis test case 3 was added to report.

Finally, for test case 3 the output of both models will be compared to a full-scale outdoor experiment, which is conducted by Elbers and documented in [42]. For this experiment the Pipistrel Velis Electro was used as an aircraft. This aircraft is a fully-electric powered aircraft, which makes it a very suitable aircraft to compare both models with as the propeller noise will be the primary noise source of this aircraft due to its electric engine. For obtaining the full-scale outdoor data, a microphone array consisting of 64 microphones is deployed in an Underbink configuration. More information about the test set-up can be found in Elbers [42]. The results of the comparison with the flyover event are presented in [Figure 6.8\(b\)](#). It can be observed that similarly as in test

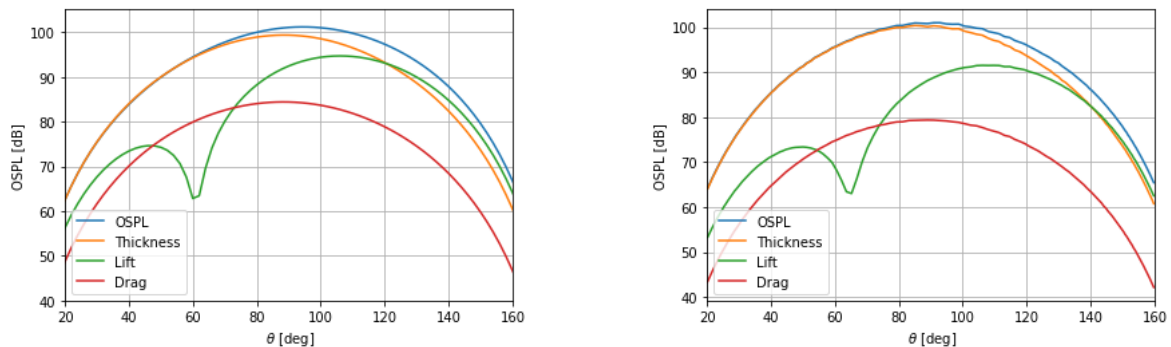
case 2 the OSPL has been predicted relatively well by both models compared to the measurements. The peak OSPL value measured is 98 dB, and both models predict an OSPL of roughly 101 dB, which is indeed closer to the measured data compared to test case 2, as expected.



((a)) Case 2: Directionality plot comparing experimental data from Block [41] with both models ((b)) Case 3: Directionality plot comparing flyover data from Elbers [42] with both models

Figure 6.8: Directionality plots of test cases 3 and 4

To verify whether the individual noise components have been modelled correctly they have been plotted in Figure 6.9(a) and Figure 6.9(b) for the Helix- and NLR tool respectively, for test case 4. It can be seen that the graphs of all components share great resemblance between the two models. Additionally, a check is performed with the noise component of the drag. The Helix tool computed a power coefficient of 0.076, where the NLR tool predicted a power coefficient of 0.045 for test case 3. Following Equation 3.4 it can be determined that with a similar drag, a higher power coefficient will result in a higher power, which will result in a higher noise level due to a higher loading. In Figure 6.9 this expectation can indeed be observed as it can be seen that the noise level computed due to drag is 82 dB for the Helix tool and 80 dB for the NLR tool.



((a)) Directionality plot of all noise components computed by the Helix tool ((b)) Directionality plot of all noise components computed by the NLR tool

Figure 6.9: Directionality plot of all noise components computed by the Helix- and NLR tool

Concluding remarks on the comparison

Based on the preceding sections, this section will provide some concluding remarks on the comparison between both models, and select one of the models to be the main building block of the distributed propulsion noise model. When making a decision between the two models, two elements were found to be very important selection criteria, namely the accuracy and the run time. Since the main goal of this thesis is to construct a noise sample of a flyover of a DEP aircraft, it is critical that the run time is kept low in order to make the construction process as efficient as possible when adding multiple propellers to the equation. In the preceding sections it was concluded that both models performed satisfactory comparing them to the analysed data found in literature, both for the performance results as for the acoustic results. None of the two models showed significant superiority over the other model, and therefore the run time of both models was the most decisive selection criteria. For this criteria the Helix tool performed significantly better than the NLR tool, which took around 90 minutes to compute a pressure time signal of 30 seconds, whereas the Helix tool took around 15 minutes to compute this. For this reason the decision is made to continue working with the Helix tool in order to build the DEP model. However, it should be noted that the DEP model will be built in such a way that in the end both models can be used to research the noise of a DEP aircraft flyover, but during the construction the Helix tool will be used, and the NLR tool will function mostly as a validation instrument.

6.2. DEP model

Now that the isolated propeller analysis has been completed, it is time to dive into the theory of the aeroacoustics of distributed propellers. A number of studies has already been conducted concerning this topic [43–45], of which all broadly follow the flow diagram presented in [Figure 6.1](#). This section will discuss the methodology used in the existing literature and consequently will assist in producing a methodology for a DEP noise model that fulfills the objective of this project. The section will begin by discussing the existing literature in [Subsection 6.2.1](#), and will be followed by a proposed methodology to create a DEP noise signal in [Subsection 6.2.2](#).

6.2.1. Existing literature

It was already touched upon that distributed propulsion systems offer several advantages over conventional aircraft configurations, such as the ability to allocate the necessary thrust among multiple propellers, which enables the possibility for intelligent propulsion integration. Furthermore, DEP configurations have the potential to minimise noise through a technique known as synchrophasing, which involves coordinating the phase angles of the propeller blades to achieve constructive and destructive interference patterns in the sound fields produced by the multiple propeller configuration. This results in reduced noise emissions at specific locations [46]. From a thorough screening of the literature it can be concluded that the majority of the studies on DEP configurations only evaluate the acoustic interference effects on noise. Nevertheless, in complex integrated architectures, such as a DEP configuration, the aerodynamic interaction between components can alter the acoustic field by modifying the strength of the noise source [47–49]. Therefore, literature on both of these topics will be discussed in this section.

Bernardini et al. [47] performed a numerical study on aeroacoustic interaction within configurations featuring two and three propellers. They concluded that the aerodynamic interference expanded the region of elevated noise levels and amplified the noise peak when compared to simulations that exclusively considered acoustic interference. In a different study, de Vries et al [48] demonstrated through experiments using three propellers that the resultant acoustic waveform could be predicted by superimposing the signal of the individual propellers when the propeller tips were a distance of at least 1R apart. However, when the propellers were placed closer together (with a tip clearance of 0.04R) the noise signal contained sharp peaks which were not captured when the individual signals were simply superimposed. On a contrasting note, Poggi et al. [49] conducted a numerical analysis and showcased that reducing the tip clearance between propellers yielded favourable effects on the radiated noise.

The different results from these studies make it difficult to conclude the impact aerodynamic interference has on a DEP system, but one take-away that seems logical is that when the different propellers are located far apart, the signal of the DEP system can be predicted by superimposing the signals of the individual propellers. This assumption was used, for example in the research performed by Pascioni and Rizzi [43], who dedicated a numerical study on the tonal noise emitted by distributed propellers on an unmanned aerial vehicle (UAV). Their paper starts by introducing the chosen vehicle configuration and the selected operating conditions of said aircraft. Subsequently, the noise of an isolated propeller is computed such that the complex acoustic pressure spectrum is stored on a so called "source hemisphere". A visual representation of this is presented in [Figure 6.10\(a\)](#). It can be seen that from each propeller a straight ray is drawn to the observer on the ground. These paths of propagation are mapped out to identify the intersections of the rays with the source hemisphere, and consequently the query point where the acoustic pressure is interpolated is found. It is worth noting that the magnitude and phase of the acoustic pressure are both linearly interpolated along the surface of the source hemisphere. To model a DEP configuration a source hemisphere is placed at each propeller location, and subsequently the entire procedure is repeated for each propeller. The pressure observed at the observer can be computed with [Equation 6.22](#).

$$p_m(t) = \sum_{n=1}^{N_p} \sum_{n_h=1}^{N_H} \frac{R_s}{r_{m,n}} \tilde{A}_{m,n_h,n} \sin(\Psi) \quad (6.22)$$

in which

$$\Psi = 2\pi n_h f_{0,n} t + \tilde{\psi}_{m,n_h,n} + k_{n_h}(r_{m,n} - R_s) + N_b n_h \psi_{r_n} \quad (6.23)$$

In these equations R_s represents the radius of the source hemisphere, $r_{m,n}$ stands for the distance between the source hemisphere and the observer, and $\tilde{A}_{m,n_h,n}$ represents the pressure amplitude at the intersection of the propagation line and the source hemisphere. By dividing R_s by $r_{m,n}$ spherical spreading is taken into account by scaling the amplitude based on the additional distance to the observer. The final term, Ψ in [Equation 6.22](#) consists of four terms as presented in [Equation 6.23](#). By looking at the entire equation it becomes clear that it shows great resemblance to a sine wave, for which the equation equals: $y = A \sin(2\pi f t + \phi)$. In this equation

there are two terms present in the sine function. The first one represents the angular frequency of the wave, which agrees with the first term of Equation 6.23, where n_h represents a specific harmonic and $f_{0,n}$ is equal to the blade passage frequency. The second term in the perfect sine equation ϕ represents the phase angle of the wave, which represents the offset of the wave from a specified reference position. This term corresponds with the remaining terms in Equation 6.23. In general the acoustic phase with frequency f at the observer m due to propeller n can be denoted with $\tilde{\psi}_{m,n} + k(r_{m,n} - R_s)$, in which $\tilde{\psi}$ is the phase at the source hemisphere and k the wave number, which can be computed as follows $k = 2\pi f/c_0$, with c_0 being the speed of sound. However, in Equation 6.23 there is an additional term, namely ψ_{r_n} , which adjusts the relative angular blade position (also known as clocking), and consequently has an influence on the phase of the sound wave. This procedure is performed for every propeller at every harmonic and subsequently the contributions of each propeller can be linearly summed at the observer.

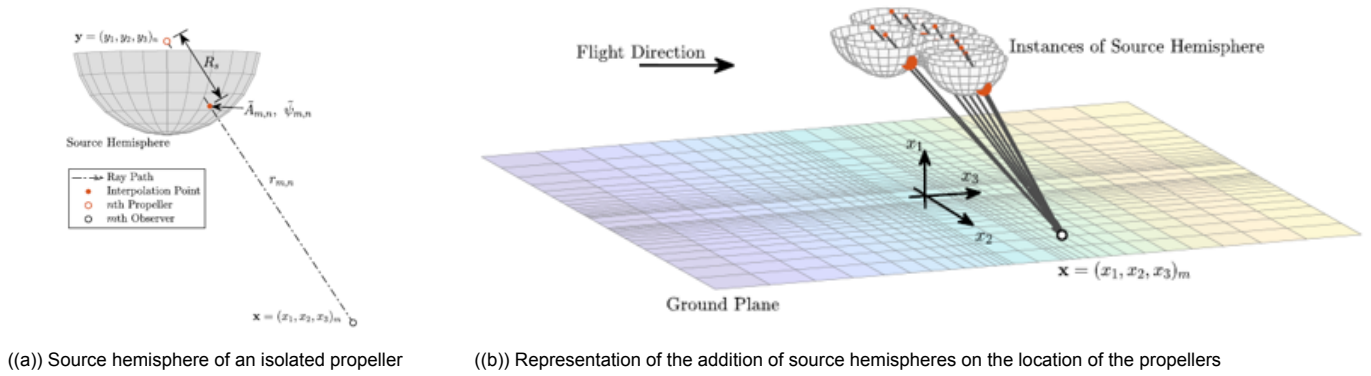


Figure 6.10: Representation of the methodology used by Pascioni and Rizzi [43]

Guerin and Tormen [45] carried out a similar analysis on the existence of acoustic interference in distributed propulsion, and came to a similar conclusion that the acoustic phase has a big influence on the directivity patterns emitted by a DEP aircraft. However, they also performed a comparison by considering the distributed propellers as if they were fully uncorrelated noise sources. The results they obtained are very intriguing, and will be discussed momentarily. First, the methodology of modelling the noise levels for the uncorrelated propeller system will be discussed. In this case the total acoustic pressure $p_{\omega}^2|_{\Sigma_{uncorr}}$ is obtained by multiplying the root mean square of the acoustic pressure emitted by an isolated propeller with the total number of propellers in the system, as presented in Equation 6.24. Subsequently, the OSPL can be computed using Equation 4.5, or alternatively the noise level of an isolated propeller can be computed first and then by making use of the theory on how to add decibel values as explained in Subsection 4.1.2 the OSPL of the distributed configuration can be computed.

$$p_{\omega}^2|_{\Sigma_{uncorr}} = N_p \times p_{\omega}^2 \quad (6.24)$$

As expected, when comparing the results of the correlated and uncorrelated configurations Guerin and Tormen [45] found the levels of the correlated cases to be either significantly lower due to destructive interference or amplified up due to constructive interference. They also concluded that the angular relative blade position of the propellers did have a major influence on the directivity patterns, and should definitely not be discarded. For that reason they conducted a probability study, where they randomly varied these relative positions according to the uniform probability distribution model, and what they found was quite astonishing. That is that the mean directivity result of the probability study was found to be the same as that obtained by analysing the uncorrelated configuration. This means that the work by Guerin and Tormen proves that the average tonal noise emission by a DEP aircraft can be directly computed by taking the distributed propellers as uncorrelated noise sources, which means this type of noise can be computed without too much effort. Although this may be true, since this thesis is focused on the auralization of a DEP aircraft it is deemed necessary to take the acoustic interference effects into account when developing the tonal noise of a DEP aircraft, and therefore a methodology more comparable to Pascioni and Rizzi [43] is deemed necessary to achieve the objective of this project.

6.2.2. Proposed methodology

It was established that since the objective of this project is to create a realistic noise sample of a DEP configuration the acoustic interference patterns should not be neglected. For that reason the research conducted by Pascioni and Rizzi [43] is taken as the main source of inspiration for the proposed methodology to incorporate

the phase difference between the sound waves of the individual propellers. It was decided make use of the retarded-time solution of the Ffowcs Williams and Hawkings (FWH) analogy as described in Casalino [50]. This analogy evaluates the signal received at a given time t through summation of all the disturbances reaching the observer at the same time t . These disturbances are emitted at different retarded times and cover different distances before reaching the observer. For example, when considering an aircraft flyover the sound of the plane might seem like it is coming from a different direction than where the plane appears to be in the sky. This occurs because the sound takes a while to reach the ground. A technique to address this phenomenon involves the utilisation of a Variable Delay Line (VDL). This device introduces a controlled delay to a signal, just like pressing pause for a moment, effectively accounting for the time taken for the acoustic wave to travel from the source to the receiver. For situations involving moving sources or observers, the VDL also incorporates the Doppler shift, solving two problems at once. The operation of the VDL can be described as follows:

$$y[n] = x[n - m[n]], \quad (6.25)$$

where $m[n]$ represents the time varying delay, which can be computed by dividing the time it takes for the sound wave to reach the observer by one over the sampling frequency. This will result in the amount of samples the signal needs to be delayed for. For example, consider an audio signal that is sampled at 50.0 kHz, which means that an audio sample is stored at every $1/50 = 0.02$ ms. Additionally, suppose the propagation distance between the source and receiver is 1 meter, which results in a travel time of 2.94 ms, at a speed of sound of 340 m/s. This results in a delay of $2.94/0.02 = 147$ samples, which means the audio signal needs to be held by 147 samples in a buffer before integrating it to the audio signal that reaches the observer. In this example the delay is composed of an integer amount of samples, however, it is also possible to have a fractional number of samples. The fractional part also needs to be considered, because ignoring it will result in audible aliasing effects as pieces of the signal are being neglected. Including the fractional part is essentially an interpolation task. Throughout this thesis spline interpolation will be used to incorporate the fractional delays as this minimises the chances of aliasing occurring due to waveform gradients being taken into account [24]. This process will be repeated for every propeller over the entire time span of the flyover, and subsequently all the noise signals, referred to as disturbances in Casalino [50], can be summed up at the time t at which the signals reach the observer.

To summarise, a noise sample of a DEP aircraft flyover will be created following these steps.

1. First of all, a reference aircraft must be selected. This aircraft will determine a number of inputs for the model, such as the locations of the propellers, the propeller geometry and the aircraft's operating conditions.
2. Secondly, the propeller performance and the source noise will be computed using the isolated propeller models from TUD and NLR. It was chosen to adopt both models in the research, since the NLR tool will mainly be used for validation, as it is more computationally intensive than the TUD tool. The TUD model runs several orders of magnitude faster and will therefore be the main tool that will be used to identify and analyse the acoustic effects of the distributed propeller configuration.
3. Finally, the source noise needs to be processed to incorporate the propagation effects, and the single propeller noise sample should be expanded to include multiple propellers. This is done by implementing a gain (spherical spreading), followed by implementing the retarded-time solution of the Ffowcs Williams and Hawkings analogy, which evaluates the signal received at a given time t through the summation of all the disturbances reaching the observer at the same time t . These disturbances, which in the case of a DEP aircraft are the sound waves emitted by the different propellers, are emitted at different retarded times and cover different distances before reaching the observer. This analogy is explained in more detail in the beginning of this section, and includes both the interference effects and the Doppler effect. Finally, a filter is included to model the atmospheric absorption. This procedure is explained in more detail in [Section 5.2](#).

Following these steps, a tonal noise sample of a DEP aircraft will be created. In order to produce a more realistic noise sample, a number of new work packages will be introduced in the next chapter, which will be the focus areas during the remainder of this project.

6.2.3. Preliminary results

The methodology and theory described in this literature report have been implemented in a Matlab code in order to generate a noise sample of a flyover event of a DEP aircraft. For these preliminary results the same operating conditions and propeller characteristics were selected as the ones that were used in the flyover experiments

conducted by Elbers [42], and can be found in [Table 6.2](#). In addition to these inputs, it was decided to use a reference aircraft with four propellers, with the propellers being located at 3 meters and 6 meters from the centre on both sides. It should be noted that these locations were chosen arbitrarily and can be easily altered when a validation aircraft is selected.

Table 6.2: Operating and propeller characteristics used as input for the preliminary results

M_x	0.12 [-]
RPM	2520 [rev/min]
$\beta_{0.75}$	18 [deg]
N_B	3 [-]
R	0.82 [m]
N_p	4 [-]

The variables presented above are used as inputs in the performance prediction tools, which in this case result in the values presented in [Table 6.3](#). With the performance coefficients known, it is time to compute the source noise, for which the assumption was made that the source noises of the different propellers are the same. This procedure is done by following the HST to compute the pressure at a specific distance at a range of angles underneath the aircraft ranging from 10 to 170 degrees. The distances at which the source noise is computed is calculated by dividing a constant vertical distance of 1 meter underneath the propeller by the sine of the different observation angles. This for example results in a distance of 1 meter when the aircraft is directly overhead of the observer. Consequently, pressure data points are available for the angles ranging from 10 to 170 degrees around the propeller with increments of 1 degree. It should be noted that during a flyover the angle between the aircraft and the observer changes constantly, and consequently the noise spectrum also varies. To account for this, the actual emission angle during the flyover will be matched with the pressure data computed for that specific angle. However, it is of course possible that the aircraft will be at an angle during the flyover for which no data points have been calculated. When this happens the data of two known adjacent data points will be linearly interpolated to obtain a pressure value.

Table 6.3: Performance coefficients for the preliminary results

C_T	0.090 [-]
C_p	0.076 [-]

Defining the flyover of the DEP aircraft is the next step in the auralization process. It was decided during the start of this project that the aircraft will be at a constant altitude with uniform inflow. For this example an altitude of 100 m was chosen, which is the z-coordinate in the chosen reference frame. The starting and end point of the x-coordinate on the other hand can be computed making use of [Equation 6.26](#). The x-coordinate changes over time by a distance that can be computed with [Equation 6.27](#)

$$x_{start}, x_{end} = \frac{\mp V_x t_{end}}{2} \quad (6.26)$$

$$\Delta x = \frac{(x_{end} - x_{start})t}{t_{end}} \quad (6.27)$$

After the source noise data is computed and the flyover is determined, it is time to execute the digital processing steps to propagate the sound waves to the observer. The four propellers all generate a direct wave and a reflected wave, which results in eight sound waves being used in the analysis. These are all processed following the steps explained in [Section 5.3](#). In short, spherical spreading is incorporated by including a gain. Subsequently, a Variable Delay Line is included to account for the acoustic interference between the propellers and to include the Doppler shift in the analysis. Finally, a filter is included to incorporate the atmospheric absorption. It should be noted that these digital processing steps are propeller and time specific. Following these steps results in a pressure time signal, which is an audible representation of a DEP configuration flyover, and can be found in [Figure 6.11](#).

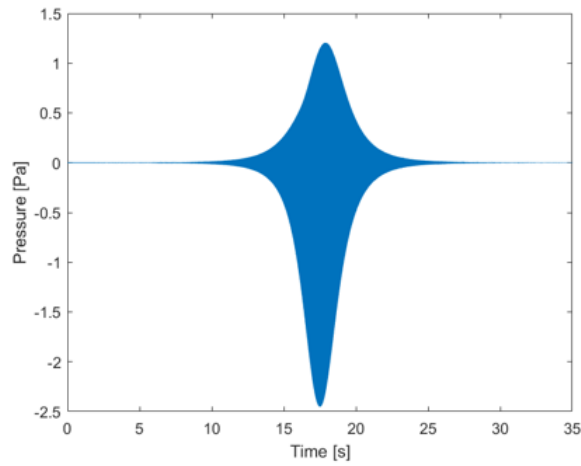


Figure 6.11: Processed pressure time signal as received by the observer

Besides the pressure time signal, the frequency composition of the signal, depicting the aircraft’s flyover, changes over time and is illustrated by a spectrogram presented in Figure 6.12. The spectrogram shows that when the signals of the four propellers with their own distinct propagation paths, each characterised by their unique delay, are combined, an interference pattern appears during the flyover. These interference patterns arise due to the interaction between the signals when they reach the observer. Additionally, it can be seen that for now only tonal components of the signal are considered in the current version of the DEP noise model, as only noise is produced at the BPF, which in this case is 126 Hz, and its harmonics.

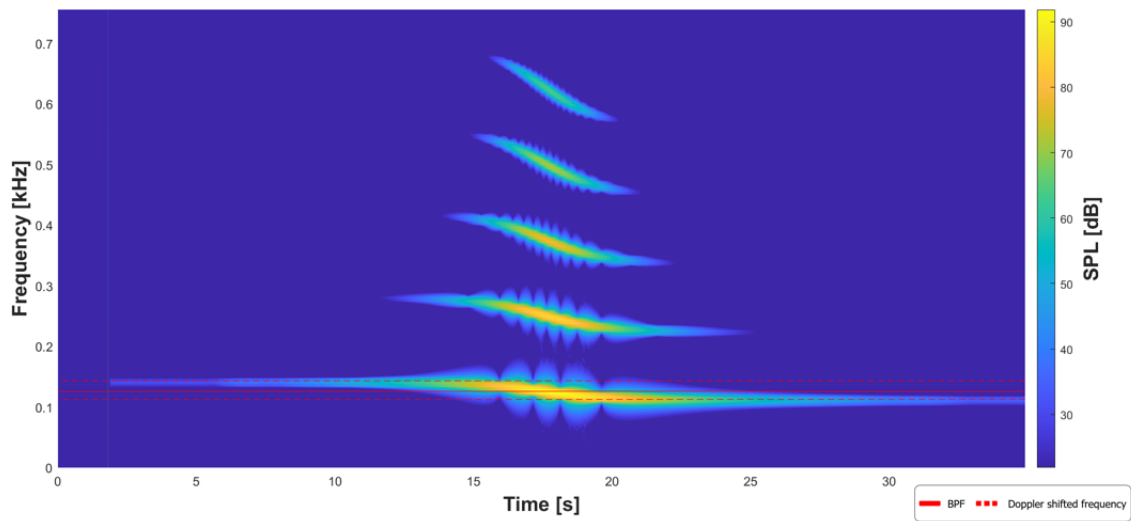


Figure 6.12: Spectrogram of the DEP configuration with a total duration of 35 seconds. The altitude = 100 meters, sampling frequency = 50,000 Hz and the height of the receiver = 1.8 meters.

Research plan and timeline

In [Chapter 2](#), the research questions that guide the project have been formulated. At the moment, a tool that models the tonal characteristics of a DEP configuration exists. However, in order to accomplish the project objectives, a planning is made to expand this model to produce an even more realistic noise sample. This planning will be used during the remainder of this project as a road map to tackle the problem at hand and to keep track of what still needs to be done. The project tasks are divided into five main work packages, for which a road map can be found in [Figure 7.1](#).

Work package 1 has been completed, and will be followed by work package 2, which will focus on validating the model. This is a very critical part of the research, and there are two options that can be used. The first one is validation through the means of a fixed-wing UAV flyover. Secondly, wind tunnel data of three closely spaced propellers can be used. The time frame of this work package depends on the availability of the drones. The flyover tests are expected to be conducted at the end of September. Subsequently, the gathered data needs to be filtered, analysed and compared to the output of the model. If both validation methods are performed this work package is expected to take three-four weeks to complete, which makes it the middle of October. Work package 3 will focus on including the broadband noise to the signal, and is expected to be finished at the end of October (if a suitable method can be found). For work package 4 a sensitivity analysis of the model will be conducted, which is expected to take around two weeks to complete, which will be somewhere in the beginning of November. Work package 5 is the final work package and includes all the general deliverables, such as preparing for presentations and documenting the findings of the research.

All being well, after completing these work packages there will exist a tool that can be used to model a noise sample of a DEP configuration flyover. This sample can be used in order to assess the annoyance of a DEP aircraft compared to an ordinary aircraft. Additionally, this research can act as the foundation for future research on the acoustics of DEP configurations.

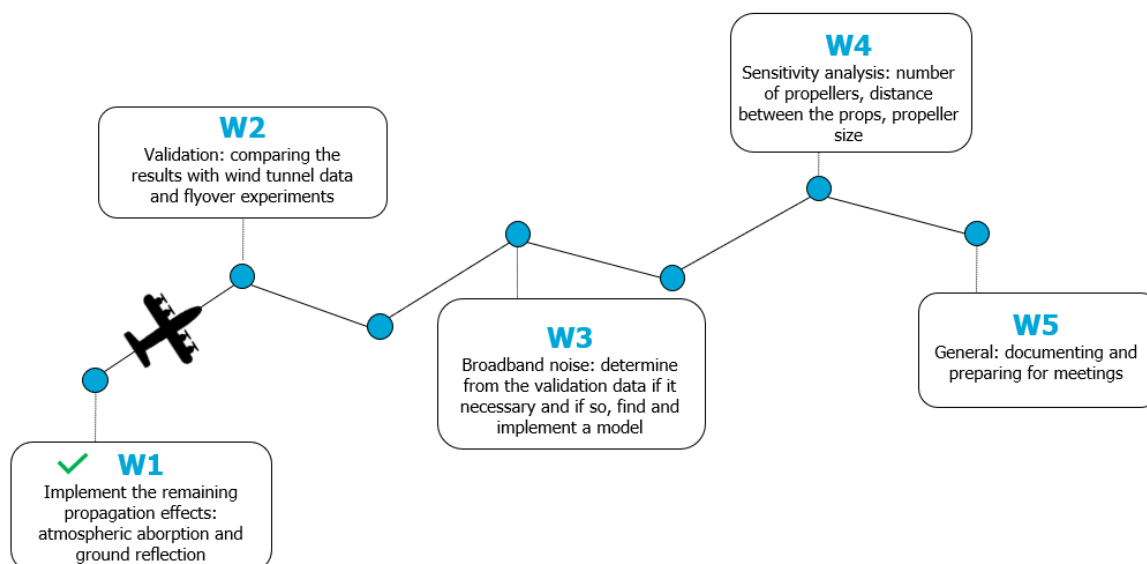


Figure 7.1: Work package breakdown for the remainder of the MSc. thesis



Conclusion

In response to the deeply troubling global warming caused by significant human-made emissions, primarily driven by CO₂ release from burning fossil fuels, the aviation sector has initiated a series of projects to explore alternate propulsion systems. These projects aim to diminish aviation's environmental footprint. Within this context, distributed electric propulsion (DEP) has gathered growing attention over the past ten years. The core idea of DEP involves dividing the overall thrust among multiple propulsors, which are then strategically positioned across the wingspan [43]. This approach presents novel opportunities for designing aircraft with a focus on reducing emissions. While DEP configurations have the potential to revolutionise aircraft designs and performance, there are still several technological and operational challenges that must be addressed before the production of these vehicles can start, e.g. the annoyance experienced by people when a DEP aircraft flies over their head. For that reason, the aim of this thesis is to develop a noise model of such an aircraft, which makes it possible to assess the annoyance experienced by the community before these aircraft configurations start roaming the skies.

Noise produced by propellers can be divided into tonal noise and broadband noise. The first step of the project is to create a tonal noise sample of a DEP aircraft flyover. This will be done by selecting a reference aircraft, which will determine the propeller locations, the propeller geometry and the aircraft's operating conditions. These parameters will function as the input of the existing isolated propeller models from TUD and NLR. Both models use the Helicoidal Surface Theory by Hanson [32] to model the thickness noise and steady loading noise. They only differ in the performance analysis, where the TUD model uses XRotor and the NLR model uses a BEMT-model to compute the thrust coefficient and power coefficient. The decision was made to adopt both models in the research, where the NLR tool will mainly function as the validation for the TUD tool, as it is more computationally intensive. Subsequently, the isolated propeller noise sample will be expanded making use of the retarded-time solution of the Ffowcs Williams and Hawkings (FWH) analogy, which evaluates the signal received at a given time t through the summation of the disturbances, i.e. the noise samples of the different propellers, reaching the observer at the same time t . This analogy has been implemented to account for the multiple propellers in the configuration, however, it also models the Doppler effect, solving two problems at once. In addition to the FWH analogy, spherical spreading is included as a gain and the atmospheric absorption as a filter. Furthermore, the reflection of the sound waves from the ground creates additional paths, which results in an extra number of sound waves (equal to the number of propellers) reaching the observer. For these signals the same processing steps are performed, and subsequently they can all be summed when they reach the observer at time t .

In the next phase, the research will shift towards the broadband noise. Then, will be determined whether it is essential to include the broadband noise to the signal, and if so which model will be selected to incorporate it to the noise sample. This will be checked by validating the model by conducting experiments with a fixed-wing UAV or using wind tunnel data. To conclude, a sensitivity analysis will be conducted in order to analyse the impact of the input parameters on the noise sample. If the project is a success, the noise of a DEP concept can be evaluated and compared to a conventional aircraft, and provided the annoyance experienced lays within an acceptable range the production of such an aircraft will be one step closer to reality.

Appendix

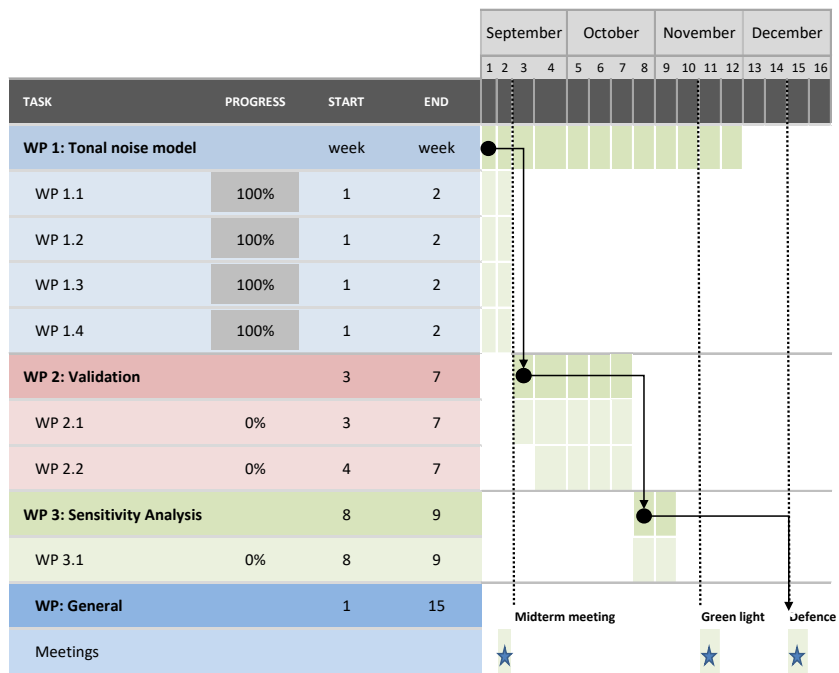


Figure 8.1: Gantt chart

References

- [1] T. Sinnige. Aerodynamic and aeroacoustic interaction effects for tip-mounted propellers, 2018.
- [2] L. Veldhuis. Propeller wing aerodynamic interference, 2005.
- [3] R. Hager and D. Vrabel. Advanced turboprop project, 1988.
- [4] IATA. Air passenger numbers to recover in 2024. <https://www.iata.org/en/pressroom/2022-releases/2022-03-01-01/>, 2022. Online; accessed 9 May 2023.
- [5] L. Gipson. Advanced air vehicle program (aavp). <https://www.nasa.gov/aeroresearch/programs/aavp/description/>, 2020. Online; accessed 9 May 2023.
- [6] T. Perry D. Kim and J. Ansell. A review of distributed electric propulsion concepts for air vehicle technology, 2018.
- [7] NASA. NASA's X-57 concept for distributed electric propulsion. <https://www.nasa.gov/specials/x57/>, 2017. Online; accessed 7 March 2023.
- [8] Maeve Aerospace bv. Maeve Aerospace's concept for distributed electric propulsion. <https://maeve.aero/home>. Online; accessed 7 March 2023.
- [9] T. Sinnige. *Lecture slide AE4130 on Aircraft Aerodynamics*. Delft University of Technology, 2020.
- [10] Jeff Borland, Peter Dawkins, David Johnson, and Ross Williams. Returns to investment in higher education, 2000.
- [11] T. Sinnige D. Ragni Y. Wang G. Eitelberg L. Veldhuis Q. Li, K.Ozturk. Design and experimental validation of swirl recovery vanes for propeller propulsion systems, 2018.
- [12] World Health Organization. Environmental noise guidelines for the european region, 2018.
- [13] A. Hansell J. Hileman S. Janssen K. Shephard M. Basner, C. Clark and V. Sparrow. Aviation noise impacts: State of science, 2017.
- [14] M. Heilig. Aircraft noise: Modelling measuring, 2020.
- [15] D.G. Simons and M. Snellen. Reader aircraft noise and emissions (part a), 2020.
- [16] The European Parliament and the Council of the European Union. Directive 2002/49/ec of the european parliament and of the council of 25 june 2002 relating to the assessment and management of environmental noise., 2002.
- [17] R.H. Self. *Propeller Noise*. Encyclopedia of Aerospace Engineering, 2010.
- [18] J.E. Marte and D.W. Kurtz. A review of aerodynamic noise from propellers, rotors and lift fans, 1970.
- [19] M. Haddaoui. Development of a propeller source noise model, 2019.
- [20] M. Snellen D.G. Simons. *Aircraft Noise and Emissions: Introduction to general acoustics and aircraft noise*. TU Delft, 2022.
- [21] H. Blackburn. *Quadrupoles in potential flow: two model problems*. Journal of Fluid Mechanics, 1982.
- [22] M. Vorländer. *Auralization: Fundamentals of acoustics, modelling, simulation, algorithms and acoustic virtual reality*. Springer, 2008.
- [23] E.M. Salomons. *Computational atmospheric acoustics*. Elsevier, 1999.
- [24] M. Arntzen. Aircraft noise calculation and synthesis in a non-standard atmosphere, 2014.
- [25] S. Burger. Multi-fidelity aerodynamic and aeroacoustic sensitivity study of isolated propellers, 2020.
- [26] O. Gur and A. Rosen. Comparison between blade-element models of propellers, 2008.

- [27] P. Alexandros Koutsoukos. Aerodynamic and aeroacoustic interaction effects of a distributed-propeller configuration in forward flight, 2022.
- [28] C. Lock and H. Bateman. Experiments with a family of airscrew. part iii: Analysis of the family of airscrew by means of vortex theory and measurements of total head, 1923.
- [29] W.F. Durand. Aerodynamic theory, third edition, vol 4, 1935.
- [30] R.D. Clark and C.A. Leiper. The free wake analysis. a method for the prediction of the helicopter rotor hovering performance, 1970.
- [31] T. Theodorsen. Theory of propellers, 1948.
- [32] D. Hanson. Helicoidal surface theory for harmonic noise of propellers in the far field, 1980.
- [33] L. Gutin. On the sound field of a rotating propeller, 1948.
- [34] E. Envia. Asymptotic theory of supersonic propeller noise, 1992.
- [35] H. Brouwer. A lifting line model for propeller noise, 1989.
- [36] M.E. Goldstein. Aeroacoustics, 1976.
- [37] M. Drela and H. Youngren. Xfoil 6.94 user guide, 2001.
- [38] P. Liu T. Sinnige X. Geng, T. Hu and G. Eitelberg. Analysis of thrust-scaled acoustic emissions of aircraft propellers and their dependence on propulsive efficiency, 2021.
- [39] M. Drela and H. Youngren. Xrotor user guide. http://web.mit.edu/drela/Public/web/xrotor/xrotor_doc.txt, 2003. Online; accessed 30 May 2023.
- [40] G.L. Stefko and R.J. Jeracki. Wind tunnel results of advanced high speed propellers at takeoff, climb, and landing mach numbers, 1985.
- [41] P. Block. Experimental study of the effects of installation on single and counter-rotation propeller noise, 1986.
- [42] N. Elbers. Assessment of an aircraft propeller noise model by verification & experimental validation, 2021.
- [43] S.A. Rizzi K.A. Pascioni and N.H. Schiller. Noise reduction potential of phase control for distributed propulsion vehicles, 2019.
- [44] J. Rathsam A. Christian S. Rizzi, D. Palumbo and M. Rafaelof. Annoyance to noise produced by a distributed electric propulsion high-lift system, 2017.
- [45] G. Sebastien and T. Damiano. On the importance of acoustic interferences in distributed propulsion, 2023.
- [46] F. Avallone F. do Nascimento Monteiro, D. Ragni and T. Sinnige. Low-order acoustic prediction tool for estimating noise emissions from distributed propeller configurations, 2023.
- [47] U. Lemma C. Pasquali C. Poggi M. Rossetti G. Bernardini, F. Centracchio and J. Serafini. Aeroacoustic numerical characterization of propellers interaction, 2019.
- [48] T. Sinnige R. Vos R. de Vries, N. van Arnhem and L.L.M. Veldhuis. Aerodynamic interaction between the propellers of a distributed-propulsion system in forward flight, 2021.
- [49] G. Bernardini C. Poggi and M. Gennaretti. Aeroacoustic analysis of wing-mounted propeller arrays, 2021.
- [50] Damiano Casalino. Analytical and numerical methods in vortex-body aeroacoustics, 2002.

III

Supporting work

Read me file for Helix tool and DEP model

The Helix tool consists of multiple files containing various functions. These functions are imported into the **main** file, which serves as the operating point from where the tool is run. Prior to running the Helix tool, it is necessary to verify if the correct propeller geometry is being loaded into the model. Furthermore, it is essential that the airfoil files are formatted exactly in the same way as presented in the SR-2 propeller files.

The input files specifying the propeller geometry are the following:

- **betadata_Sr2**, which represents the radial difference in β distribution.
- **chord_Sr2** is the chord over diameter along the propeller radius.
- **rR024 - rR100** represent the airfoil coordinates along the propeller radius.
- **thicknessdata_Sr2** stands for the thickness over chord distribution.

It is necessary to import these input files in the following Matlab functions:

- **rightformat()**: the airfoil coordinates rR024 - rR100 need to be inserted here in order to format the files correctly.
- **run_xfoil()**: betadata_Sr2 and chord_Sr2 need to be imported here in order to run XFOIL.
- **thickness_chord()**: thicknessdata_Sr2 determines the maximum t/c ratio for different radial sections.
- **wavenumber()**: chord_Sr2 is needed to determine the non-dimensional wave numbers

Furthermore, the variables n_i and r_R need to be changed such that they represent the correct range of selected airfoil coordinates sections. These variables can be changed in the main() and run_xfoil() files. Subsequently, one should also alter the variable q in the run_xfoil() file. This variable selects the corresponding Re and M per radial location.

In Figure 1.1, the flow of the Helix tool is presented. The yellow blocks represent the import files discussed above, while the grey blocks denote functions/files in Matlab. Now, the main file can be executed. First of all, XFOIL will compute the 2D aerodynamic properties, which are the $C_l - \alpha$, $C_d - \alpha$ and $C_m - \alpha$ distributions. If an error arises, indicating XFOIL's failure to converge, consider modifying the angle of attack step or range. Adapting these parameters can enhance convergence and resolve issues with the XFOIL computations. XFOIL is by far the most time intensive segment of the Helix tool.

Subsequently, the radial loading and the performance coefficients are calculated making use of XRotor. During this step potential errors may arise in the read_xrotordata() file, specifically when parsing the SR2_data and encountering stalled sections. To proceed, locate and remove the "s" situated between de C_l and C_d columns in the SR2_data file. Save the modified SR2_data and initiate the main file

for the code after XRotor. Another potential error in reading the SR2_data file may occur if data has shifted a row down due to convergence issues. In such cases, modify '16' to '17' on line 7, and '13' to '14' on lines 49 and 50 in read_xrotordata().

The output of the Helix tool is a pressure-time signal, which is computed by following the Helicoidal Surface Theory. When the Helix tool is completed, and the signal has been subjected to the digital processing steps that incorporate the propagation effects, the code concludes with reporting some interesting outputs, such as the maximum OSPL, OSPL over time plot and directivity plot.

Now the source noise of an isolated propeller has been computed, it is time to expand the isolated propeller model to a model that incorporates the noise of multiple propellers. First of all, the number of propellers and the propeller locations should be modified in the file 'define_flyover()'. Thereafter, the function 'DEP_noise' should be run. This function models the noise observed by a specified receiver on the ground. The output of the DEP model is a pressure-time signal, for which the directivity plot, the maximum OSPL and the OSPL over time plot are given as outputs of the model.

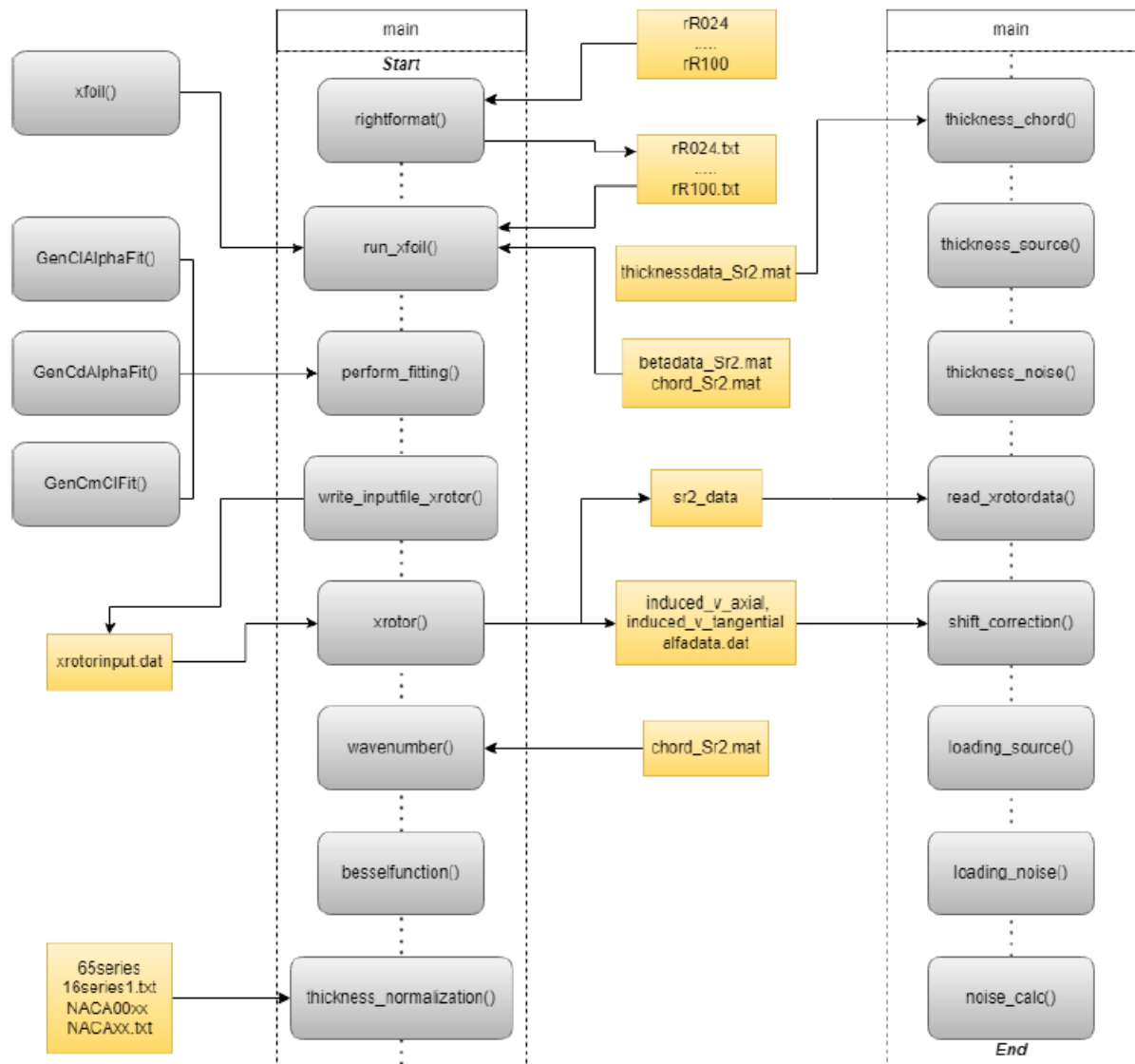


Figure 1.1: Helix tool work flow diagram [1]

Bibliography

- [1] N. Elbers. Assessment of an aircraft propeller noise model by verification & experimental validation, 2021.